SIMULATION OF FLOW PULSATIONS IN GAP GEOMETRIES

SIMULATION OF FLOW PULSATIONS IN GAP GEOMETRIES USING UNSTEADY REYNOLDS AVERAGED NAVIER-STOKES MODELLING

By

GEORGE ARVANITIS, DIPLOMA (MECH. ENG.)

A Thesis

Submitted to the School of Graduate Studies

in Partial Fulfillment of the Requirements

for the Degree

Master of Applied Science

McMaster University

MASTER OF APPLIED SCIENCE (2008) McMaster University

(Mechanical Engineering) Hamilton, Ontario

TITLE: Simulation of Flow Pulsations in Gap Geometries Using Unsteady Reynolds Averaged Navier-Stokes Modelling

AUTHOR: George Arvanitis, Diploma in Mechanical Engineering (National Technical University of Athens)

SUPERVISORS: Dr. Marilyn F. Lightstone

Dr. Mohamed S. Hamed

NUMBER OF PAGES: xviii, 132

ABSTRACT

An unsteady Reynolds Averaged Navier-Stokes (URANS) based turbulence model, the Spalart-Allmaras (SA) model, was used to investigate the flow pulsation phenomenon in compound rectangular channels for isothermal flows. The computational fluid dynamics (CFD) commercial package ANSYS CFX-11.0 was used for the simulations. The studied geometry was composed of two rectangular subchannels connected by a gap, on which experiments were conducted by Meyer and Rehme [34] and were used for the validation of the numerical results. Two case studies were selected to study the effect of the advection scheme. The results using the first order upwind advection scheme had clear symmetry and periodicity. The frequency of the flow pulsations was underpredicted by almost a factor of two. Due to the inevitable numerical diffusion of the first order upwind scheme, it was more appropriate to use a second order accurate in space advection scheme for comparison with the experiments. The span-wise velocity contours and the velocity vector plots at planes parallel to the bulk flow, together with the time traces of the velocity components at selected monitor points showed the expected cross-flow mixing between the subchannels through the gap. Although the SA model does not solve directly for the turbulence kinetic energy, a kinetic energy associated with the unsteady solutions of the momentum equations was evaluated and qualitatively compared with the experimental turbulence kinetic energy. The calculated kinetic energy followed the trends of the experimental turbulence kinetic energy at the gap area, predicting two peaks at the edges of the gap. The

dynamics of the gap pulsations were quantitatively described through temporal auto-correlation and auto-power spectral density functions and the numerical predictions were in agreement with the experiments. Studies on the effect of the Reynolds number and the computational length of the domain were also carried out. The numerical results reproduced the relationship between the Reynolds number and the frequency of the auto-power spectral density functions. The impact of the channel length was tested by simulating a longer channel. It was found that the channel length did not significantly affect the predictions. Simulations were also performed using the $k - \varepsilon$ model. While flow pulsations were predicted with this model, the frequency of the pulsation was in poor agreement with the experimentally measured value.

Acknowledgements

I would like to thank Dr. Marilyn F. Lightstone and Dr. Mohamed S. Hamed for their supervision and mentoring. The financial support of the Natural Sciences and Engineering Research Council of Canada (NSERC) and the University Network of Excellence in Nuclear Engineering (UNENE) is also gratefully acknowledged.

Dedication

To Panayiotis Giannakis, The Dragon.

Contents

List of Tables

List of Figures

List of Symbols

C_f: coefficient of friction

C_p: specific heat capacity $\left[\frac{J}{kgK}\right]$

D: rod diameter $[m]$

D_h: hydraulic diameter $[m]$

f: Fanning friction factor

g: acceleration of gravity $= 9.81 \left[\frac{m}{s^2}\right]$

h: enthalpy $\left[\frac{J}{kgK}\right]$

k: turbulence kinetic energy $\left[\frac{J}{kg}\right]$

p: pressure $[Pa]$

p: instantaneous pressure $[Pa]$

$\overline{p}$: time mean pressure $[Pa]$

p': pressure fluctuation $[Pa]$

P: rod pitch $[m]$

q': net heat transport through gap per unit length $\left[\frac{W}{m}\right]$

R: rod radius $[m]$

r: radial distance $[m]$

Re: Reynolds number

S: gap spacing $[m]$

St_g: gap Stanton number

Str: Strouhal number

T: temperature $[K]$

T: instantaneous temperature $[K]$

$\overline{T}$: time mean temperature $[K]$

T': temperature fluctuation $[K]$

U: velocity $\left[\frac{m}{s}\right]$

u: instantaneous velocity $\left[\frac{m}{s}\right]$

$\overline{U}$: time mean velocity $\left[\frac{m}{s}\right]$

u': velocity fluctuation in stream-wise or axial direction $\left[\frac{m}{s}\right]$

u^+: dimensionless velocity

U_b: bulk velocity $\left[\frac{m}{s}\right]$

u_τ: friction or average shear velocity $\left[\frac{m}{s}\right]$

v': velocity fluctuation in wall-normal (transverse) or radial direction $\left[\frac{m}{s}\right]$

W: distance between wall and rod center $[m]$

w': velocity fluctuation in span-wise or azimuthal (circumferential) direction $\left[\frac{m}{s}\right]$

x: axial (stream-wise) direction $[m]$

y: wall-normal (transverse) direction $[m]$

y^+: dimensionless distance from wall $\left[= \frac{yu_\tau}{\nu}\right]$

z: span-wise direction $[m]$

δ_{ij}; distance between centres of subchannels i and j $[m]$

ε: turbulent dissipation rate $\left[\frac{W}{kg}\right]$

ε^+: dimensionless eddy diffusivity

ε_H^r: turbulent diffusivity of heat in radial direction $\left[\frac{m^2}{s}\right]$

ε_H^x: turbulent diffusivity of heat in axial direction $\left[\frac{m^2}{s}\right]$

ε_H^ϕ: turbulent diffusivity of heat in azimuthal direction $\left[\frac{m^2}{s}\right]$

ε_{ij}^H: turbulent diffusivity of heat $\left[\frac{m^2}{s}\right]$

ε_M^r: turbulent diffusivity of momentum in radial direction $\left[\frac{m^2}{s}\right]$

ε_M^x: turbulent diffusivity of momentum in axial direction $\left[\frac{m^2}{s}\right]$

ε_M^ϕ: turbulent diffusivity of momentum in azimuthal direction $\left[\frac{m^2}{s}\right]$

κ: Von Karman constant

λ: Darcy friction factor

μ_t: turbulent dynamic viscosity $[Pa.s]$

ν: kinematic viscosity $\left[\frac{m^2}{s}\right]$

ν_t: turbulent kinematic viscosity $\left[\frac{m^2}{s}\right]$

ρ: density $\left[\frac{kg}{m^3}\right]$

ρ: instantaneous density $\left[\frac{kg}{m^3}\right]$

$\overline{\rho}$: time mean density $\left[\frac{kg}{m^3}\right]$

ρ': density fluctuation $\left[\frac{kg}{m^3}\right]$

ϕ: azimuthal angle $[rad]$

Chapter 1

Introduction

1.1 Relevance of Research to Nuclear Industry Applications

Fluid pulsations in subchannel geometries is of importance to the nuclear industry with implications to nuclear reactor safety analysis and design. In the reactor core, the heat generation within the fuel rods is removed by the coolant which flows axially past the rods. Under loss-of-coolant accident conditions, single-phase vapour or two-phase conditions can occur depending on the magnitude of the break in the heat transport system. An understanding of the behaviour of the fluid flow under normal or abnormal conditions is very important, in order to accurately predict the fuel rod temperatures and ultimately improve the design of the reactor cores.

CANDU reactor cores contain cylindrical rod bundle geometries, where coolant flows axially along the rods. A cross-section of a CANDU 37-element fuel rod bundle can be seen in figure 1.1. In this figure the bounding ring represents the inner pressure

tube in which the nuclear fuel is kept. The numbered circles represent the cylindrical fuel rods, while the remaining numbered geometric shapes are the cross-sections of the fluid flow regions, known as subchannels. These lines that frame the subchannels indicate the gap regions where the flow area is reduced. Specifically, the subchannels are defined as the small flow regions surrounded by rod surfaces and separated by imaginary lines connecting the centroids of the fuel rods. Subchannels are bounded by either the fuel rod wall, pressure tube walls, or the regions between the subchannels, referred to as gaps. The subchannels can be classified as walls, if they are next to walls (subchannels 50, 51, 60, etc, in figure 1.1), and as triangular (subchannels 1, 3, 9, etc, in figure 1.1) or square subchannels (subchannels 12, 18, 30, etc, in figure 1.1), depending on their shape. The important parameters that are mainly used to describe the geometric characteristics in such flow configurations are the rod diameter, D, the centre-to-centre distance between the rods or the pitch, P, the wall distance, W, and the gap width, S. Referring to figure 1.1, P is the distance between the centres of two neighbouring rods (such as rods 4 and 13 or rods 4 and 3), S is the minimum distance between the walls of two neighbouring rods and W is the distance from the centre of a rod next to a wall and the surface of that wall (such as rod 49 and the pressure tube wall).

As the coolant fluid flows axially past the rods, mass, momentum and heat are exchanged due to interchange mixing through the gaps between the rods. The main interest of the current research is on the fluid cross-flow at the gap regions

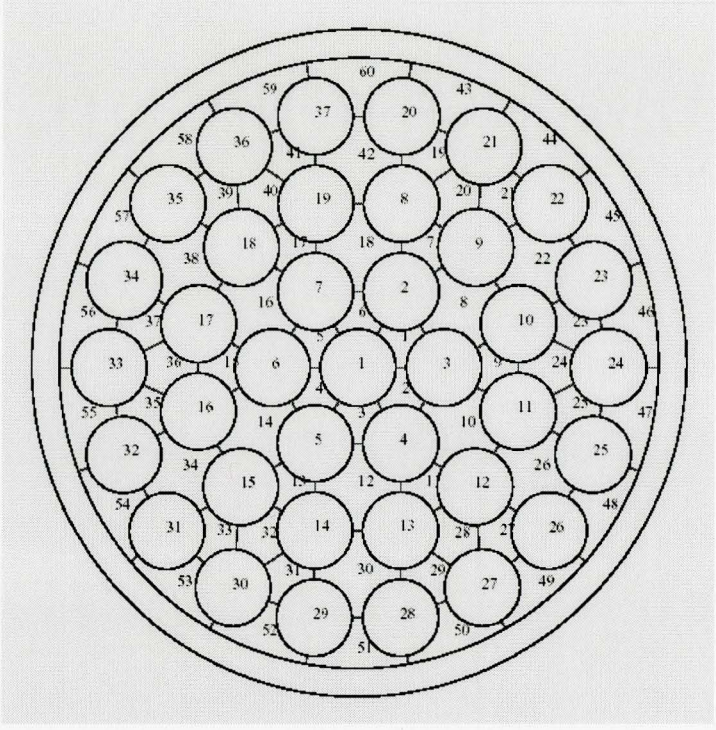

Figure 1.1: Cross-section of a CANDU 37-element fuel bundle. Adapted from Eiff and Lightstone [17]

which connect adjacent subchannels. The flow across the gaps aids in fluid mixing and in homogenizing the fluid temperatures across the rod bundles, thus playing an important role in determining the heat transfer rates from the fuel rods.

An understanding of the physics of this mixing process is necessary for development of constitutive models for use in nuclear safety analysis codes. During the last forty years there has been an extensive experimental and numerical research, trying to understand the mechanism that causes these high mixing rates ([53], [55], [66], [43] [3], [58], [26], [49], [36], [30]). In the early 1970's, the main trend was to attribute this mixing process to secondary flows. Later on, experimental research has indicated

that large-scale flow pulsations are responsible for the majority of the mixing between subchannels [55], [35], [21], [22].

The main features discussed in the relevant investigations, that could replicate the momentum and heat exchange process in rod bundle geometries, are the anisotropy of turbulence, the secondary flows and the large-scale flow pulsations. The periodic flow pulsations are observed at the gap regions. As the gap width, S, is reduced, the stream-wise and circumferential turbulence intensities are increased. The periodic flow pulsation phenomenon is the main contributor to the anisotropic turbulence structure in the flow field. The anisotropy of the turbulence can be observed through the estimation of the eddy diffusivities. The eddy diffusivity parallel to the rod walls is much higher than the eddy diffusivity normal to the rod walls. This anisotropic turbulence structure, drives secondary flows, which are generated in these flows.

1.2 Purpose of Research

The goal of the current research is to determine if an unsteady Reynolds Averaged Navier Stokes (RANS) simulation is able to predict the flow pulsations that have been observed experimentally. If this numerical approach is able to capture the essential physics of the flow, then the longer term goal is to use this model as basis for development of a constitutive model which could be incorporated into broader safety analysis codes. The specific objectives of the thesis report are summarized in

the next section.

In order to assess the safety of nuclear reactors and to mitigate potential consequences of accidents, numerical simulations of the large reactor systems are performed. These simulations are multi-disciplinary and often include simulation of both the primary and secondary side heat transport systems, reactor physics, fuel channels, moderator flows, containment, and atmospheric dispersion. Because of the large-scale of the analyses and the long transients that can occur, integrated models are used. For example, thermalhydraulics behaviour is modelled using one-dimensional two-fluid codes which are able to predict the important phenomenon, but require accurate correlations and empirical models since the fine details of the flows (such as the details of the boundary layers and the turbulence) are not solved for directly.

In the Canadian nuclear industry, the fuel temperatures at the reactor cores are obtained from computer codes such as FACTAR, CATHENA, TUF, ASSERT-PV among others. Rather than solving for the detailed description of the fluid flow and heat transfer in fuel rod bundles, these codes average over a larger region (the size of this region is dependent on the code used and the level of detail desired). Thus, constitutive relations that supply the information that was lost during the averaging or integrating process are required. This can include pressure-drop or friction factor correlations, k-factors due to obstructions such as bearing pads or spacers, heat transfer correlations, etc. Of the codes listed above, the most detailed information is

obtained from ASSERT-PV which uses a grid based on the flow subchannels.

In contrast to the above mentioned numerical approaches, CFD codes solve the conservation equations for mass, momentum and energy on fine grids. Previous attempts to model inter-subchannel thermal mixing using standard turbulence models have had mixed success [50]. Steady state predictions significantly underpredict the mixing since the flow pulsation phenomenon is not captured. While accurate modelling of the two-phase flow in the fuel channel is an important objective for nuclear safety analysis, the current research is focused on single-phase flows as a first step in attaining this goal.

Recent studies using an unsteady Reynolds Averaged Navier-Stokes (RANS) model to simulate isothermal flows in a channel containing a single rod [10] and isothermal flows in a 37-rod bundle [11] have shown that the coherent structures in the regions between the rods and the rods and the walls can be predicted. Furthermore, RANS models are the least computationally intensive models for modelling turbulent flows, compared to the other two main categories of models, namely LES (Large Eddy Simulation) and DNS (Direct Numerical Solution). DNS models solve for all the scales of turbulence. RANS models, in contrast, model all the scales of turbulence. In between them lie the LES models, which solve for the large scales of turbulence and model the small scales. Considering the computational cost, it was decided for this research to apply an unsteady RANS approach for isothermal flows in selected geometries. The specific model that was used is the Spalart - Allmaras (SA) model.

This model was calibrated for predictions of aerodynamic flows where there is a formation of vortex structures. Since the large-scale pulsation phenomenon that we anticipated to capture had the characteristics of flows similar to the ones for which the SA model was calibrated, it was decided to use it in this numerical investigation.

The idea of this numerical research was to start from simple isothermal turbulent flow configurations and study step by step, in terms of complexity, the phenomenon of cross-flow mixing through large-scale pulsations. Experimental [68], [34] and numerical research [21], [22] has shown that a quasi-periodic large scale turbulent structure exists in any longitudinal slot or groove in a wall or a connecting gap between two flow channels, provided that the gap's depth is more than approximately twice its width. More precisely, it has been proved that the same flow pulsation phenomena that appear in flows in cylindrical geometries as the ones in fuel reactor cores, also occur in rectangular compound channels [34]. It was thus decided to validate the SA model for turbulent flows in compound rectangular geometries, using the flow configurations that were used by Meyer and Rehme in their experiments in 1994 [34]. The goal of this broader numerical research is to continue investigating the flow pulsation phenomenon problem by gradually adding to it more physical and geometrical parameters, approaching the ideal end, which is the successful numerical prediction of non-isothermal turbulent flows in subchannel geometries, in order to develop a simplified physical model of subchannel mixing for use in the broader safety analysis codes. The research results presented in this thesis represent the outcome of the first

step in the broader research program.

1.3 Objectives of Thesis

In the frame of the overall purpose of this research described in the above section, the objective of this thesis is to numerically explore the isothermal turbulent flow pulsation phenomenon in compound rectangular channel geometries, by applying an unsteady RANS approach. The specific objectives of the thesis are the following.

1. examine the turbulence structure of isothermal flows in the compound rectangular configurations used by Meyer and Rehme [34]

2. select an appropriate unsteady RANS model and assess its applicability to the capture of the large-scale flow pulsation phenomenon, reported in the experimental outcomes.

3. validate the results of the simulations by comparing them against the available experimental measurements.

1.4 Structure of Thesis

Following this introduction, the structure of the thesis report is divided in four chapters. The second chapter deals with a literature survey on the characteristics of the fluid flow, heat transfer and turbulent mixing in heated rod bundle geometries. The gist of the experimental effort on the studied phenomena is revealed through the

sections of chapter 2 on the formation of the mean axial velocity profiles, the secondary flows, the Reynolds stresses and the periodic flow pulsations and their effect in the resulting anisotropic turbulent field. This chapter ends with an overview on the relevant numerical investigations.

In chapter 3 an overview of the Reynolds Averaged Navier-Stokes models, together with the main characteristics of the SA model are presented.

Chapter 4 deals with the analysis of the results of this research. First, the choice of the experiments to validate the numerical results, together with the description of these experiments is provided. Following this, the simulation details are mentioned. After the report on the grid independence test, the main part of this chapter is a comparison of the numerical results with the experimental measurements and a discussion of these results. The last two subsections of chapter 4 refer to a study on the effect of the computationally implemented length of the channel and a comparison of the SA model results to those obtained using the commonly applied $k - \varepsilon$ turbulence model.

Finally, the thesis ends with chapter 5, where the conclusions of this work are summarized and a potential future direction on the current research is given.

Chapter 2

Literature Review

2.1 Overview

An understanding of the flow characteristics and the underlying physics that govern inter subchannel thermal mixing processes in closely spaced rod bundle geometries is important for nuclear safety analysis and design. Extensive experimental work has been performed for over a period of four decades in related geometries with the aim to understand the nature of the turbulent flow field structure in narrow gap regions. This chapter provides a review of experimental studies on the turbulent flow field structure in such geometries and it also serves as an introduction on the related numerical investigations.

2.2 Turbulent Flow in Rod Bundle Geometries

2.2.1 Turbulent friction factor for fully developed flow

From a pressure gradient and wall shear stress balance, a Fanning friction coefficient, f, is defined as [57]:

$$f = -\left(\frac{dp}{dx}\right)\frac{R}{\rho U_b^2} \tag{2.1}$$

where $\frac{dp}{dx}$ is the axial pressure gradient. Since for a fully developed flow the pressure gradient in a duct is constant, the coefficient is indicative of the pressure drop in a duct.

For circular pipes, Prandtl proposed a friction factor relationship based on Nikuradse's friction factor data [38]. This relationship is known as Prandtl's universal law of friction for smooth pipes:

$$\frac{1}{\sqrt{4f}} = 2.0\log\left(Re\sqrt{4f}\right) - 0.80 \tag{2.2}$$

Due to geometrical differences, the expressions for the friction factors for flow through rod bundles differ from the ones in circular pipes. A number of experimental and numerical studies have been made in order to establish friction factor relationships, applicable to flows in rod bundles.

Rehme [43] proposed a method called the G^*-method for estimating the friction factor for turbulent flows in non circular channels. The relationship he developed is:

$$\sqrt{\frac{2}{f}} = A\left[2.5\ln\left(Re\sqrt{\frac{f}{2}}\right) + 5.5\right] - G^* \tag{2.3}$$

where A and G^* are geometry factors. These factors are exported from diagrams which provide the two factors as a function of a geometric factor for laminar flow, K. The value of K is obtained by solving the Poisson equation. It is generally acceptable that the G^*-method is accurate, but it is difficult to apply because of the complexity of the calculations.

Cheng and Todreas [13] presented a simple friction factor relationship for laminar and turbulent flows:

$$\lambda = \frac{C_f}{Re^m} \tag{2.4}$$

where λ is the Darcy friction factor ($\lambda = 4f$) and m is equal to 1.0 for laminar flows and 0.18 in the case of turbulent flows. From equation 2.4, it is obvious that in the case of flows in rod bundle geometries, similar to circular pipe flows, the friction factor decreases with increasing Reynolds number. In equation 2.4 the constant, C_f, is expressed as a function of the pitch-to-diameter ratio, $\frac{P}{D}$:

$$C_f = \alpha + b_1\left(\frac{P}{D} - 1\right) + b_2\left(\frac{P}{D} - 1\right)^2 \tag{2.5}$$

Cheng and Todreas determined the coefficients α, b_1, b_2 by comparing their method with the Rehme's G^*-method. In this way, the friction factor relationship given in equation 2.4 can predict the friction factor as accurately as the Rehme's G^*-method and has also the advantage of simplicity, which is important in applications.

A plot of the friction factor versus the pitch-to-diameter ratio of rod bundles at a Reynolds number of 10^5, using Cheng and Todreas' friction factor relationship (equation 2.4) is shown in figure 2.1. The different types of subchannels can be seen in figure 1.1 in section 1.1 of the Introduction chapter.

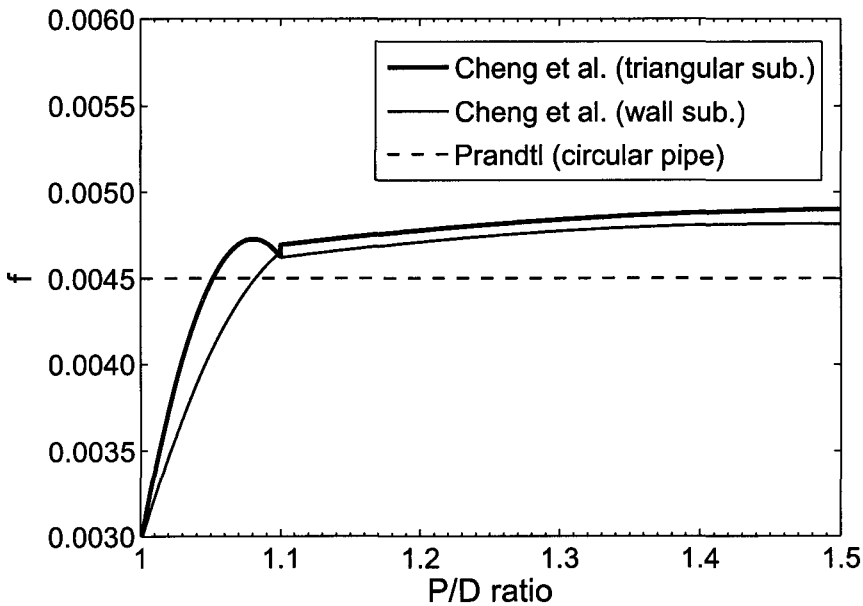

Figure 2.1: Friction factors at $Re = 10^5$ as a function of the $\frac{P}{D}$ ratio. Based on Cheng and Todreas [13]

Also, included in figure 2.1 is the friction factor plot in circular pipes predicted by Prandtl's universal law of friction for smooth pipes (equation 2.2). As the pitch-to-

diameter ratio increases from around 1.0 to around 1.1, the friction factor, predicted by Cheng and Todreas, increases abruptly up to the friction factor for circular pipes and then it continues to increase slowly for $\frac{P}{D}$ values higher than around 1.1. This behaviour was also observed by Rehme [42]. With comparison to circular pipe cases, friction factors in rod bundle geometries are higher for $\frac{P}{D}$ values higher than 1.1. The observed discontinuity in the plots of Cheng and Todreas' correlations is due to the different constants in the expression of C_f (equation 2.5) used for: $1.0 \leq \frac{P}{D} \leq 1.1$ and for: $1.1 < \frac{P}{D} \leq 1.5$.

2.2.2 Mean axial velocity

Rehme [43] used pitot tubes to measure the axial velocity distribution in a wall subchannel of a rod bundle geometry at a Reynolds number of $8.73 * 10^4$. The distribution of the positions at which measurements were taken, is shown in figure 2.2. In this figure, the horizontal (parallel to the channel walls) x-direction and the azimuthal or circumferential (parallel to the rod walls) ϕ-direction, can also be seen.

Figure 2.3 shows the contour plot of the measured axial velocity. At the bottom left corner of figure 2.3 there is also a scheme where the shaded area is the region for which the contour plots had been created.

The mean velocity, $\overline{U}$, is normalized by the velocity kept constant by a fixed Pitot tube, $\overline{U}_{REF} = 27.74$ m/s. In the experiment, velocity data were obtained by

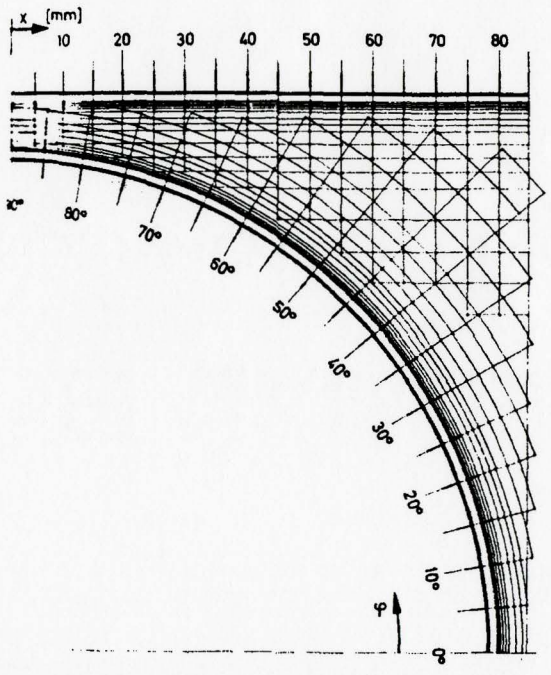

Figure 2.2: Distribution of the measurement positions. Adapted from Rehme [43]

using a cylindrical coordinate system for the part close to the cylinder wall and a cartesian coordinate system for the region close to the channel wall. In this way, two graphs were plotted separately and they are connected by the maximum velocity line. Because the contour plots at each region were drawn seperately from each other, an inconsistency of the contour lines at the maximum velocity line is observed.

As shown in figure 2.3, the maximum velocity line is at the core region of the channel. The ratio of the maximum velocity (on the symmetry line) and the maximum velocity in the gap between the rod and the channel wall is 1.38. Rehme also calculated the axial velocity using the VELASCO code and he found the value of the above ratio to be 1.62. Based on his statement, the difference of the two

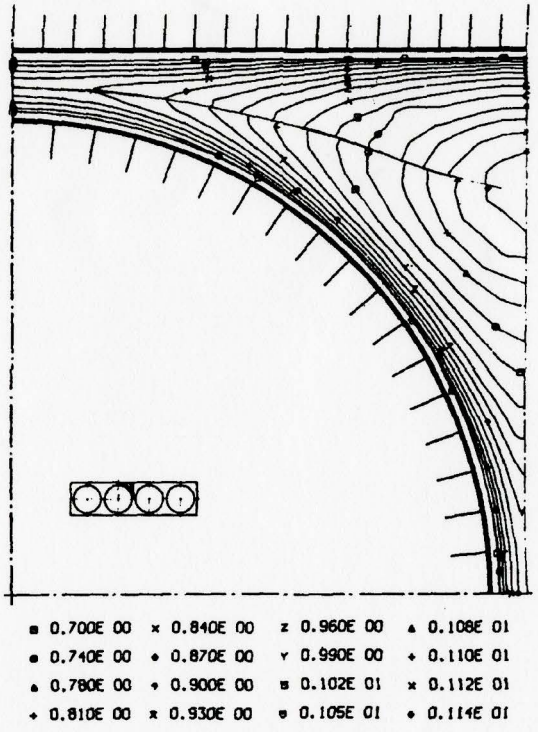

Figure 2.3: Axial normalized velocity ($\frac{\overline{U}}{\overline{U}_{REF}}$) distribution. Adapted from Rehme [43]

ratios is likely due to the larger circumferential eddy diffusivity than the radial eddy diffusivity.

The law of the wall is expressed for a smooth pipe by [41]:

$$u^+ = \frac{1}{\kappa} \ln y^+ + B \tag{2.6}$$

where κ is the Von Karman constant and B is an empirical constant. For smooth pipes, Nikuradse [38] determined the constants by fitting equation 2.6 to his experi-

mental data. Specifically, the values of the two constants are:

$$\kappa = 0.4, B = 5.5 \tag{2.7}$$

Rehme investigated the applicability of the law of the wall for a circular pipe to a rod bundle geometry. From his measurements, he found that the Von Karman constant in a rod bundle is the same as for the smooth pipe case and that B is equal to 5.0. So, for rod bundle flows, the law of the wall is modified to the following expression:

$$u^+ = 0.4 \ln y^+ + 5.0 \tag{2.8}$$

where: $y^+ = \frac{r}{\phi}$, for the region near the rod wall, or: $y^+ = \frac{x}{y}$, for the region near the channel wall. Here, r and y are the distances from the rod wall and the channel wall, respectively. In figure 2.2, the ϕ-angle, and the x-direction can be seen.

2.2.3 Secondary flows

Experimental data have shown that secondary flows exist in circular as well as in non-circular geometries such as square, rectangular and triangular ducts, which all have corners ([5], [1]). The generation of the secondary flows is due to gradients of the Reynolds stresses. This type of secondary flows are called secondary flows of Prandtl's second kind.

Renksizbulut and Hadaller [49] provide a schematic of secondary flow patterns

in a rod bundle geometry. This schematic is shown in figure 2.4, where θ is the azimuthal angle. In the top upper left corner of figure 2.4 there is a circulation region moving fluid elements from the core to the rod-to-wall gap and then along the channel wall toward the symmetry line (dashed line) which divides the regions of the two illustrated rods. On the right of this circulation region there is another one which moves fluid elements in a similar manner, but closer to the rod wall. On the right of the latter circulation, there is another circulation zone close to the rod-to-rod gap, which carries fluid elements down the center line and returns them to the core along the rod wall.

Several investigators performed experiments to study the effect of secondary flows on the axial velocity and the turbulence distributions. Rehme [43] and Seale [58] measured axial velocity distributions in a wall subchannel, but did not clearly report 'bulging' in the axial velocity distributions. On the other hand, the bulging of the axial velocity contour plots was reported by other authors, such as Renksizbulut and Hadaller [49] and Meyer and Rehme [34]. The bulging of the mean axial velocity distribution due to the presence of secondary flows, can be observed by comparing figure 2.4 with figure 2.5, where $\overline{u}$ is the mean velocity field and u_{AVG} is the measured test section average flow velocity. For example, the constant velocity lines at the top left corner in figure 2.5 are seen to be curved in a manner suggestive of the presence of the flow cells at the top left corner in figure 2.4.

In addition, experimental results [55] reported bulging in the turbulence in-

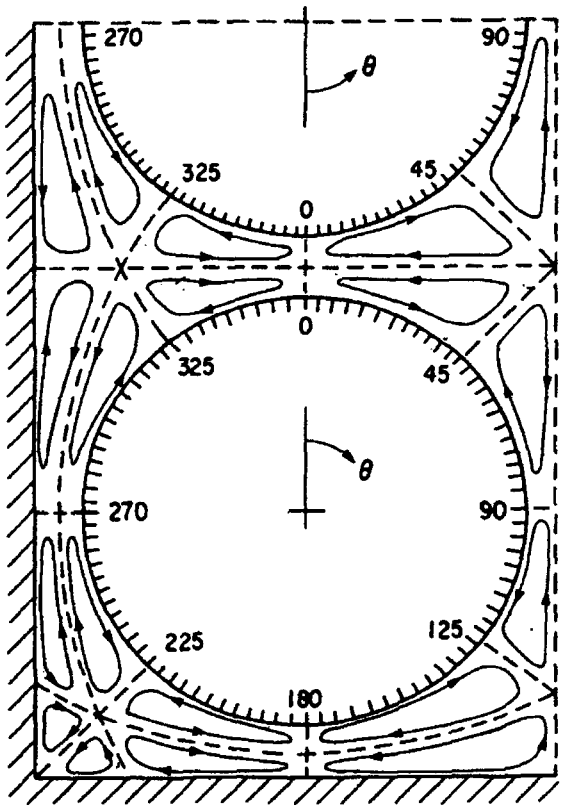

Figure 2.4: Secondary flows. Adapted from Renksizbulut and Hadaller [49]

tensity distribution which seems to be due to secondary flows. Rowe et al. [55] are likely the first to investigate bulging in the tudbulence intensity in a rod bundle geometry. They inferred the secondary flow behaviour in a rod bundle geometry, using the secondary flow behaviour in a square duct. It was stated that secondary flows move toward the gaps, thus cause the turbulence intensity lines to bulge toward the gaps.

Secondary flows were also easily detected from the measurements of the wall shear stress distribution. Rehme [43], [44] found that the measured wall shear stresses

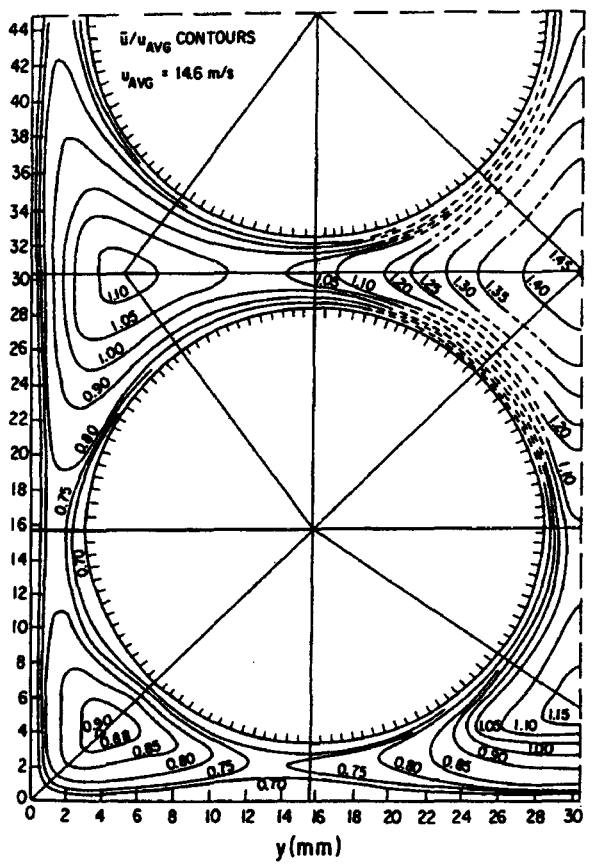

Figure 2.5: Normalized axial velocity ($\frac{\overline{u}}{u_{AVG}}$) contours. Adapted from Renksizbulut and Hadaller [49]

are much more uniformily distributed than the respective calculated values. This was because his model did not include secondary flows. Seale [58] examined the same behaviour of the wall shear stress distribution and calculated the turbulent flow with and without secondary flow source terms. The case for which secondary flows were included provided the same shear stress distribution as the measured one. In his study, Seale [58], showed the effect of the secondary flows in the wall shear stress distribution, by comparing the predictions with isotropic effective diffusivities for

turbulent flow in rod bundles. Basically, secondary flows cause the displacement of the position of the maximum shear stress.

Secondary flows in rod bundle geometries have proved to be very difficult to measure. Some of the earliest attempts to measure secondary flows, such as the ones by Trupp and Azad [66] and Carajilescov and Todreas [8] were not successful. This could be due to geometrical tolerances of the test sections, which caused cross-flow or due to experimental inaccuracy [55], [66], [67]. Seale [61] attempted to measure secondary flows in a rod bundle geometry with high geometric precision. In this experiment, the overall uncertainty of the secondary velocity parallel to the top wall was estimated to be about $\pm 0.06 u_\tau$. The maximum secondary velocity parallel to the top plate wall is about 1.5% of the bulk velocity and it occurs near the walls on the outward secondary flow from the corners of the duct. He also reported two large rotating cells between the flat wall and the rod and one cell in the gap region between the rod and the vertical axis of the duct.

Aly [1] measured the magnitude of secondary velocities in equilateral triangular duct at a Reynolds number range of $53,000 \sim 107,000$. The maximum secondary velocities were 1.5% of the bulk axial velocity.

2.2.4 Reynolds stresses

For small pitch-to-diameter and wall-to-diameter ratios, the turbulent flow structure through rod bundles differs significantly with comparison to simple channel flows like

circular tubes and parallel plates. Rehme [43] measured the turbulent intensities and the Reynolds shear stresses in a rod bundle geometry with a pitch-to-diameter ratio of 1.07. As already mentioned, the distribution of the positions at which measurements were taken, is shown in figure 2.2.

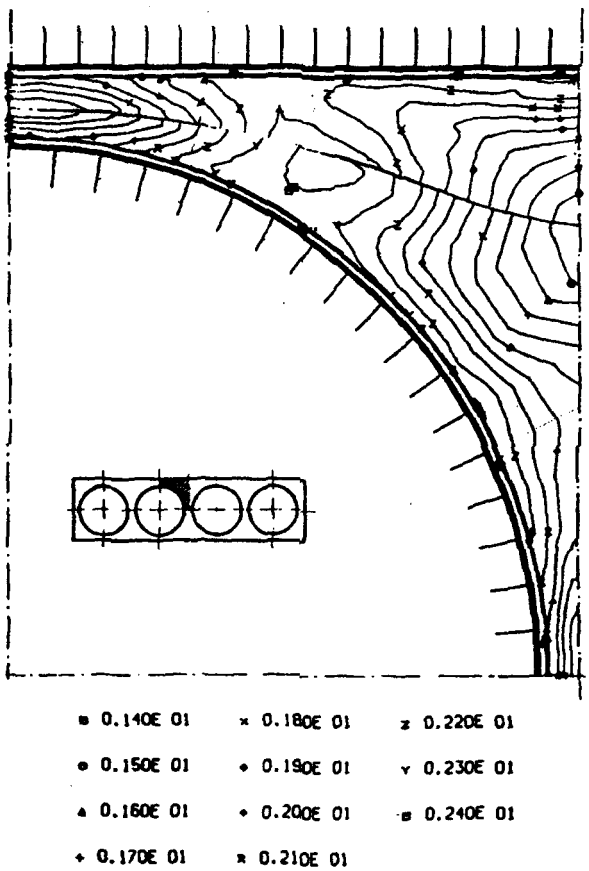

Figure 2.6: Axial turbulence intensity distribution normalized by the friction velocity, $\frac{\sqrt{\overline{u'^2}}}{u^*_{REF}}$. Adapted from Rehme [43]

Figure 2.6 shows the axial turbulence intensity distribution, normalized by the wall shear velocity on the rod at $5^0(u^*_{REF})$. In the figure, the maximum axial

turbulence intensity is placed at about 55^0 from the rod-to-wall gap. At that point the axial turbulence intensity is about 2.4 times higer than the friction velocity. The minimum axial intensity is observed in the core of the subchannel. This axial turbulence intensity distiribution is also observed in the turbulent kinetic energy distribution.

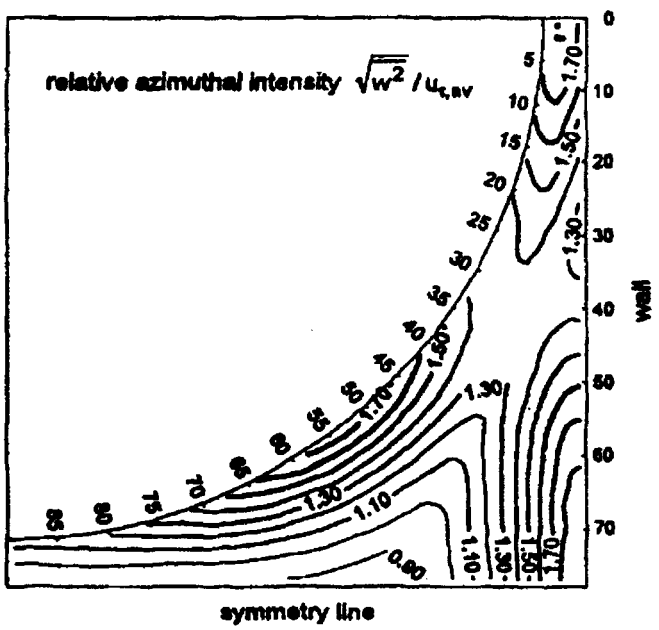

Figure 2.7: Azimuthal turbulence intensity distribution normalized by the average friction velocity, $\frac{\sqrt{\overline{w'^2}}}{u_{\tau,av}}$. Adapted from Krauss and Meyer [30]

Figure 2.7 provides the azimuthal (parallel to the rod walls) turbulence intensity, $\sqrt{\overline{w'^2}}$, which is normalized by the friction velocity, $u_{\tau,av}$, measured by Krauss and Meyer [30]. On the interior of the rod wall, the measuring positions can be seen. Unlike the axial turbulence intensity, the maximum azimuthal turbulence intensity

is found in the rod-to-wall gap. The maximum value is about 1.7 times the friction velocity. The azimuthal turbulence intensities were roughly 30% lower than the axial turbulence intensities.

Rehme [46] investigated the change of the maximum axial and circumferential turbulence intensity with pitch-to-diameter ratio $\left(\frac{P}{D}\right)$ and wall-to-diameter ratio $\left(\frac{W}{D}\right)$. He observed the following:

1. The axial and azimuthal turbulence intensity increases with decreasing $\frac{P}{D}$ ratio near the rod-to-rod gap.

2. The axial and circumferential turbulence intensity increases with decreasing $\frac{W}{D}$ ratio near the rod-to-wall gap.

The following correlations were drawn from the measurements:

$$\frac{u'}{u_\tau} = 0.6 + 0.307\left(\frac{W}{D} - 1\right)^{-\frac{2}{3}} \tag{2.9}$$

$$\frac{w'}{u_\tau} = 0.6 + 0.0425\left(\frac{W}{D} - 1\right)^{-\frac{4}{3}} \tag{2.10}$$

Other investigators [55], [26], [69] found similar trends for the axial and circumferential turbulence intensity with the $\left(\frac{P}{D}\right)$ or $\left(\frac{W}{D}\right)$ ratio. The reason for this behaviour was explored by Hooper and Rehme [26]. They investigated the periodic behaviour of the auto and cross-correlations of the axial and circumferential turbu-

lence intensities. They stated that this periodic behaviour results in high momentum exchange between subchannels. This is called the flow pulsation phenomenon, which is discussed in the following section.

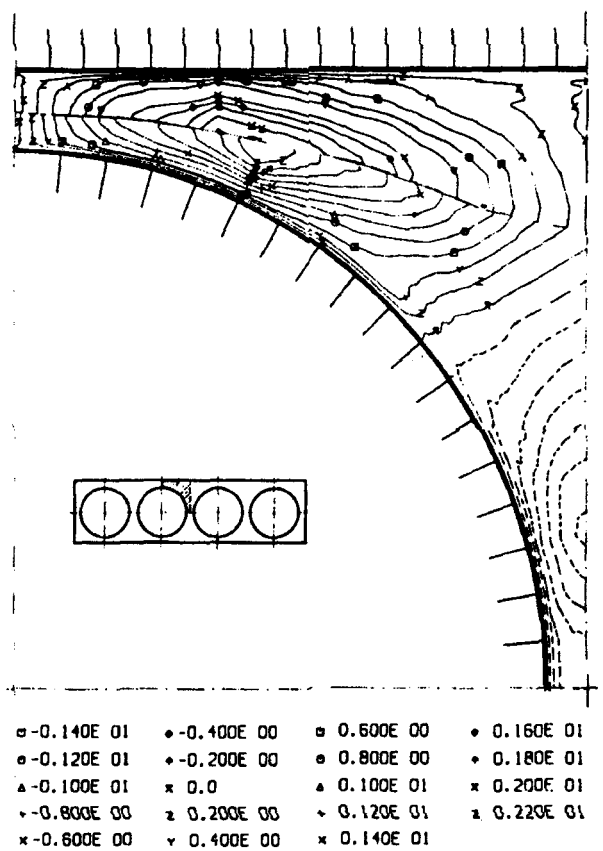

Figure 2.8: Distribution of the normalized azimuthal Reynolds shear stress, $\frac{\overline{u'w'}}{u^{*2}_{REF}}$. Adapted from Rehme [43]

The radial (normal to the rod wall) and circumferential (parallel to the rod wall) Reynolds shear stresses in rod bundles were measured by Rehme [43] and Krauss and Meyer [30]. The radial Reynolds shear stress, $-\rho\overline{u'v'}$, decreases with increasing distance from the wall. The azimuthal Reynolds shear stress is more important to

turbulent mixing between subchannels. Figure 2.8 shows the measured circumferential turbulence shear stress distribution. The value of the maximum shear stress is $2.2u^{*2}_{REF}$ at the angle of 65^0 (measuring positions: see figure 2.2). At an angle of around 40^0 the Reynolds shear stress is zero. The important conclusion that has to be drawn from these measurements is that high shear stresses are found away from the gaps. This fact suggests the existence of large scale periodic flow pulsations, which is discussed in the following subsection.

2.2.5 Periodic flow pulsations

Experimental studies of turbulent inter-subchannel thermal mixing for single-phase flows using relatively simple subchannel geometries have indicated that complex turbulent flows can arise. For example, Meyer [33] found that the azimuthal eddy-viscosity is higher than the radial eddy-viscosity away from the rod, especially in the gap region, by a factor of between three and four. In a pipe, this ratio is at most two [59]. There is thus strong anisotropy in the eddy diffusivity.

Rowe et al. [55] performed an experimental study to investigate the effect of the flow channel geometry on fully developed turbulent flow in channels with rod bundles. The experiments were performed with water and a Reynolds number of $50,000 \sim 200,000$. The pitch-to-diameter ratio was $1.125 \sim 1.25$. The autocorrelation function and the velocity and turbulence intensities were measured. It was pointed out that the periodic behaviour, observed in the autocorrelation functions

indicates a dominant frequency of turbulence. As the rod gap spacing is reduced, the dominant frequency of turbulence is increased. Furthermore, this frequency is insensitive to the Reynolds number. Limited data of the radial turbulence intensity was also obtained. It was concluded that macroscopic flow processes exist near the rod-to-rod gap. This increased turbulence intensity indicates an enhancement of cross-flow mixing.

Experiments of Hooper [25] and Hooper and Rehme [26] indicated that the axial and circumferential turbulent velocities have a clear periodic large-scale structure. More specifically, Hooper and Rehme [26] made more detailed measurements of the mean axial velocity, all the six Reynolds stresses and they came up with auto and cross-correlations of turbulence intensities. The measurements were made in a wall bounded rod array and a square pitch rod cluster. Spatial auto and cross-correlation functions were measured at four positions on the symmetry line between two rods, labeled as 1, 2, 3, 4 and corresponding to y-distances of 0, -10, 5 and 10 mm, respectively. So, point 1 was exactly at the center of the rod-to-rod gap and the relative to point 1 positions of the other three points can be understood from their above distances.

It was found that the axial and circumferential turbulent velocities clearly have a periodic behaviour and their peak values were about 25% of the mean axial velocity, while the radial turbulent velocities do not have a periodic character. In addition, the high magnitude of the circumferential Reynolds shear stress is also associated with

the large scale structure of the circumferential turbulent velocity.

In order to resolve the large scale structure, the auto and cross-correlation functions were obtained. From the autocorrelation results, the axial turbulent velocities showed a periodic component with a peak frequency of 92 Hz for the locations 2 and 4, while the periodic behaviour was not observed at location 1. This periodic character was also obtained in Rowe's experiment. Moreover, Hooper and Rehme found the same periodic behaviour in the circumferential turbulent velocity at all four locations with the same frequency as the frequency of the axial turbulent velocity. The spatial correlation showed that there is a phase shift of 180^0 in the axial turbulent velocities for the locations 2 and 4, while no phase shift was observed in the circumferential turbulent velocity.

Therefore, the axial and circumferential turbulent velocity has a large scale structure with a phase shift. The long length scales of the axial and circumferential turbulent velocities, relative to the gap width, emphasize the anisotropy of the turbulent transport processes at the rod gap. It is considered that this periodic large scale structure in the circumferential turbulent velocity causes periodic momentum exchange through the rod-to-rod gap.

Möller [36] developed a phenomenological model to describe the formation of large eddies near the gaps by adopting the coherent structure concept [27] in the gap regions of rod bundles. In his study, similarly to Hooper and Rehme [26], Möller [36] found peaks at characteristic frequencies in the power spectra of the turbulent

velocity fluctuations in the axial direction and in the direction parallel to the walls. He established a relationship between the gap width and the non-dimensional frequency, the Strouhal number, which was defined with the characteristic frequency, f, the rod diameter, D, and the friction velocity, u_τ:

$$Str = \frac{fD}{u_\tau} \tag{2.11}$$

The large-scale eddies move almost periodically through the gaps of the rod bundles at the characteristic frequency. Similarly to Rowe et al. [55], he found that the characteristic frequency, as well as the maximum value of the power spectra increase with decreasing gap width.

Guellouz and Tavoularis [21], [22] did a comprehensive study on the structure of turbulent flow in a rectangular channel containing a cylindrical rod, focusing on the gap between the rod and a plane wall. Reynolds averaged and phase averaged measurements were performed to characterize the features of the large-scale structures. The presence of large-scale, quasi-periodic structures in the vicinity of the gap for a range of gap widths was demonstrated through flow visualization, spectral analysis and space-time correlation measurements. The measurements identified large-scale structures with a field of a street of three dimensional, counter rotating vortices, whose convection speed and stream-wise spacing were found to be functions of the gap width. Phase-averaged measurements identified the structures as coherent vortical structures with instantaneous phase-correlated vorticity.

A few suggestions have been made on the mechanism of developing periodic behaviour in the turbulence intensities. Hooper and Rehme [26] contended that the 180^0 phase shift in the axial turbulence intensity between points 2 and 4 may be the cause of intersubchannel instability stemmed in the periodic behaviour. It is said that if the mass flow in one subchannel decreases, local axial pressure gradient also decreases, with the generation of a transverse pressure difference between the subchannels. The increasing magnitude of the pressure driven intersubchannel instability may lead to the selective amplification or excitation of the axial and circumferential components of the turbulence intensities.

From the different turbulent structural investigations, a general consensus is derived. The large-scale coherent structures are found to exist in any longitudinal slot or groove in a wall or a connecting gap between two flow channels, provided that certain geometrical restrictions are satisfied. These structures are generated in both isothermal and non-isothermal flow conditions. The peaks in the power spectra are found to be highest for the fluctuating velocity components parallel to the walls directly in the gaps. With decreasing gap width, the peaks become narrower in the frequency range and they reach higher maximum values. This means that the average velocity through the gaps increase with decreasing gap width. For higher gap widths, the peaks broaden and the maximum values of the power spectras decrease. The large eddies move almost periodically through the gaps of rod bundle geometries at a characteristic frequency.

2.2.6 Turbulent eddy diffusivity and anisotropy

The turbulent eddy diffusivity of momentum or heat is used to describe the anisotropic turbulent properties in a rod bundle geometry.

The turbulent eddy diffusivity of momentum is defined as the ratio of the Reynolds stresses to the mean velocity gradients. In a circular pipe, the radial eddy diffusivity was obtained by Reichardt [48]. The eddy diffusivity increases from the wall and then reaches a constant value at the core of a circular pipe. For the rod bundle geometry, the eddy diffusivity distribution is different from that of a circular pipe.

Rehme [45] defined the axial, radial and circumferential components of the turbulent eddy diffusivity of momentum as:

$$\varepsilon_M^x = \frac{-\overline{u'^2}}{\overline{\frac{\partial U_x}{\partial x}}},\ \varepsilon_M^r = \frac{-\overline{u'v'}}{\overline{\frac{\partial U_r}{\partial r}}},\ \varepsilon_M^\phi = \frac{-\overline{u'w'}}{\overline{\frac{\partial U_\phi}{r\partial \phi}}} \tag{2.12}$$

where $U_i\,(i = x, r, \phi)$ is the time mean velocity and u', v' and w' are the velocity fluctuations in the axial, x, radial, r and azimuthal or circumferential, ϕ direction, respectively.

The dimensionless eddy diffusivities were also defined as follows:

$$\varepsilon_M^{x+} = \frac{\varepsilon_M^x}{Lu_\tau},\ \varepsilon_M^{r+} = \frac{\varepsilon_M^r}{Lu_\tau},\ \varepsilon_M^{\phi+} = \frac{\varepsilon_M^\phi}{Lu_\tau} \tag{2.13}$$

where L is the normal distance from the walls to the maximum velocity line. The measurement of the eddy diffusivity was made in a rod bundle with the pitch-to-diameter ratio of 1.07 and at a Reynolds number of $8.7 * 10^4$. From the measurements it was found that the maximum value of the dimensionless circumferential eddy diffusivity, $\varepsilon_M^{\phi+}$, equal to 20 or higher, was located near the gap regions. This value is 260 times higher than the maximum value of the dimensionless radial eddy diffusivity in a circular pipe $\left(\varepsilon_M^{r+} = 0.0075\right)$. The maximum value of the dimensionless radial eddy diffusivity in the rod bundle was about 0.18. Thus, the strong anisotropy in the eddy diffusivity was revealed with an anisotropy factor above 100. This anisotropy of the eddy diffusivity was also confirmed by Trupp and Azad [66].

Rehme [47] showed that the circumferential turbulent eddy diffusivity of momentum, which was measured near the gaps, strongly increases with decreasing pitch-to-diameter ratio. He summarized his results in the following correlation:

$$\varepsilon_M^{\phi+} = 0.0177 \left(\frac{S}{D}\right)^{-2.42} \tag{2.14}$$

where S represents the gap spacing width.

The radial eddy diffusivity of momentum does not depend on the angular position in a rod bundle geometry. It increases from the rod wall surface, similarly to the case of a circular pipe. Away from the rod wall the eddy diffusivity deviates from the circular pipe case, with a value of two times higher.

Seale [59], [58] presented some anisotropic factors at the gap of a wall sub-

channel. He asserted that the circumferential eddy diffusivities are much higher than the radial ones, as observed in Rehme's experiment. It was also mentioned that the anisotropy factor increases as the pitch-to-diameter ratio is reduced. The anisotropy factor ranged from $3 \sim 30$ with a pitch-to-diameter ratio of $1.1 \sim 1.8$

The eddy diffusivities of heat are defined as the ratio of the turbulent heat flux to the temperature gradient:

$$\varepsilon_H^x = \frac{-\overline{u'T'}}{\frac{\overline{\partial T}}{\partial x}}, \quad \varepsilon_H^r = \frac{-\overline{v'T'}}{\frac{\overline{\partial T}}{\partial r}}, \quad \varepsilon_H^\phi = \frac{-\overline{w'T'}}{\frac{\overline{\partial T}}{r\partial \phi}} \tag{2.15}$$

The dimensionless eddy diffusivities of heat were defined as:

$$\varepsilon_H^{x+} = \frac{\varepsilon_H^x}{Lu_\tau}, \quad \varepsilon_H^{r+} = \frac{\varepsilon_H^r}{Lu_\tau}, \quad \varepsilon_H^{\phi+} = \frac{\varepsilon_H^\phi}{Lu_\tau} \tag{2.16}$$

Krauss and Meyer [30] provided eddy diffusivities of heat in a wall subchannel of a heated 37-rod bundle $\frac{P}{D} = 1.12$, $\frac{W}{D} = 1.06$. The maximum value of the dimensionless circumferential eddy diffusivity of heat was found at $20 \sim 30^0$ from the rod-to-rod gap and it was about 20. The maximum value of the dimensionless radial eddy diffusivity of heat was located at the symmetry line and it was about 0.18. Thus, the same anisotropy factors are obtained for heat as well as for momentum. In addition, the radial turbulent Prandtl number, which is defined as the ratio of the eddy diffusivity of momentum and the eddy diffusivity of heat in the radial direction, was about $2 \sim 2.5$ near the heated wall and it decreases with increasing distance

from the heated wall, reaching unity at the symmetry line which is the same as for a circular pipe flow.

2.3 Turbulent Interchange Mixing

2.3.1 Subchannel models for turbulent interchange mixing

Turbulent interchange mixing between subchannels is modelled using a subchannel approach. With this approach, the averaged enthalpy or temperature over a subchannel is used to determine the mixing rate. Consider two subchannels, i and j, with bulk enthalpies of h_i and h_j, respectively. Assume that turbulent mixing causes the flow across the gap between the two subchannels at a mass flow rate, w, and at a mass velocity, v. This mass flow rate or mass velocity is a fictitious property, equal to the real mass transfer which would be needed to carry the observed amount of heat from one subchannel to the other.

The conservation of mass through the subchannels yields:

$$w = \rho v S \tag{2.17}$$

where S is the gap spacing width. The transported heat between the subchannels per unit axial length is modelled as a diffusive process, using a turbulent eddy diffusivity,

ε_{ij}^{H} as the diffusion constant [9].

$$q' = -\rho\varepsilon_{ij}^{H}\left(\frac{\partial\overline{h}}{\partial z}\right)_{ij} S \tag{2.18}$$

The gradient of enthalpy, $\overline{h}$, in equation 2.18 is linearized as:

$$\left(\frac{\partial\overline{h}}{\partial z}\right)_{ij} \cong \frac{h_j - h_i}{\Delta z_{ij}} \tag{2.19}$$

where Δz_{ij} represents the 'mixing distance' between the subchannels and it is often set to the centroidal distance between the two subchannels, δ_{ij}. Substitution of equation 2.19 into equation 2.18 provides:

$$q' = -\rho\varepsilon_{ij}^{H}\frac{h_j - h_i}{\delta_{ij}} S \tag{2.20}$$

As an alternative expression, the heat exchanged between the subchannels is given in the following equation, using the turbulent mixing flow rate, w [53]:

$$q' = w\left(h_j - h_i\right) S \tag{2.21}$$

The turbulent mixing flow rate is obtained by equating equation 2.20 to equation 2.21 and it is given by:

$$w = \rho S\frac{\varepsilon_{ij}^{H}}{\delta_{ij}} \tag{2.22}$$

Dimensionless mixing factors are often used to represent the degree of turbulent mixing between subchannels. Ingesson and Hedberg [29] introduced a mixing factor in terms of the mixing velocity, v, the mixing distance, δ_{ij}, and the reference eddy diffusivity, $\bar{\varepsilon}$, which is given by:

$$Y = \frac{v\delta_{ij}}{\bar{\varepsilon}} \tag{2.23}$$

This factor can be considered as a multiplier which accounts for how much higher the eddy diffusivity in rod bundles is in comparison with a reference eddy diffusivity. Usually, the eddy diffusivity of a circular pipe is used as the reference mixing eddy diffusivity. Rehme [47] provided a reference eddy diffusivity using a friction coefficient, f:

$$\bar{\varepsilon} = \frac{\nu}{20} Re \sqrt{\frac{f}{8}} \tag{2.24}$$

The second dimensionless mixing factor is a mass Stanton number used by several authors [53], [51]. The definition of the number is the ratio of the mixing flow rate to the axial mass flow rate, which is given by:

$$M_{ij} = \frac{w}{\rho U_b S} \tag{2.25}$$

A third dimensionless mixing factor, the gap Stanton number is defined as the

ratio of the mixing velocity, ν, to the axial bulk velocity, U_b, which is given by [12]:

$$St_g = \frac{\nu}{U_b} \tag{2.26}$$

Replacing the mixing velocity, using equation 2.17 and equation 2.22 gives the following expression for the gap Stanton number:

$$St_g = \frac{q'}{\rho C_p U_b S\,(T_j - Ti)} \tag{2.27}$$

where the temperatures T_i and T_j correspond to the bulk temperatures of subchannels i and j, respectively.

The fourth mixing factor is the mixing number, w/μ, which is defined as the mixing flow rate divided by the molecular viscosity [52]. The four mixing factors mentioned above are interchangeable. In order to compare the mixing factors used by different authors, all the mixing factors are converted into a gap Stanton number in the following:

$$St_g = \frac{\nu}{U_b S}\frac{w}{\mu} = \frac{\overline{\varepsilon}}{U_b \delta_{ij}} Y = \frac{\rho\nu}{\mu} M_{ij} \tag{2.28}$$

2.3.2 Contribution of flow pulsations and secondary flows to turbulent mixing

In subsections 2.2.3 and 2.2.5 the contribution of the secondary flows and the large scale flow pulsations in axial turbulent flows through rod bundle geometries is being discussed. Due to its importance, this discussion is extended and summarized in this subsection.

As it is already mentioned, it is generally accepted that turbulent cross-flow mixing, as well as the amount of heat transfer between the adjacent subchannels are dependent on gap spacing. As gap spacing is reduced, the heat flow from the rod to the gap may remain constant. This fact was confirmed by several experimental results [29], [54].

Rowe et al. [55] explained this behaviour of turbulent mixing flow rate by adopting the mass Stanton number in equation 2.25 based on D instead of S. Substitution of equation 2.22 into equation 2.25 yields the following equation:

$$M_{ij} = \frac{w}{\rho U_b D} = \frac{\varepsilon_{ij}^H}{U_b D} \frac{S}{\delta_{ij}} \tag{2.29}$$

From equation 2.29 it is seen that the mass Stanton number is linearly proportional to the eddy diffusivity and the gap spacing. As the gap spacing is reduced, the eddy diffusivity should be increased to satisfy the fact that the mass Stanton number is insensitive to the rod gap spacing.

Seale [59] observed that strong anisotropy in the eddy diffusivity was found through investigations of heat transfer across rod bundles. As mentioned in subsection 2.2.6, the azimuthal eddy diffusivity of heat in the gap region was much higher than the radial eddy diffusivity. The anisotropic diffusivities are thought to be the reason for high mixing in narrow gaps of rod bundles.

The increase of the eddy diffusivity near the gaps is mainly associated with the flow pulsation phenomenon. According to Hooper and Rehme's experiment [26] high turbulence intensity near the gap influences high momentum exchange between subchannels. Moreover, the periodic behaviour of turbulence intensity provides evidence of the periodic flow pulsation occurring near the gaps.

It is of interest to assess how much secondary flows contribute to mixing interchange compared with the contribution of the anisotropic eddy diffusivity. In order to explore the effect of secondary flows on mixing, several numerical investigations on this issue have been made.

Seale [60] investigated the change of the gap Stanton number due to secondary flows. He calculated the gap Stanton number with and without secondary flows. He concluded that secondary flows increased the gap Stanton number by 10 to 15%. Hence, experimental gap Stanton numbers were still under estimated by the turbulence models used by Seale, even if secondary flows were included. From this investigation it was concluded that contribution of secondary flows to mixing is not significant and it is much lower than the contribution of the anisotropic eddy diffu-

sivity. By augmenting the circumferential eddy diffusivity using an anisotropy factor, determined from experimental data, the experimental gap Stanton number was able to be reproduced.

Bartzis and Todreas [3] used a similar approach to Seale's in order to investigate the contribution of secondary flows to mixing. Their results revealed that the use of an anisotropic eddy diffusivity reproduced the experimental axial velocity. With an isotropic eddy diffusivity, axial velocity was underpredicted, regardless of the inclusion of secondary flows. Therefore, it was concluded that the anisotropic eddy diffusivity has a greater impact on the axial velocity than the secondary flow. In addition, the temperature distribution was strongly dependent on the eddy diffusivity from their heat transfer calculation.

Summarizing, the main conclusion of this review is that the contribution of the secondary flows to the anisotropy of the flow field is very small. What makes the flow highly anisotropic, with high axial and azimuthal turbulence intensities in the gap regions, and is responsible for the high mixing rates between the subchannels, is the existence of the periodic flow pulsations across the gaps in the rods.

2.3.3 Overview of the relevant numerical investigations

In this subsection an overview of the numerical investigations, relevant to this research work, is carried out.

A number of attempts have been made to predict the turbulent flow and mixing

in rod bundles using computational fluid dynamics (CFD). Unlike the safety analysis codes described in the introduction, CFD codes solve the conservation equations for mass, momentum, and energy on sufficiently fine grids, so that constitutive relationships for pressure drop or heat transfer coefficient are not required. If a Reynolds Averaged Navier-Stokes (RANS) solver is applied, then special models are required for the turbulence.

Rock and Lightstone [50] assessed the applicability of the $k-\varepsilon$ model by applying the model to Seale's experiment [59] which considered turbulent air flow in a twin subchannel geometry. They found that the $k-\varepsilon$ model favourably predicted the radial component of the turbulent eddy viscosity, but underpredicted the azimuthal component. Thus, the $k-\varepsilon$ model failed to reproduce the experimental turbulent mixing. In addition, the $k-\varepsilon$ model was unable to predict secondary flows. This was expected since secondary flows arise from anisotropy in the turbulence and the $k-\varepsilon$ model is unable to predict that anisotropy.

Higher-order turbulence models are thus necessary for prediction of secondary flow. Launder and Ying [31] proposed an algebraic stress model for normal and shear stresses which was derived by simplifying the corresponding transport equation proposed by Hanjalic and Launder [23]. The applied length scale was obtained from the geometrical formulation suggested by Buleev [6]. A number of authors have applied Launder and Ying's model to estimate secondary flows in a rod bundle [1], [58]. Gessner and Emery [19] pointed out that Launder and Ying's model predicted

secondary flow streamlines very well, but significantly underpredicted the turbulence kinetic energy. Demuren [15] suggested that the underprediction of Launder and Ying's model to a rod bundle is due to secondary velocity gradients neglected in the model. They applied Naot and Rodi's model [37] and Demuren and Rodi's model [16] which include secondary velocity gradients by eddy viscosity type relations. Both models were able to produce secondary velocities in square and rectangular ducts as well as in rod bundles.

Chang and Tavoularis [10] used an unsteady RANS approach to simulate an isothermal flow in a channel containing a single rod. They used an RNG $k-\varepsilon$ model to predict the turbulence in conjunction with a timestep that was small relative to the timescales of the large scale structures. The goal of that exploratory work was to see if the flow pulsations (which appear as coherent structures) could be predicted by a RANS model. Interestingly, they found that such structures were predicted during the transient phase of the simulation. Eventually, the flow became steady and the structures washed out. For comparison, simulations were also performed using Large Eddy Simulation (LES) with a Smagorinsky subgrid model. The LES simulations also showed structures with a periodic oscillation across the gap between the base of the rod and the wall. Predictions were compared to experiments and it was seen that the $k-\varepsilon$ RANS results significantly overpredicted the flow oscillations timescale and the stream-wise spacing. The LES simulation underpredicted the timescale and overpredicted the spacing. On close examination of the LES results, however, it was

seen that the grid used was too coarse. This means that much of the turbulent kinetic energy was not modelled directly as a result of the filtering process.

Chang and Tavoularis [10] extended their project by modelling the problem using the Reynolds Stress Model. Again, by running an unsteady simulation with an appropriate timestep, they found that they were able to predict the presence of coherent structures. Biemüller [4] performed LES simulations to predict the pulsations occurring in the gap connecting two rectangular channels. To reduce computational effort, their domain represented only a portion of the actual channels with periodic boundary conditions applied at the inlet and the outlet of the domain. They also used a coarse grid $(8 * 8)$ in the gap region and applied wall functions to treat the no-slip walls. Because of the inherent differences between the simulated geometry and the experimental geometry, quantitative agreement was not obtained. Nonetheless, the LES simulations are promising since they were able to capture the large-scale flow pulsation in the gap.

Heavy liquid metals are used as coolant for an accelerator driven sub-critical system. Cheng and Tak [14] performed a CFD analysis on the thermal-hydraulic behaviour of heavy liquid metal flows like lead-bismuth eutectic in subchannels of both triangular and square lattices. The effects of parameters like turbulence models and the P/D ratio on the thermal-hydraulic behaviour were studied. It was found that only second order closure turbulence models could faithfully reproduce secondary flows. For the range of Reynolds number considered, the amplitude of secondary flows

was found to be less than 1% of the mean flow. It was found that turbulence had a strong anisotropic behaviour in the gap region. These findings were in accordance with previous CFD subchannel studies. The turbulence behaviour was found to be the same for both triangular and square lattices. From a heat transfer point of view it was observed that the heat transfer coefficient (Nusselt number) had a strong circumferential non-uniformity in tight rod bundles. This clearly suggests that the subchannel analysis codes used in nuclear industry which rely on an averaged approach cannot faithfully reproduce the exact flow and heat transfer field in rod bundles with small P/D ratio. The non-uniformity should be taken into consideration, due to the importance of local cladding temperature to the corrosion behaviour.

Tóth and Aszódi [65] carried out a CFD analysis on the fluid flow and heat transfer in a VVER-440 fuel assembly (Russian PWR). The BSL Reynolds Stress model was used in their investigation based on the fact that this model could reproduce the flow field in a triangular rod bundle more accurately as compared to other two equation or Reynolds stress models. Two different rod bundles were examined: one without spacer grid and one with spacer grid. Similar boundary conditions were used in both cases to investigate the mixing process. In the geometry without spacer grids it was found that the secondary flows are symmetric to the subchannel walls and they do not cause convective mixing between adjoining subchannels. For the rod bundle with spacer grids, it was found that the secondary flows are more intense and that they can cause convective mixing between the subchannels. CFD analysis

should take into account the effect of spacer grids.

Ikeno and Kajishima [28] performed an LES study of turbulence in a rod bundle geometry without heat transfer. The computational domain comprised of four subchannels which were large enough to capture the large scale structures. The LES study was performed for three different values of P/D ratio. The lateral flow was found to be not confined to a subchannel, and there was strong indication of a pulsating flow through the rod gaps between subchannels. The intensity of the gap flow increased as P/D increased. The turbulence intensity profile in the rod gap suggested that the flow pulsation was caused by the turbulence energy transferred from the main flow to the wall-tangential direction.

Chapter 3

Mathematical Modelling

3.1 Overview: Brief History of Turbulence Modelling

Reynolds developed the time averaged Navier-Stokes equations in the late nineteenth century from his research on turbulence. The earliest attempts in developing a mathematical description of the turbulent stresses, which is the core of the closure problem, were performed by Boussinesq with the introduction of the eddy viscosity concept. However, it was not until 1920, that the first successful calculation of the practical turbulent flow was achieved, based on the Reynolds averaged Navier-Stokes equations with an eddy viscosity model.

Prandtl came up with his pioneering research in 1925 and proposed the concept of mixing length as a basis for the determination of the eddy viscosity model and thus the turbulent stresses could be modelled. This mixing length model led to closed form solutions for pipe and channel turbulent flows that were remarkably successful

in collapsing the existing experimental data [63]. This early development was the cornerstone for nearly all turbulence modelling for the next twenty years. The mixing length model is now known as the algebraic, or zero equation model.

To develop a more realistic mathematical model of the turbulence stresses, Prandtl in 1945 proposed the one-equation model in which the eddy viscosity depends on the turbulence kinetic energy, which was obtained from a separate modelled transport equation. This was a precursor to the one-equation models of turbulence or the so-called $k-l$ models, wherein the turbulent length scale l is specified empirically and the turbulent kinetic energy k is obtained from a modelled transport equation.

The first complete turbulence models were introduced through the first two-equation model, known as the $k-\varepsilon$ model. Similarly to the one-equation models, the two-equation models solve for the turbulence kinetic energy, k, and in addition they solve another transport equation, which in the $k-\varepsilon$ model case is for the dissipation of the turbulence kinetic energy, ε. The two-equation models also used the concept of the eddy viscosity to determine the Reynolds stress tensor.

The next step in accuracy came with the modelling approach, known as second order or second moment closure approach. The primary conceptual advantage of a stress transport model is the natural manner in which nonlocal and history effects are incorporated. The complex nature of these models awaited the advent of adequate computer resources to be exploited fully. The four main categories of turbulence models were:

- Zero Equation Models
- One Equation Models
- Two Equation Models
- Second Order closure Models

Development of the afore-mentioned models gained importance with the increased computing capabilities.

In the early 1980's researchers started focusing on more accurate simulation techniques, like Large Eddy Simulations (LES) and Direct Numerical Simulations (DNS), which can represent the physics of turbulence accurately, as these are not based on the basic modelling or approximating techniques as those that were used by previous models. DNS models solve for the actual turbulent flow field.

As it is clear from the above 'glance' on the history of turbulence modelling, a number of models have been developed that can be used to approximate turbulence. Some have very specific applications, while others can be applied to a wider class of flows with a reasonable degree of confidence. In this chapter, the basic idea of the Reynolds Averaged Navier Stokes (RANS) models is introduced through the analysis of the conservation equations. The last section of this chapter is devoted to the main aspects together with a discussion on the RANS model used in this research work, known as the Spalart - Allmaras (SA) model.

3.2 Conservation Equations

3.2.1 Instantaneous quantities and their decomposition

An example of a plot of a turbulent instantaneous velocity field can be seen in figure 3.1.

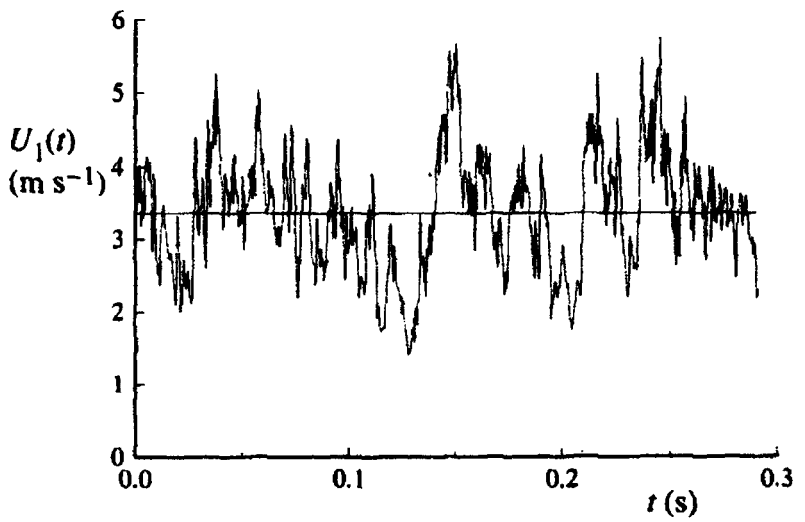

Figure 3.1: Time history of the axial velocity $U_l\,(t)$ on the centerline of a turbulent jet. Adapted from Tong and Warhaft [64]

This field may be generated by the readings of a probe put in a pipe, where the fluid flow is turbulent. The typical mathematical approach to study a turbulent instantaneous velocity field, u_i, is to decompose it in a mean velocity field, $\overline{u}_i$, and a fluctuating velocity field, u_i' , i.e.:

$$u_i = \overline{u}_i + u_i' \tag{3.1}$$

The decomposition of any instantaneous quantity field is fundamental in turbulence modelling techniques. The simple reason behind this is that it is not affordable, even with current computational power, to fully solve a turbulent flow, except for some few simple cases. Instead of solving equations for instantaneous quantities, in most of the cases it is more affordable to solve the equations for the time averaged quantities, like $\overline{u}_i$ in equation 3.1.

Similarly to the instantaneous velocity field, the instantaneous pressure and temperature field, respectively, can be decomposed as:

$$p = \overline{p} + p' \tag{3.2}$$

$$T = \overline{T} + T' \tag{3.3}$$

The time averaged (mean) quantities have the known linear properties:

$$\begin{aligned} \overline{x+y} &= \overline{x} + \overline{y} \\ \overline{\alpha x} &= \alpha \overline{x} \\ \overline{\overline{x}} &= \overline{x} \end{aligned} \tag{3.4}$$

where α is a constant.

3.2.2 Conservation of mass

The continuity equation for incompressible flow, using the Einstein summation convention, is the following:

$$\frac{\partial \rho}{\partial t} + \frac{\partial}{\partial x_j}(\rho u_j) = 0 \tag{3.5}$$

Decomposing the instantaneous velocity to its mean and fluctuating components and time averaging, equation 3.5 is written as:

$$\frac{\partial \rho}{\partial t} + \frac{\partial}{\partial x_j}\left(\rho \overline{u}_j + \rho \overline{u_j'}\right) = 0 \tag{3.6}$$

Since the mean of a fluctuation equals zero, equation 3.6 is simplified to:

$$\frac{\partial \rho}{\partial t} + \frac{\partial}{\partial x_j}(\rho \overline{u}_j) = 0 \tag{3.7}$$

Expanding its second term, equation 3.7 is written as:

$$\frac{\partial \rho}{\partial t} + \overline{u}_j \frac{\partial \rho}{\partial x_j} + \rho \frac{\partial \overline{u}_j}{\partial x_j} = 0 \tag{3.8}$$

Since the flow is incompressible, the fluid density is constant and the final simplified form of the continuity equation is:

$$\frac{\partial \overline{u}_j}{\partial x_j} = 0 \tag{3.9}$$

which is the time averaged continuity equation for incompressible flows.

3.2.3 Conservation of momentum

The momentum equations, also known as the Navier Stokes equations, for incompressible flows can be written as [24]:

$$\frac{\partial}{\partial t}\left(\rho u_i\right) + \frac{\partial}{\partial x_j}\left(\rho u_j u_i\right) = -\frac{\partial p}{\partial x_i} + \frac{\partial}{\partial x_j}\left[\mu\left(\frac{\partial u_i}{\partial x_j} + \frac{\partial u_j}{\partial x_i}\right)\right] - \rho g_i \tag{3.10}$$

Substituting the decomposed expression of the instantaneous velocity field from equation 3.1 into the Navier-Stokes equations and then applying a time average, the Reynolds Averaged Navier-Stokes (RANS) equations are obtained:

$$\begin{aligned} &\frac{\partial}{\partial t}\left[\rho\left(\overline{u}_i + \overline{u'}_i\right)\right] + \frac{\partial}{\partial x_j}\left[\rho\left(\overline{u}_i\overline{u}_j + \overline{u}_j\overline{u'_i} + \overline{u}_i\overline{u'_j} + \overline{u'_i u'_j}\right)\right] = \\ &-\frac{\partial p}{\partial x_i} + \frac{\partial}{\partial x_j}\left\{\mu\left[\frac{\partial\left(\overline{u}_i + \overline{u'_i}\right)}{\partial x_j} + \frac{\partial\left(\overline{u}_j + \overline{u'_j}\right)}{\partial x_i}\right]\right\} - \rho g_i \end{aligned} \tag{3.11}$$

Using the time averaging properties (equations 3.4), equation 3.11 is written:

$$\begin{aligned}&\frac{\partial}{\partial t}\left(\rho\overline{u}_i\right)+\frac{\partial}{\partial x_j}\left(\rho\overline{u}_i\overline{u}_j\right)+\frac{\partial}{\partial x_j}\left(\overline{\rho u_i' u_j'}\right)= \\ &-\frac{\partial p}{\partial x_i}+\frac{\partial}{\partial x_j}\left[\mu\left(\frac{\partial \overline{U}_i}{\partial x_j}+\frac{\partial \overline{U}_j}{\partial x_i}\right)\right]-\rho g_i\end{aligned} \tag{3.12}$$

Rearranging:

$$\begin{aligned}&\frac{\partial}{\partial t}\left(\rho\overline{u}_i\right)+\frac{\partial}{\partial x_j}\left(\rho\overline{u}_i\overline{u}_j\right)= \\ &-\frac{\partial p}{\partial x_i}+\frac{\partial}{\partial x_j}\left[\mu\left(\frac{\partial \overline{u}_i}{\partial x_j}+\frac{\partial \overline{u}_j}{\partial x_i}\right)-\rho\overline{u_i' u_j'}\right]-\rho g_i\end{aligned} \tag{3.13}$$

The above equations are known as the Reynolds Averaged Navier Stokes equations for incompressible flow. By comparing the Navier-Stokes equations 3.10 and the Reynolds averaged Navier-Stokes (RANS) equations 3.13, it can be seen that the difference between them is the term: $-\rho\left(\overline{u_i' u_j'}\right)$. This term is called the Reynolds stresses tensor. At this point, the essence of the so-called closure problem is revealed and it is the determination of the Reynolds stresses. Because of the existence of the Reynolds stresses and the nonlinearity of the equations, RANS equations cannot be solved in an analytical way. In order to close the RANS equations the Reynolds stresses must be expressed in some way and here is the point where turbulence modelling comes into picture. The following section refers to the turbulence model used in the current simulations, which lies in the family of RANS models.

3.3 The Spalart - Allmaras Model

The turbulence model used in the current simulations is the Spalart - Allmaras (SA) model [62]. It is a one-equation model, which solves for the turbulent eddy viscosity, ν_t. The modelled eddy viscosity is introduced to the RANS equations 3.13 through the eddy viscosity approach of the Reynolds stresses: $-\rho\overline{u_i'u_j'} = 2\nu_t S_{ij}$, where S_{ij} is the strain rate tensor. The transport equation for the eddy viscosity is:

$$\begin{aligned} &\frac{\partial \rho\tilde{\nu}}{\partial t} + \frac{\partial}{\partial x_i}\left(\rho u_i \tilde{\nu}\right) = \\ &c_{b1}\rho\tilde{S}\tilde{\nu} - c_{w1}f_w\rho\left(\frac{\tilde{\nu}}{d}\right)^2 + \frac{\rho}{\sigma}\left[\frac{\partial}{\partial x_i}\left(\left(\nu+\tilde{\nu}\right)\frac{\partial\tilde{\nu}}{\partial x_i}\right) + c_{b2}\left(\frac{\partial\tilde{\nu}}{\partial x_i}\right)^2\right] \end{aligned} \tag{3.14}$$

The quantity $\tilde{\nu}$ is defined so that it equals $\kappa y u_\tau$ all the way to the wall. In this way, $\tilde{\nu}$ is equal to ν_t except in the viscous wall region, for which:

$$\nu_t = \frac{\mu_t}{\rho} = \tilde{\nu} f_{v1}, \; f_{v1} = \frac{\chi^3}{\chi^3 + c_{v1}^3}, \; \chi \equiv \tilde{\nu}/\nu \tag{3.15}$$

The quantity ν is the kinematic viscosity, μ_t is the turbulent dynamic viscosity and f_{v1} is a function, borrowed from Mellor and Herring [32]. Also, d is the distance from the wall, σ is a turbulent Prandtl number and c_{b1}, c_{b2} and c_{w1} are constants of the model (see table 3.1). The subscripts b and w stand for basic and wall respectively and f_w is a non dimensional function (see table 3.1). In the R.H.S of equation 3.14 the first term represents the production of the turbulent eddy viscosity. In this term $\tilde{S}$ is a modified velocity gradient norm (see table 3.1). The second term in the R.H.S

of equation 3.14 represents the destruction of the turbulent eddy viscosity and the third term represents the diffusion of it.

The idea for the SA model was initiated from Baldwin-Barth's model [2]. The fundamental difference of the SA model compared to the Baldwin-Barth's model is based on the idea that generating a one-equation model as a simplified version of the $k - \varepsilon$ model is not optimal [62]. What Spalart and Allmaras did was to generate 'from scratch' all the terms in the transport equation 3.14 for the turbulent eddy viscosity. So, what they basically did in their original paper was to present four nested versions of the model from the simplest, applicable to free shear flows to the most complete, applicable to viscous flows past solid bodies and with laminar regions. In this way, as each additional effect was considered, new terms were added and calibrated resulting in the final form of the transport equation 3.14. In this procedure, the various constants and functions of equation 3.14 were determined and they are summarized in table 3.1.

The choice of $\tilde{\nu}$ as the transported quantity is beneficial for numerical solutions. The reason for this is that $\tilde{\nu}$ behaves linearly near the wall. In this way, the model does not require a finer grid than an algebraic model would. Early one-equation models use length scales related to the boundary layer thickness, which make them non-local, i.e. the equation at one point depends on the solution at other points. In contrast, the SA model is local, which makes it compatible with grids of any structure and Navier-Stokes solvers in two or three dimensions. The wall and freestream boundary

Table 3.1: SA constants and functions

Symbol	Explanation
$c_{b1} = 0.1355$	Production term constant
$c_{b2} = 0.622$	Diffusion term constant
$\sigma = \frac{2}{3}$	Turbulent Prandtl number
$c_{w1} = 3.2391$	Destruction term constant
$c_{w2} = 0.3$	Constant in g-function
$c_{w3} = 2$	Constant in f_w-function
$\kappa = 0.41$	Von Karman constant
$c_{v1} = 7.1$	Constant in f_v1-function
$f_w = g\left[\frac{1+c_{w3}^6}{g^6+c_{w3}^6}\right]^{\frac{1}{6}}$	Function in the destruction term
$g = r + c_{w2}\left(r^6 - r\right)$	Function in f_w-function
$r = \frac{\tilde{\nu}}{\tilde{S}\kappa^2 d^2}$	Function in g-function
$f_{v2} = 1 - \frac{\chi}{1+\chi f_{v1}}$	Function in $\tilde{S}$
$\tilde{S} = S + \frac{\tilde{\nu}}{\kappa^2 d^2} f_{v2}$	Modified velocity gradient norm
S	Velocity gradient norm

conditions are trivial. This fact adds an advantage of the SA model compared to some two-equation models, which are highly sensitive to freestream values, such as the value of the time scale.

Although the model has some limitations, such as the lack of accounting for the decay of the eddy viscosity in isotropic turbulence and the implication that in homogeneous turbulence the eddy viscosity is unaffected by irrotational mean straining [41], it was not meant to be a universal model. It was specifically calibrated and provided good results for aerodynamic flows [20]. It was used successfully in vortex shedding flows and in general in flows where there is formation of vortex structures, both for separated and unseparated boundary layer flows and with various degrees of complexity [40], [7].

A higher order of accuracy model would probably give more accurate results, but, as the intention of Spalart and Allmaras was, their model was developed on the basis of removing the incompleteness of algebraic and one-equation models (based on k) and on the other hand to acquire a computationally simpler model than the two-equation models. Although the SA model was calibrated for aerodynamic flows it was also used successfully for internal turbulent flows, such as channels with corners ([18], [39], [56]).

The above reasons provide justification for using this model in the present study, since it has been experimentally observed that a street of counter rotating pairs of vortices in an alternating pattern is formed at the edges of the gap region,

which conects two rectangular channels (figure 4.1). This is the geometry used in the present study, and is discussed in the following chapter.

Chapter 4

Analysis of Results

4.1 Overview

This chapter presents the simulation results and analysis of the turbulent flow field structure in a compound rectangular channel geometry. The numerical results are compared with the experimental dataset of Meyer and Rehme [34]. The importance of grid resolution and the numerical advection scheme is studied. Axial and span-wise velocity distributions, instantaneous velocity plots, turbulence quantities, correlation and power spectral density functions were generated and compared with the experimental data. The last two subsections of this chapter present the study on the effect of the channel's length and the comparison of the results obtained using the Spalart-Allmaras (SA) turbulence model and the $k - \varepsilon$ model.

4.2 Experimental Dataset

4.2.1 Description of the experiments

Figure 4.1 shows the cross-section, the coordinate system and the associated velocities for the twin rectangular subchannel geometry.

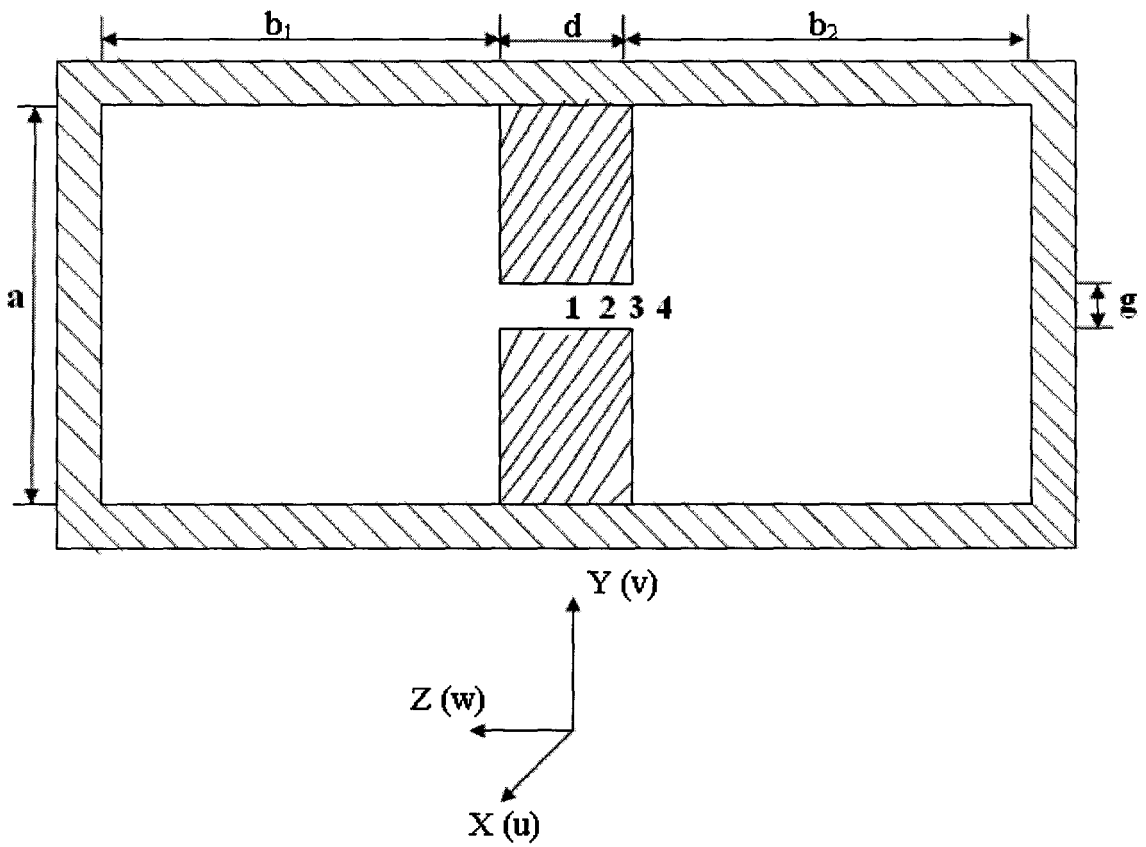

Figure 4.1: Cross-section of the flow channel [34]

The bulk flow is in the x-direction (i.e. from the page to the reader in figure 4.1). The stream-wise (axial) direction is denoted by x, the wall normal di-

rection is denoted by y and z is the span-wise direction. The dimensions of the cross-section (see figure 4.1) varied through the experiments, resulting in 18 different configurations. Nine of these configurations consisted of two almost identical rectangular channels, connected by gaps of different sizes. Seven geometries consisted of one rectangular channel (same dimensions for all seven cases) with a gap at its one side. In these cases the gap is referred to as slot and again the dimensions of it change through the studied flow configurations. The length of the test section was $L = 7,000$ mm. The dimensions of one of the experimental test cases for which numerical simulation results were generated are provided in table 4.1. This specific test case was selected to be studied because Meyer and Rehme provided detailed experimental results for this geometry in their paper.

Table 4.1: Cross-section dimensions (in mm) of the selected geometry

Dimension	Value
a	180.0
b_1	136.4
b_2	136.2
d (gap depth)	76.96
g (gap width)	10.0

The working fluid was air at atmospheric pressure and room temperature. The Reynolds number for most of the cases was $Re = 2.5 * 10^5$, based on the hydraulic diameter, D_h, and the bulk velocity of the flow, U_b. The hydraulic diameter

was defined for the channel neglecting the gap. To ensure fully developed flow conditions, the length-to-hydraulic diameter ratio of the measuring plane was at least $\frac{L}{D_h} = 40$. Meyer and Rehme [34] used Pitot tubes to measure the time mean values of the axial velocity and Preston tubes to measure the time mean values of the wall shear stresses. They also used hot wire anemometry to measure the turbulence shear stresses. Furthermore, power spectral densities of the fluctuating velocities in the vicinity of the gap were obtained. At the same positions, autocorrelation functions for the velocity fluctuations in the stream-wise and span-wise directions were also measured.

4.3 Simulation Details

4.3.1 Solution domain and mesh generation

The solution domain was based on case no.9 of the Meyer and Rehme experiments [34]. The dimensions of the cross-section of this geometry are given in table 4.1. A shorter length of $L = 730$ mm was used in the simulations with periodic boundary conditions. Periodic boundary conditions were used because the experimental length was too long to be numerically implemented with the available computational sources. The specific value of L was selected in order to capture approximately four vortex structures of alternate sequences in this length of the channel. This estimation was based on the wavelength of the structures reported by Meyer and Rehme [34].

The code uses finite volume discretization, with fully implicit time advance-

ment scheme. For the present computations, in all cases, the time discretization was carried out using the second-order backward Euler scheme. In four cases for all the equations (continuity, momentum and eddy viscosity), the advection scheme used by the code was the first order upwind scheme and in two cases, the advection scheme for the eddy viscosity was again the first order upwind, whereas for the continuity and momentum equations the advection scheme used was a second order accurate in space scheme. The details of the advection schemes used and in general the characteristics of all the cases are discussed in section 4.4.

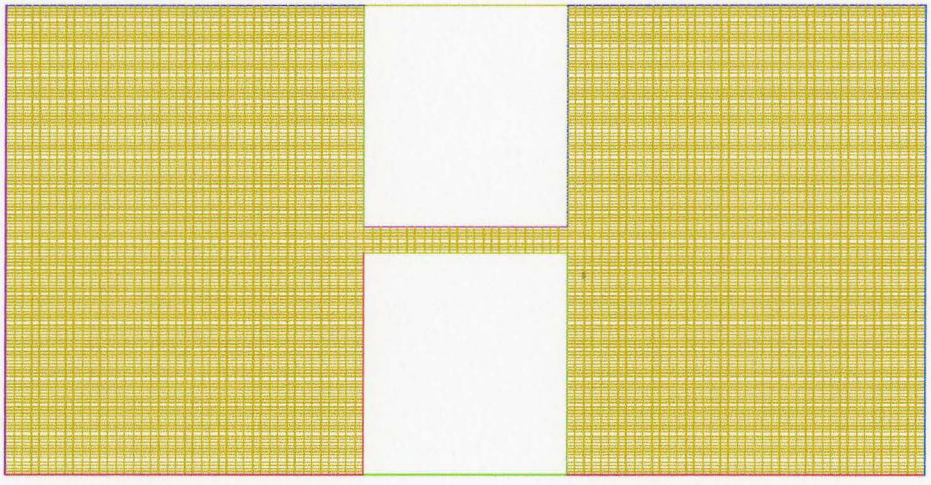

Figure 4.2: Reference mesh, M_1

Based on the literature review on the Spalart - Allmaras (SA) model (section 3.3), the restriction on the dimensionless distance from the wall, y_w^+, was:

$$y_w^+ \approx 1 \qquad or \qquad y_w^+ > 30 \tag{4.1}$$

An initial mesh (M_1) was generated, which had a total of 633,850 nodes. Uniform meshing law was applied in the respective directions. A cross-section of this mesh can be seen in figure 4.2.

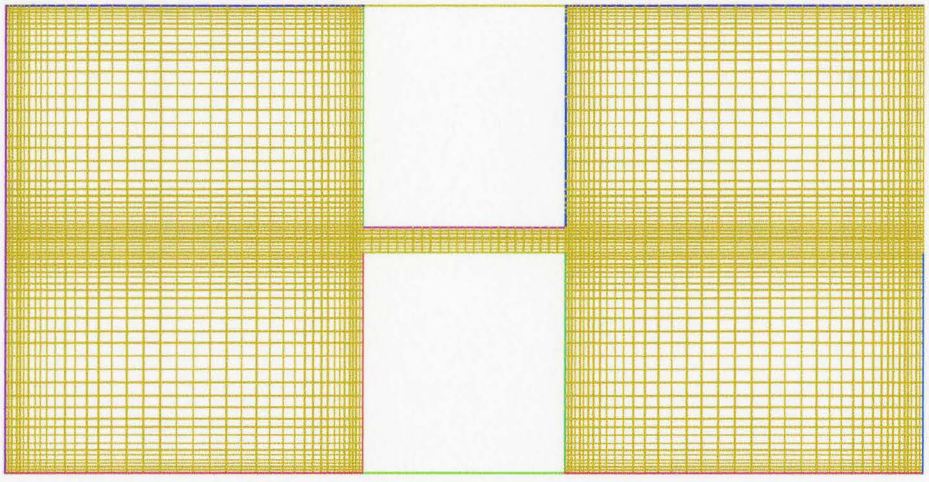

Figure 4.3: Mesh, M_5

In the stream-wise direction (x-direction) the number of nodes is 50 (X_{sub}). In the wall-normal direction (y-direction) there are 145 nodes (Y_{sub}), whereas the number of nodes at the gap is 9 (Y_{gap}). In the span-wise direction (z-direction) the total number of nodes for both the subchannels is 109 (Z_{tot}), whereas at the gap region there are 25 nodes (Z_{gap}). The number of nodes for the reference mesh, M_1, and for the rest of the grid structures is provided in table 4.2. Grids M_2, M_3 and M_4 were generated from grid M_1 by doubling the number of nodes in the z-direction, x-direction and y-direction, respectively. For grid M_5, shown in figure 4.3, the mesh is expanded in the z and y-directions, except for the gap, where the mesh is uniform

Table 4.2: Number of nodes for the grid structures used

Mesh	M_1	M_2	M_3	M_4	M_5
Total	633,850	1,268,600	1,267,700	1,276,300	278,350
X_{sub}	50	50	**100**	50	50
Y_{sub}	145	145	145	**290**	69
Z_{sub}	43	**86**	43	43	40
Y_{gap}	9	9	9	**18**	9
Z_{gap}	25	**50**	25	25	25

in both z and y-directions. For the x-direction, in all the cases, a uniform meshing law was applied.

4.3.2 Fluid properties

Table 4.3: Fluid properties

Property	Value	Units
Fluid	Air	
Temperature	25	$[^oC]$
Density	1.185	$\left[\frac{kg}{m^3}\right]$
Dynamic viscosity	$1.831 * 10^{-5}$	$[Pa.s]$

In the experiments conducted by Meyer and Rehme [34], the fluid used was air. The thermal-physical properties of air used for the simulations are provided in

table 4.3.

4.3.3 Boundary conditions and initial conditions

In the stream-wise direction, periodic boundary conditions were applied. For all other surfaces of the channel, no slip wall boundary conditions were applied. The mass flow rate, $\dot{m}$, was provided to drive the flow through the domain. This mass flow rate corresponds to a Reynolds number of $2.15 * 10^5$, based on the bulk velocity, U_b, and the hydraulic diameter, D_h, of the channel.

An initial profile for the axial velocity was required to start the simulation. This profile was obtained from an SST run. The time step is set to 10^{-4} sec. The selected time step was based on the frequency of 68 Hz of the flow pulsations observed in the experiments [34]. This ensured that the timestep was sufficiently small to capture the transient nature of the pulsations. As an implicit code, ANSYS CFX-11.0 does not require the Courant number to be small for stability. The statistics were started after 5,000 simulation time steps and then accumulated over another 5,000 time steps. The total time for the simulation was one second.

4.4 Results and Discussion

4.4.1 Summary of cases

In table 4.4 the cases presented in this report are summarized. In addition to these cases, two more simulations were carried out, and are discussed only in the last two subsections of this chapter. The computions were conducted in a two Quad core 2.4 GHz processor and 2x4 GB of RAM memory. The simulation time varied from eight days to approximately a month, depending on the case study.

Table 4.4: Summary of cases

Case	Used mesh	Advection scheme
C_1	M_1	$1^{st}\,(o)$ Upwind
C_2	M_2	$1^{st}\,(o)$ Upwind
C_3	M_3	$1^{st}\,(o)$ Upwind
C_4	M_4	$1^{st}\,(o)$ Upwind
C_5	M_1	$2^{nd}\,(o)$ Accurate
C_6	M_5	$2^{nd}\,(o)$ Accurate

As it can be clearly observed in the above summary of the cases, the main parameters that change among them is the mesh used and the advection scheme. The advection scheme refers to the numerical treatment of the advection term in the transport equations which solve for the main variables of the flow, namely, the eddy viscosity and the three velocity components. For example, the advection terms in

equations 3.13 and 3.14 are the second terms on the LHS of the equations, which are: $\frac{\partial}{\partial x_j}(\rho\overline{u}_i\overline{u}_j)$ and $\frac{\partial}{\partial x_i}(\rho u_i\tilde{\nu})$, respectively.

Advection is a phenomenon created by the fluid flow and represents the transport of a quantity by the fluid motion. For example, in the momentum equation, the advection term is $\frac{\partial}{\partial x_j}(\rho\overline{u}_i\overline{u}_j)$ and the transported quantity is the velocity $\overline{u}_i$, whereas in the case of the term: $\frac{\partial}{\partial x_i}(\rho u_i\tilde{\nu})$, the transported quantity is the eddy viscosity: $\tilde{\nu}$.

In the discretization process of a fluid flow problem, the idea of the first order upwind scheme can be described by considering the simplest possible case, which is a one-dimensional fluid flow. A typical grid-point cluster for a one-dimensional problem can be seen in figure 4.4. In figure 4.4, the control volume's vertical edges

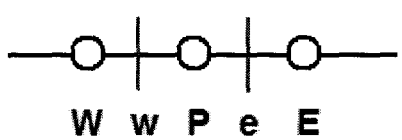

Figure 4.4: Grid-point cluster for one-dimensional problem

define the two integration points, symbolized with w, for west and e, for east. The control volume node is point P. At its west and east sides lie point W and point E, respectively. Let ϕ be the transported quantity. What the first order upwind scheme assumes is that the value of ϕ in the advection term at an integration point is the value of ϕ at the upwind node. For example, if the flow in figure 4.4 is from the left to the right, the value of ϕ_e will be the value of ϕ at node w, ϕ_w.

Although for high velocity flows parallel to the grid, the first order upwind

assumption is reasonable, in most turbulent fluid flows or very low-velocity flows, schemes of higher accuracy are necessary. In the case of the second order accurate in space scheme, ϕ_e is calculated by the following formula:

$$\phi_e = \phi_w + \beta \frac{\partial \phi}{\partial x} \Delta x \tag{4.2}$$

In equation 4.2, β is called the blending factor and in this case its value is unity. The spatial gradient $\frac{\partial \phi}{\partial x}$ is calculated at the adjacent nodes of the nodal point e and Δx is the distance between nodes w and e.

4.4.2 Mesh sensitivity

To assess grid independence for the first order upwind runs, grids M_1, M_2, M_3 and M_4 had been used. In the case of the runs for which the second order accurate scheme was used the tested grids were M_1 and M_5.

In figures 4.5, 4.6 there is a comparison of the mean axial velocity profiles at the symmetric horizontal line in the cross-section of the tested geometry (see figure 4.1). Figure 4.5 refers to the set of the first order upwind runs and figure 4.6 refers to the set of the second order accurate runs. As it can be seen in these two figures, the differences between the compared velocity profiles for the grids used are negligible. Specifically, the maximum difference between the plots for both figures 4.5 and 4.6 was not more than 0.9%.

Note that comparison of figure 4.5 to figure 4.6 shows that the second order

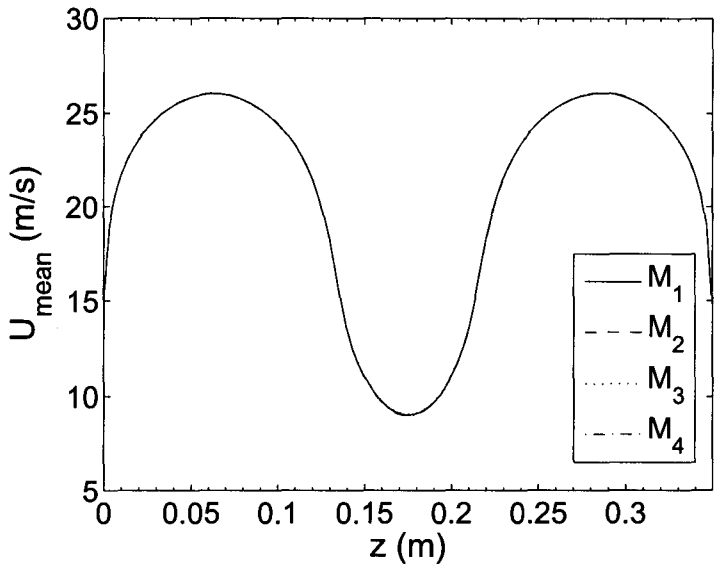

Figure 4.5: Mean axial velocity profiles for the first order upwind cases

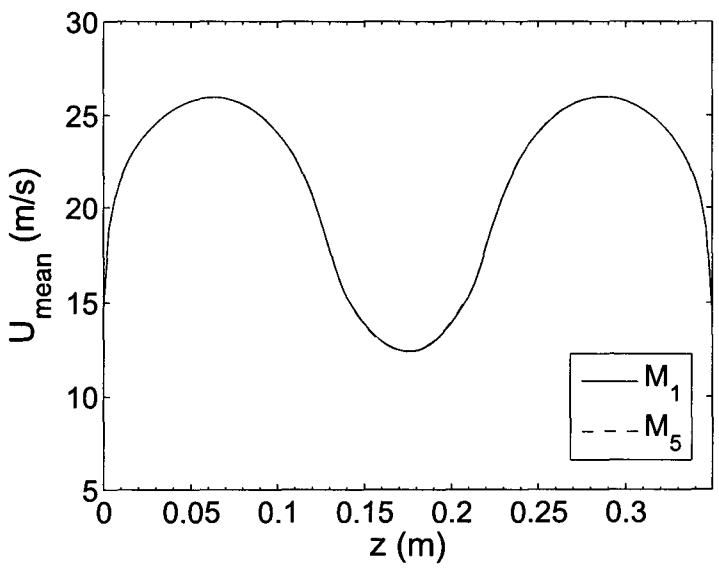

Figure 4.6: Mean axial velocity profiles for the second order accurate in space cases

accurate scheme predicts higher gap velocities than the first order upwind scheme. Differences resulting from a change in the advection schemes are presented in the following subsections. The following results are presented and discussed for case C_1 with first order upwind accuracy and case C_5 for second order accuracy in space.

4.4.3 Axial velocity distribution

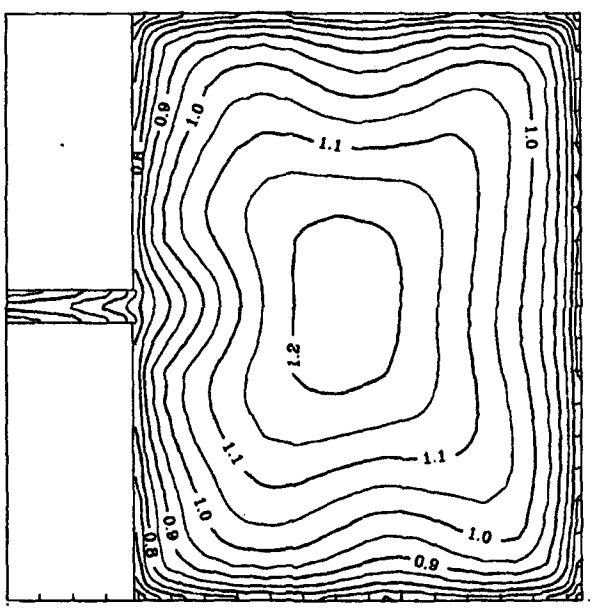

Figure 4.7: Contours of the normalized axial velocity U/U_b. Adapted from Meyer and Rehme [34]

The normalized time averaged axial velocity contour from the experiments [34] is shown in figure 4.7. In this figure only the right channel together with the half gap are illustrated. The contour plots from the numerical simulations for cases C_1 and C_5 are shown in figures 4.8 and 4.9, respectively.

In these figures, both the two channels together with the gap are illustrated.

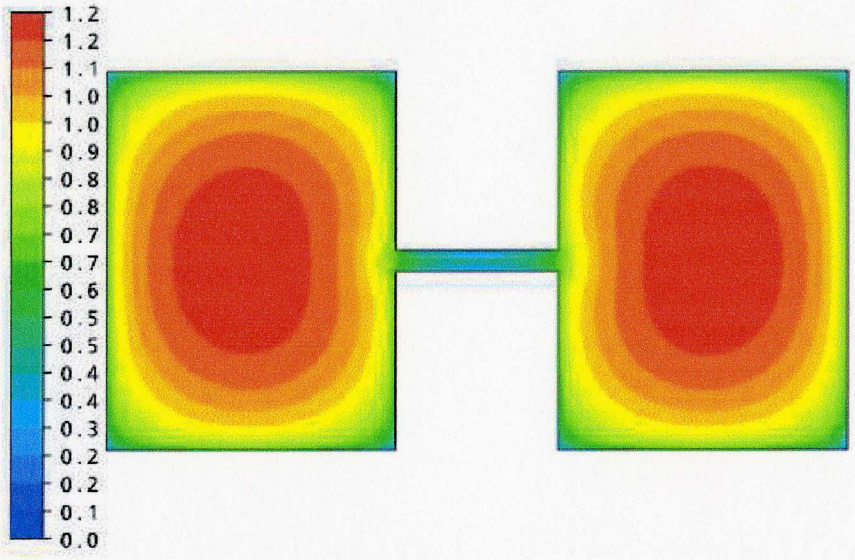

Figure 4.8: Normalized axial velocity contour plot for case C_1

The bulk velocity, $U_b = 21.5$ m/s, was used for the normalization of the axial velocity. In both cases C_1 and C_5, similar to the experiments, there was a clear symmetry with respect to the axis of symmetry through the gap. The normalized axial velocity at the cores of the two subchannels matched exactly its experimental value. The trend of the values at the contour lines from the centres to the corners of the subchannels for both cases, C_1 and C_5, matches the respective experimental trend. The contour plots show the typical bulging at the corners of the two connected channels, which is attributed to the formation of secondary flows. Right at the gap corners there was a bulging of the contour from the gap edges towards the two subchannels. This phenomenon must be attributed to the cross-flow at the gap. In case C_5 (figure 4.9), the bulging at the corners of the gap is more pronounced compared to

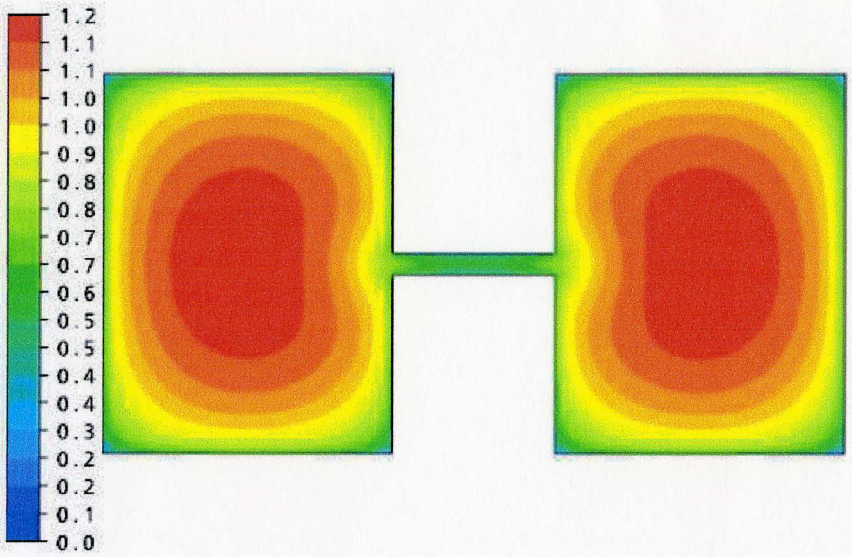

Figure 4.9: Normalized axial velocity contour plot for case C_5

case C_1 (figure 4.8). This pronounced bulging of the contour lines is closer to what the experiments showed, as depicted in figure 4.7.

In summary, the same qualitative observations for the mean axial velocity were made as reported in the experiments [34]. Furthermore, the velocity magnitudes are also very close to the experimental normalized velocity values.

4.4.4 Instantaneous span-wise velocity distribution

The instantaneous span-wise velocity contours at the (x, z) symmetry plane through the gap (i.e. at: $y = \frac{a}{2}$, see figure 4.1) for case C_1 and C_5 are shown in figures 4.11 and 4.12, respectively.

Figure 4.10 shows the plane at which the contour plots in figures 4.11 and

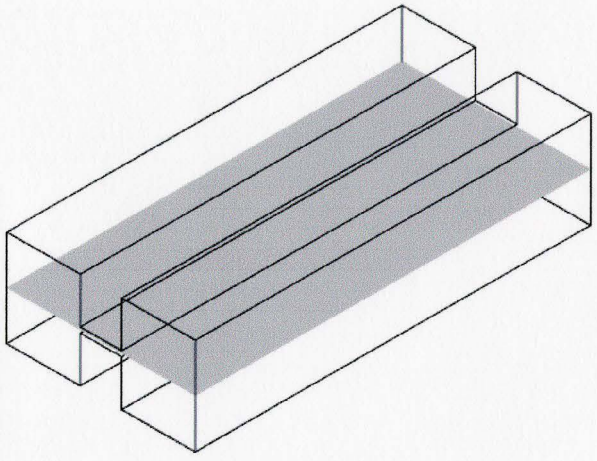

Figure 4.10: Symmetry plane at half of the height of the channel

4.12 have been generated. Figures 4.11 and 4.12 show a snapshot of the span-wise velocities at an instant in time. The gap region is demarcated from the subchannels by two thick black lines.

In case C_1, figure 4.11 clearly shows an alternate pattern of large-scale flow structures. The range of the predicted values of the span-wise velocity is symmetric. The instantaneous span-wise velocity plots, obtained from the experimental measurements, have also shown a similar symmetry in the range of the values. In addition, the magnitude of these velocity values is very close to the reported experimental values.

In contrast, the predictions for case C_5 (seen in figure 4.12) are not as structured. These contour plots reveal the fundamental difference between the two advection schemes used. The clear organized pattern of the contour plot in case C_1 is basically the result of numerical diffusion. Wherever the solver sees a steep spatial

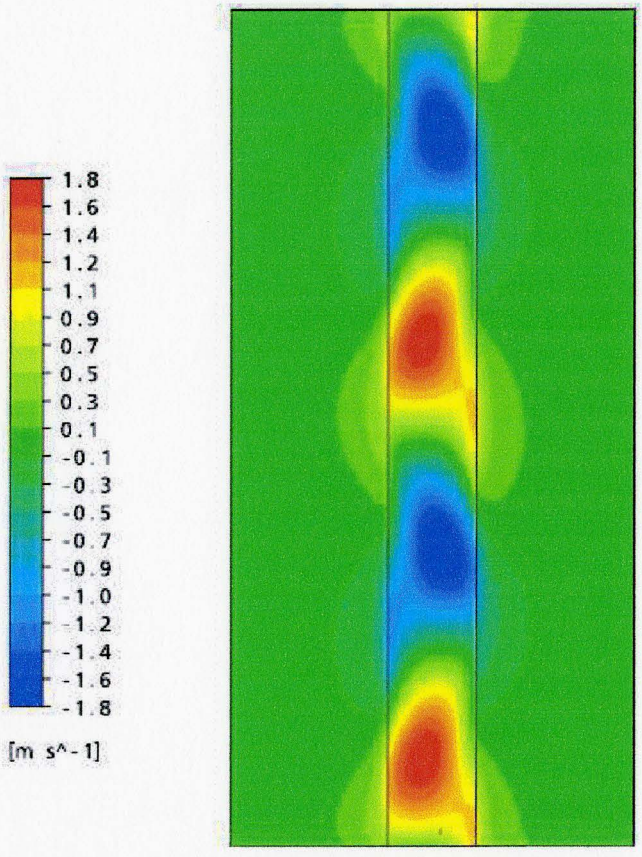

Figure 4.11: Instantaneous span-wise velocity contour for case C_1

gradient of a transported quantity, ϕ (in the case discussed: $\phi = w$), it tends to smear out this steep gradient. In this process, some information of the field simulated was missed. In contrast, in case C_5 (figure 4.12) because of the higher accuracy in space of the advection scheme used, the steep spatial gradients did not smear out with space, resulting in a more realistic picture of the field simulated.

In figures 4.13 and 4.14, the instantaneous velocity vector plots for both cases

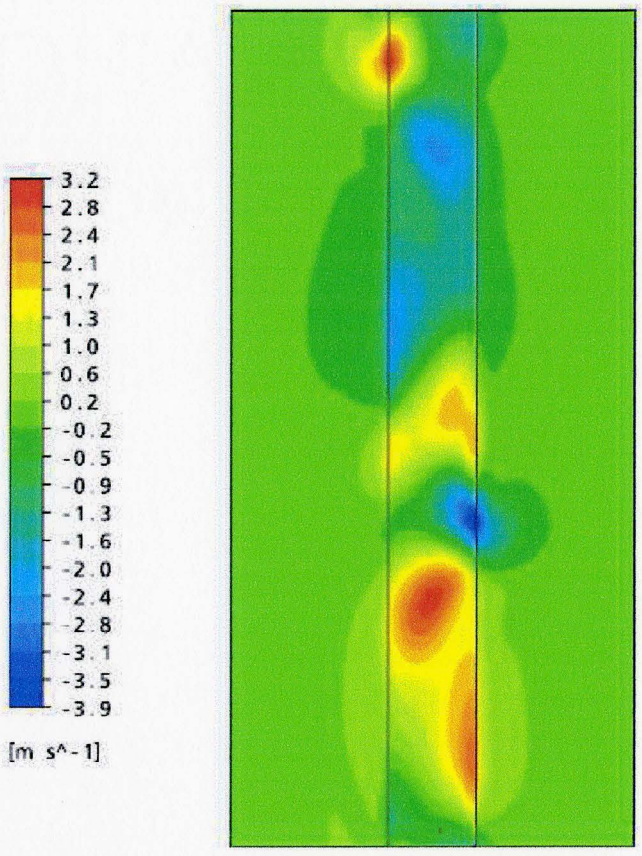

Figure 4.12: Instantaneous span-wise velocity contour for case C_5

C_1 and C_5 at the symmetry plane through the gap (figure 4.10) are shown. Based on the contour plots in figures 4.11 and 4.12, this wiggly pattern of the velocities in figures 4.13 and 4.14 was expected.

Figures 4.11, 4.12, 4.13 and 4.14 show that the fluid is being pushed in the span-wise direction in an alternate sequence through the gap. The high velocity gradients at the edges of the gap, where two shear layers meet, are responsible for

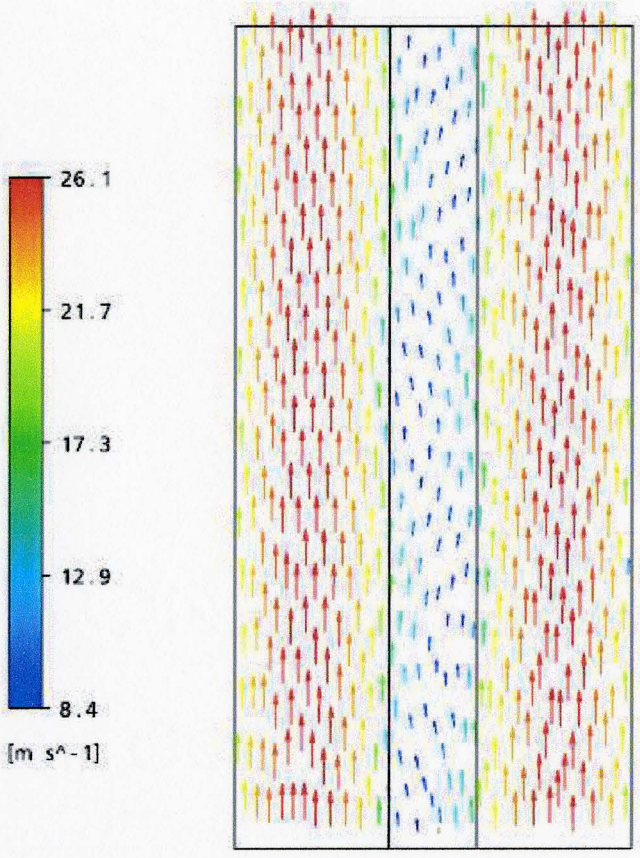

Figure 4.13: Velocity vector plot for case C_1

the formation of the flow pulsations. As mentioned in subsection 2.3.3 the results of Chang and Tavoularis [10] using the RNG $k-\varepsilon$ model in a rectangular channel containing a single rod, predicted flow pulsations at the region between the rod and the bottom surface of the channel, which washed out with time. In contrast, figures 4.11, 4.12 show that the flow pulsations do not wash out with time.

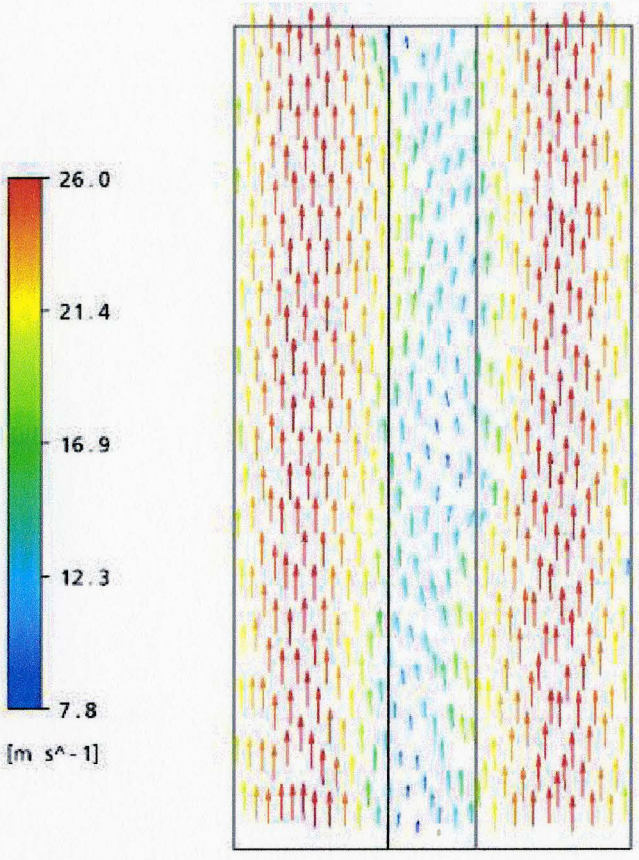

Figure 4.14: Velocity vector plot for case C_5

4.4.5 Velocity time traces

In the following figures the time variation of the span-wise velocity at the gap centre and at the gap edge and the axial velocity at the gap edge are presented. The symbols used (see figure 4.1) are w_1 and w_3 for the span-wise velocities at the gap centre and at the gap edge, respectively and u_3 for the axial velocity at the gap edge.

Experimental measurements of the instantaneous velocities are shown in

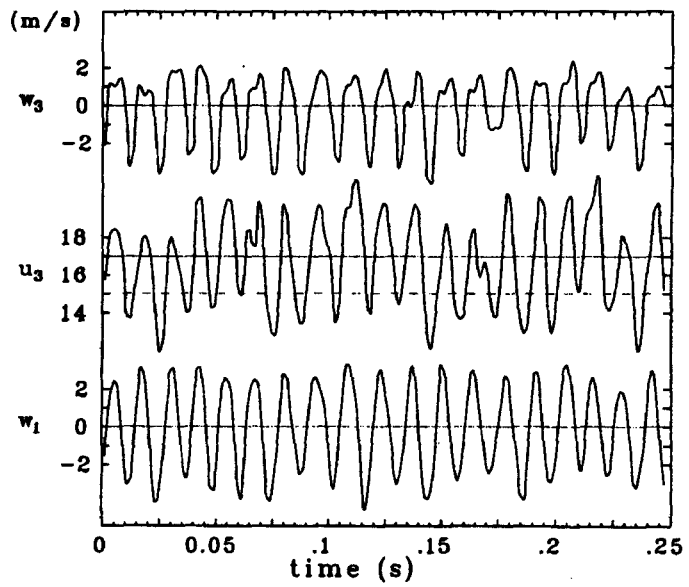

Figure 4.15: Time traces of the axial (u) and the span-wise (w) velocity. Adapted from Meyer and Rehme [34]

figure 4.15. It is clear that the instantaneous span-wise velocity time traces show a large scale quasi-periodic structure. The time trace of velocity w_1 (gap centre) shows a symmetric pattern, while the time trace of velocity w_3 (gap edge) has a strong negative skewness. In the plots for w_3 and u_3 there is an indication for the second peak to appear at the main frequency. Frequency analysis is discussed in subsections 4.4.7 and 4.4.8.

For case C_1 (figure 4.16), clear symmetry and periodicity can be observed in the results. The magnitudes of the velocities in all cases are similar to the experimental velocities. The main difference of the first order upwind cases, represented by case C_1, compared to the experiments is that the measurements showed a quasi-periodicity (figure 4.15). Also, the period of the velocity time traces for case C_1 is higher than

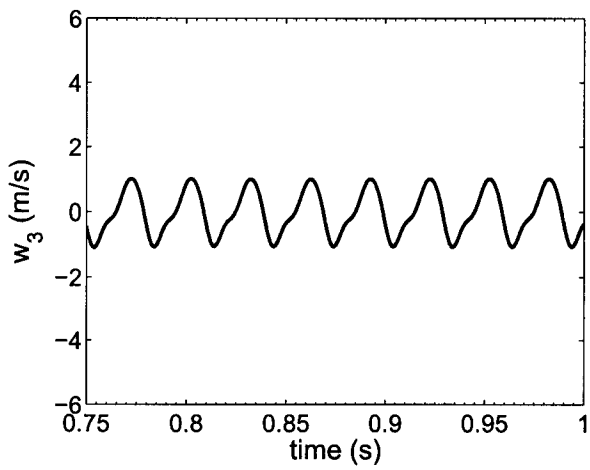

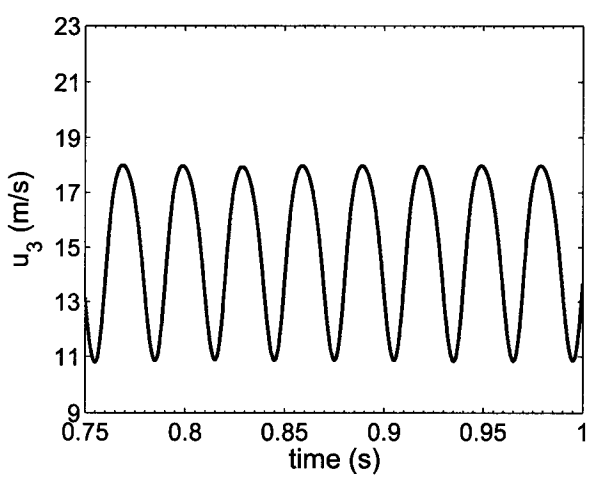

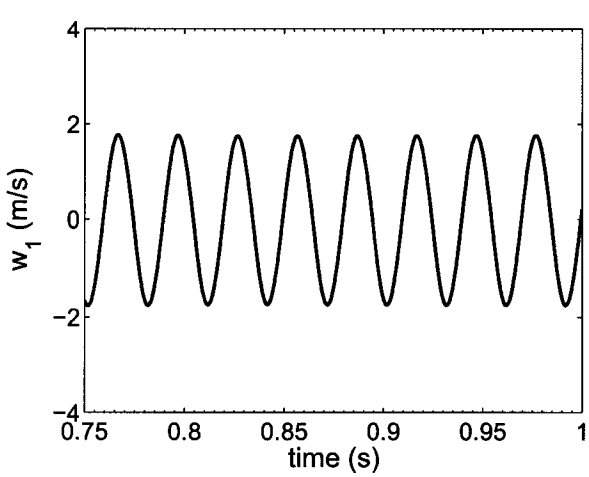

Figure 4.16: Time traces of the axial (u) and the span-wise (w) velocity for case C_1

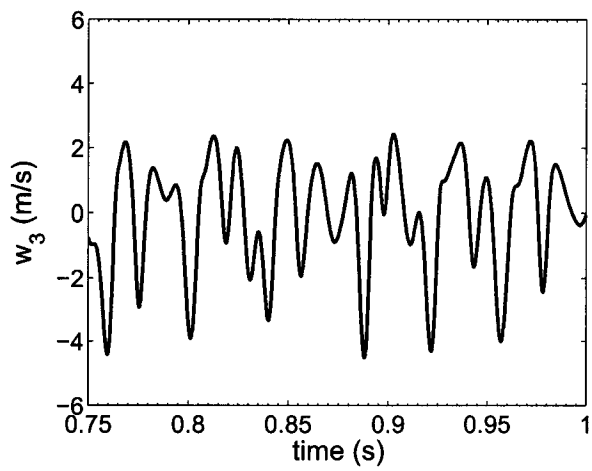

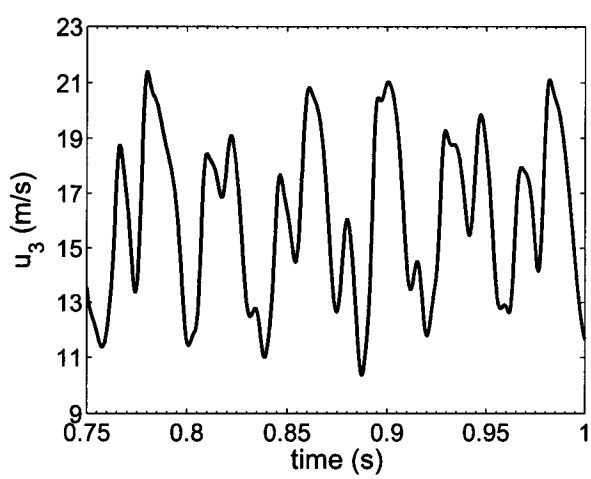

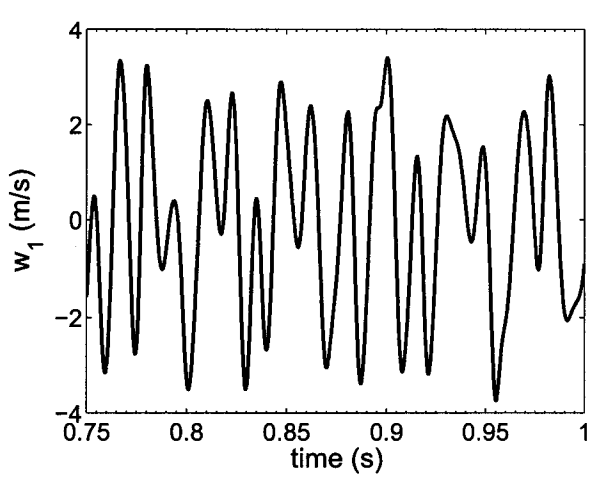

Figure 4.17: Time traces of the axial (u) and the span-wise (w) velocity for case C_5

the period of the respective experimental instantaneous velocity plots. The second order accurate cases, represented by C_5 (figure 4.17), showed a significantly different behaviour in the instantaneous span-wise and stream-wise velocity plots, compared to the first order upwind cases. As shown in figures 4.16 and 4.17, the calculated velocity time traces in case C_5 do not have the symmetry and periodicity that was observed in case C_1. There are not clear periodic peaks in the plots and the magnitudes of velocity are higher compared to case C_1.

However, the plot of velocity w_1 (gap centre) in figure 4.17 for case C_5 shows a symmetric behaviour, as it was also observed in the respective experimental measurements (figure 4.15). Moreover, the clear negative skewness in the instantaneous span-wise velocity time trace at the gap edge (w_3) that was reported in the experimental measurements, was also observed in the results of the second order accurate runs, as can be seen in the velocity w_3 plot for case C_5 in figure 4.17. Comparing figures 4.15 and 4.17, it can be observed that the variation of the instantaneous velocity fields at the gap centre and at the gap edge in case C_5 resemble the respective experimental velocity fields. This can be considered as an indication that case C_5 roughly captures the frequencies of the actual velocity field. As already mentioned, power spectral densities are discussed in section 4.4.8.

The effect of numerical diffusion can also be observed between the time traces for cases C_1 (figure 4.16) and C_5 (figure 4.17), in analogy with the span-wise velocity contours for these two cases (figures 4.11 and 4.12). More precisely, the clear sym-

metric and periodic pattern of the velocity time traces in case C_1 is a result of the smearing of the steep spatial gradients of the velocities. Since this smearing does not happen when using the second order accurate advection scheme, like in case C_5, the steep spatial gradients of the velocity fields affect the resulting instantaneous velocity plots.

4.4.6 Turbulence quantities

In this subsection a discussion on the measured and the computed turbulence quantities is carried out. Since the results of the simulations give only the modelled parts of these quantities the discussion is limited to qualitative comparison between the experimental measurements and the numerical predictions.

Meyer and Rehme [34] provided contour plots at (x, y) planes, normal to the stream-wise direction (see figure 4.1), of the normalized axial (u'), transverse (v') and span-wise (w') intensities (r.m.s velocities) for the case studied. These contours can be seen in figures 4.18, 4.19 and 4.20.

The intensities are normalized by the average friction velocity, $u_\tau = 0.924$ m/s, obtained from the experiments. In the subchannels (away from the gap region), the contours were similar to what would be seen for a simple channel flow. Specifically, the contours show a fairly good symmetry with respect to the span-wise symmetry line through the gap and the contour lines bulge toward the corners due to secondary flows. However, close to the gap, the behaviour of the turbulence intensities was

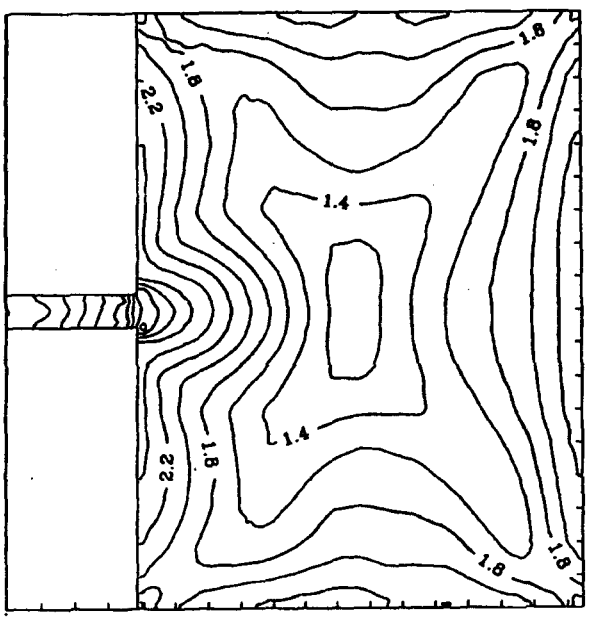

Figure 4.18: Contours of the normalized axial intensity, $\frac{u'}{u_\tau}$. Adapted from Meyer and Rehme [34]

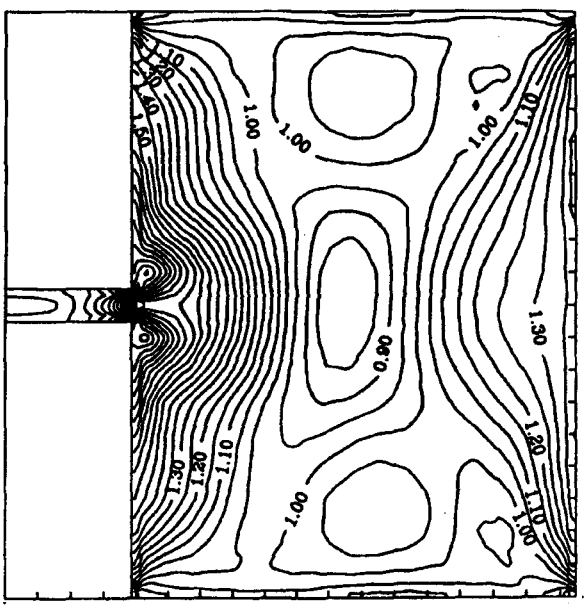

Figure 4.19: Contours of the normalized transverse intensity, $\frac{v'}{u_\tau}$. Adapted from Meyer and Rehme [34]

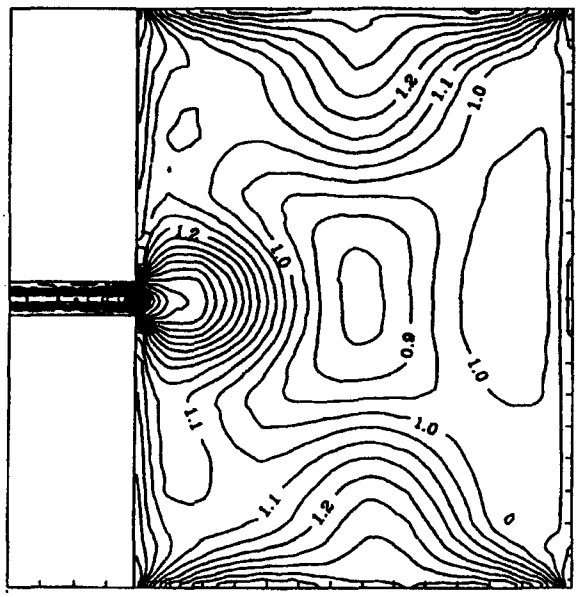

Figure 4.20: Contours of the normalized span-wise intensity, $\frac{w'}{u_\tau}$. Adapted from Meyer and Rehme [34]

completely different from the case of simple rectangular channels. The contours of the axial, u', and transverse, v', intensities show two peaks at each side of the gap. In the case of the span-wise intensity, w', only one peak was observed at each side of the gap. Furthermore, this intensity was very high along the whole depth of the gap.

The combination of these characteristics, as expected, was displayed in the turbulence kinetic energy, k, contours, where:

$$k = \frac{1}{2} * \left(\overline{u'^2} + \overline{v'^2} + \overline{w'^2}\right) \tag{4.3}$$

In figure 4.21, the normalized turbulence kinetic energy contours as reported in the experiments can be observed. The turbulence kinetic energy, k, was normalized by

the square of the average friction velocity, u_τ. As already implied, the symmetry of the contours with respect to the symmetry line through the gap was good since the symmetry of the three intensities was good. The contour lines bulge towards the corners of the channel, which means relatively low energy in the corners. The peak value of k at the corners of the gap was as high as 9.2. This value of k is more than twice the highest values at the other walls without the gap.

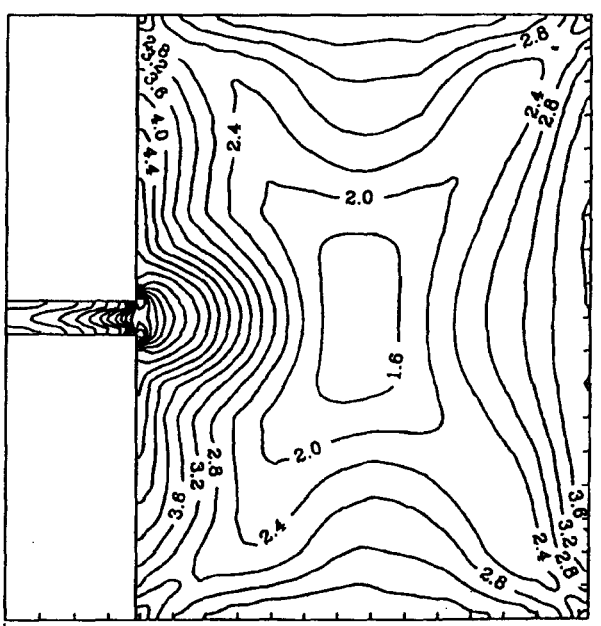

Figure 4.21: Contours of the normalized turbulence kinetic energy, $\frac{k}{u_\tau^2}$. Adapted from Meyer and Rehme [34]

As already discussed (section 3.3), the SA model is a RANS based model that calculates the turbulent viscosity from a one-equation transport model for ν_t. As such, the turbulence kinetic energy is not solved for directly. Since the momentum equations are solved to obtain unsteady solutions, the variance of the calculated

velocity fluctuations can be calculated from the transient solution.

For example, let: $u(x^*, y^*, z^*, t)$ be the predicted u velocity at location (x^*, y^*, z^*). This velocity is known at N discrete times contained in the time interval: $t_0 < t \leqslant t_0 + N\Delta t$. The number of samples, N, must be large enough to ensure statistical significance and the simulations must be statistically stationary. The mean value, $\overline{u}$, and the variance, $\tilde{u}^2$, are then calculated as:

$$\begin{aligned} \overline{u}(x^*, y^*, z^*, t) &= \frac{1}{N} \sum_{i=1}^{N} u(x^*, y^*, z^*, t_i) \\ \tilde{u}^2 &= E\left[(u - \overline{u})^2\right] = \frac{1}{N} \sum_{i=1}^{N} \left[(u - \overline{u})^2\right] \end{aligned} \tag{4.4}$$

where: $t_i = t_0 + i\Delta t$. The 'tilde' symbol indicates that the variance calculated is based on the resolved flow and does not include the turbulence kinetic energy which is implied in the turbulent viscosity. Similarly, velocity variances in the y and z directions can also be calculated. A kinetic energy associated with these fluctuations can be calculated as:

$$\tilde{k} = \frac{1}{2} * \left[\tilde{u}^2(x^*, y^*, z^*) + \tilde{v}^2(x^*, y^*, z^*) + \tilde{w}^2(x^*, y^*, z^*)\right] \tag{4.5}$$

Figures 4.22 and 4.24 show the calculated kinetic energy, $\tilde{k}$, at a cross-section for cases C_5 and C_1, respectively. The instantaneous turbulent viscosity is shown in figure 4.23 for case C_5 and in figure 4.25 for case C_1. The average friction velocity from the numerical results was underpredicted compared to the experiments.

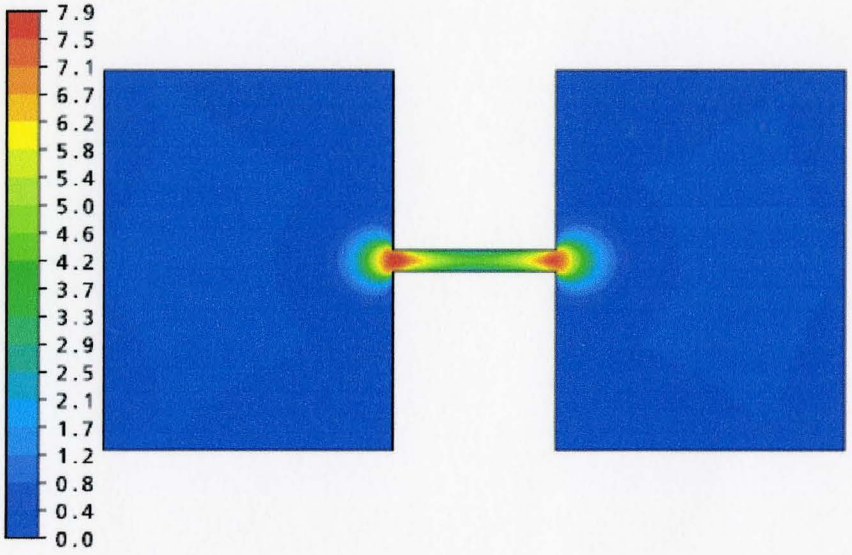

Figure 4.22: Contours of $\frac{\tilde{k}}{u_\tau^2}$ for case C_5

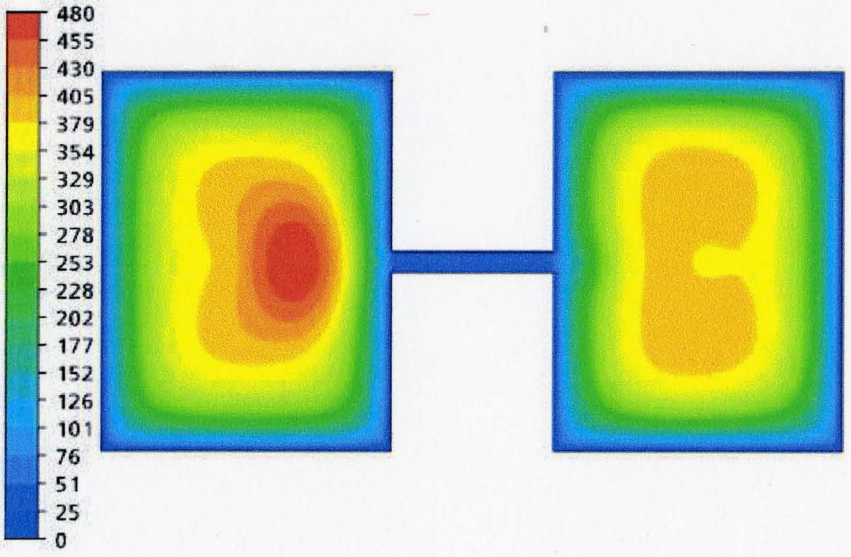

Figure 4.23: Normalized instantaneous eddy viscosity for case C_5

In order to isolate the contribution of $\tilde{k}$ in its normalized expression, $\frac{\tilde{k}}{u_\tau^2}$, and qualitatively compare it with the turbulence kinetic energy, k, from the experiments (equation 4.3), the experimental average friction velocity, $u_\tau = 0.924$ m/s, was used for the normalization of $\tilde{k}$. Furthermore, in figures 4.25 and 4.23, the turbulence eddy viscosity is normalized by the dynamic viscosity of air (table 4.3).

As it can be observed in figures 4.22 and 4.24, $\tilde{k}$ is zero at the regions away from the gap. Based on the discussion on equation 4.5, the fact that $\tilde{k}$ is zero in these regions, implies that the flow was predicted to be steady in the areas away from the gap. In contrast, the eddy viscosity had its highest values at the cores of the two subchannels, as seen in figures 4.23 and 4.25 for cases C_5 and C_1, respectively. This discussion suggests that an indication of the turbulence kinetic energy level should be considered from the combination of $\tilde{k}$ for the areas in the vicinity of the gap and of the eddy viscosity for the areas away from the gap.

As it is seen in figures 4.24 and 4.22, both the first order upwind and the second order accurate cases capture two peaks of $\tilde{k}$ at the corners of the gap, as it was reported for the turbulence kinetic energy, k, in the experiments (figure 4.21). For case C_1 the peak value of $\frac{\tilde{k}}{u_\tau}$ was 4.6, whereas for case C_5 it was 7.9 and in the experiments the peak value of the normalized turbulence kinetic energy was 9.2 (figure 4.21). Comparing figure 4.24 to figure 4.22 it is seen that at the vicinity of the gap, case C_5 predicts higher values of k in all three directions.

Figures 4.23 and 4.25, show that the instantaneous eddy viscosity at the walls

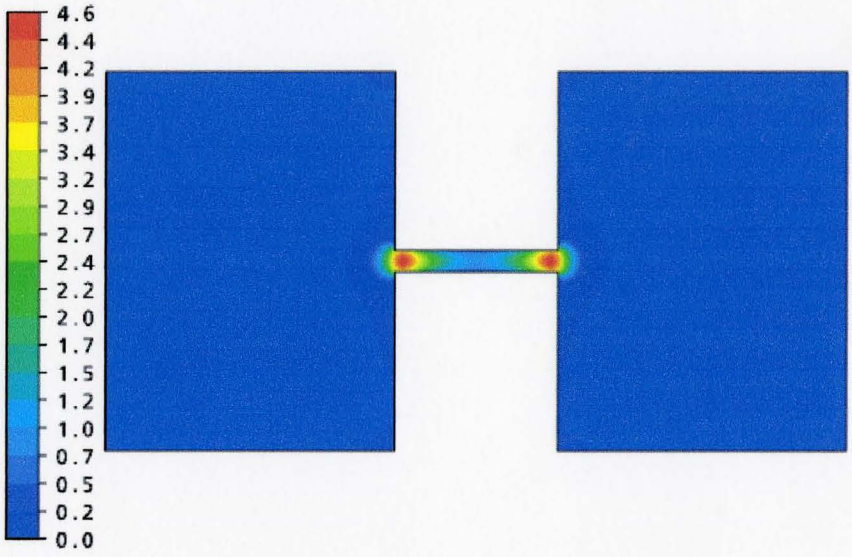

Figure 4.24: Contours of $\frac{\tilde{k}}{u_\tau^2}$ for case C_1

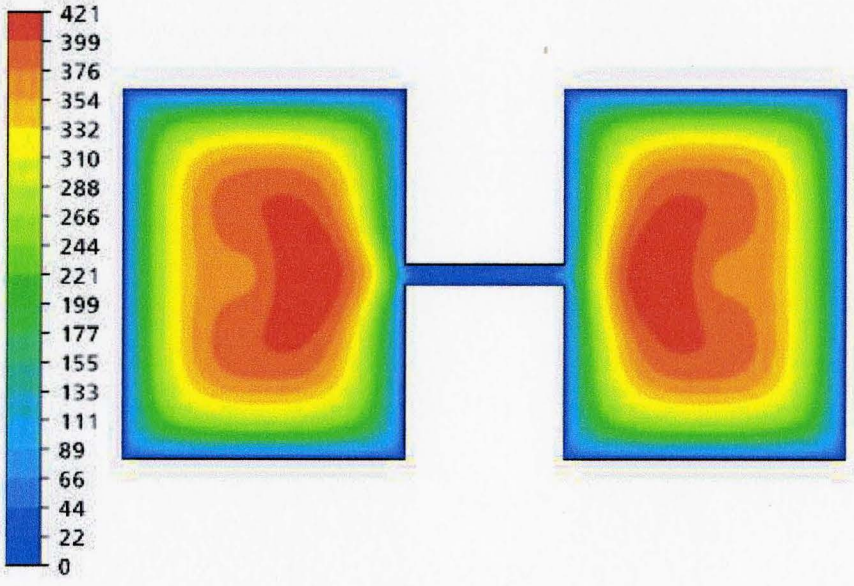

Figure 4.25: Normalized instantaneous eddy viscosity for case C_1

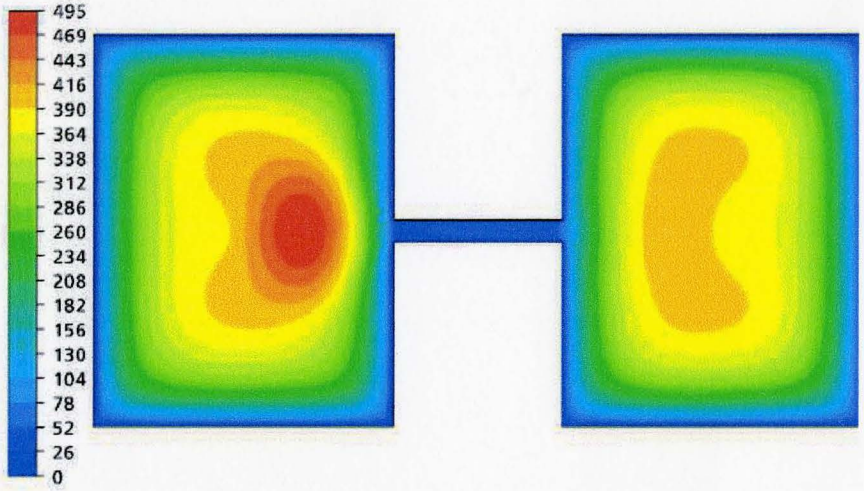

Figure 4.26: Normalized instantaneous eddy viscosity for case C_5 at time t

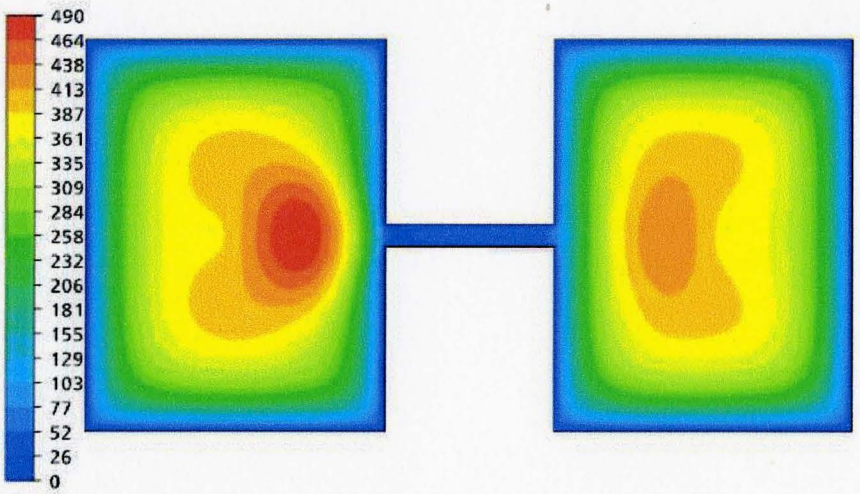

Figure 4.27: Normalized instantaneous eddy viscosity for case C_5 at time $t + \Delta t$

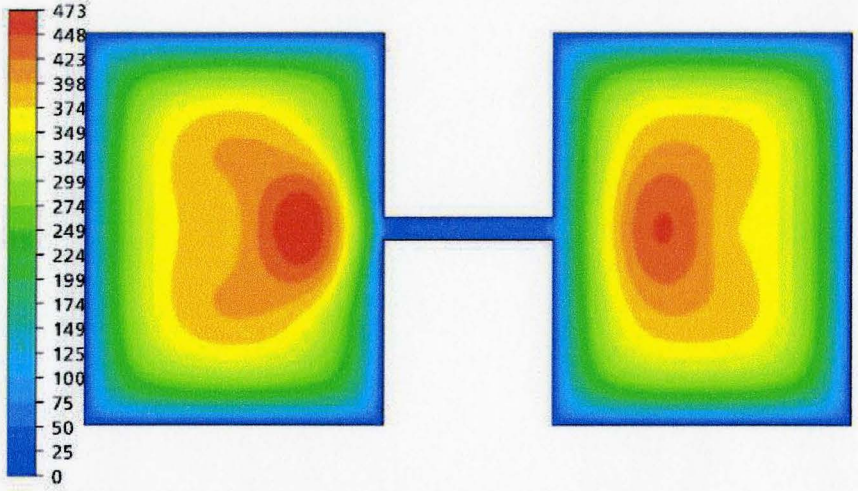

Figure 4.28: Normalized instantaneous eddy viscosity for case C_5 at time $t + 2 * \Delta t$

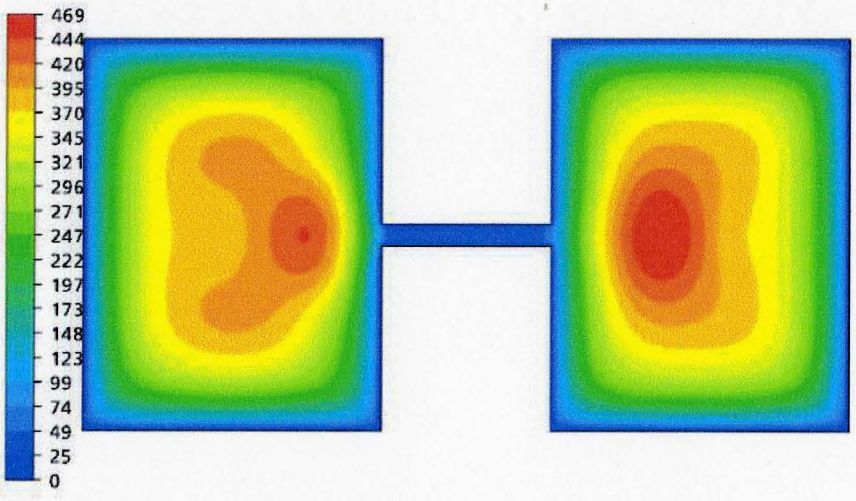

Figure 4.29: Normalized instantaneous eddy viscosity for case C_5 at time $t + 3 * \Delta t$

is zero and it increases with increasing distance from the walls, reaching its highest values at the regions near the centres of the two subchannels.

It is interesting to see snapshots of the instantaneous eddy viscosity at a cross-section. Figures 4.26, 4.27, 4.28 and 4.29 are contour plots of the predicted instantaneous eddy viscosity at different times for case C_5. The time lag between these snapshots is $\Delta t = 0.003$ sec. It is obvious that the core of the highest values of the eddy viscosity is gradually transferred from the left to the right channel with time.

4.4.7 Correlations

A way to identify the presence and determine the characteristics of the large scale structures present at the gap region is by generating the temporal autocorrelation functions. An autocorrelation function of a velocity component is basically a measure of how well a velocity value matches a time shifted value of itself as a function of time. In other words, if a value of a velocity component at a specific monitor point is close to its value after a time interval Δt, then the temporal autocorrelation function will have a value close to unity. In the opposite case, the value of the correlation function will be close to zero. So, in this way we can identify a repetitive or periodic pattern in the evolution of a variable field, such as velocities.

In figure 4.30, the autocorrelation functions of the span-wise, R_{ww}, and the axial, R_{uu}, velocity components from the experimental measurements [34] are presented. In the R_{ww} plot, the half cross-section of the gap together with the monitor

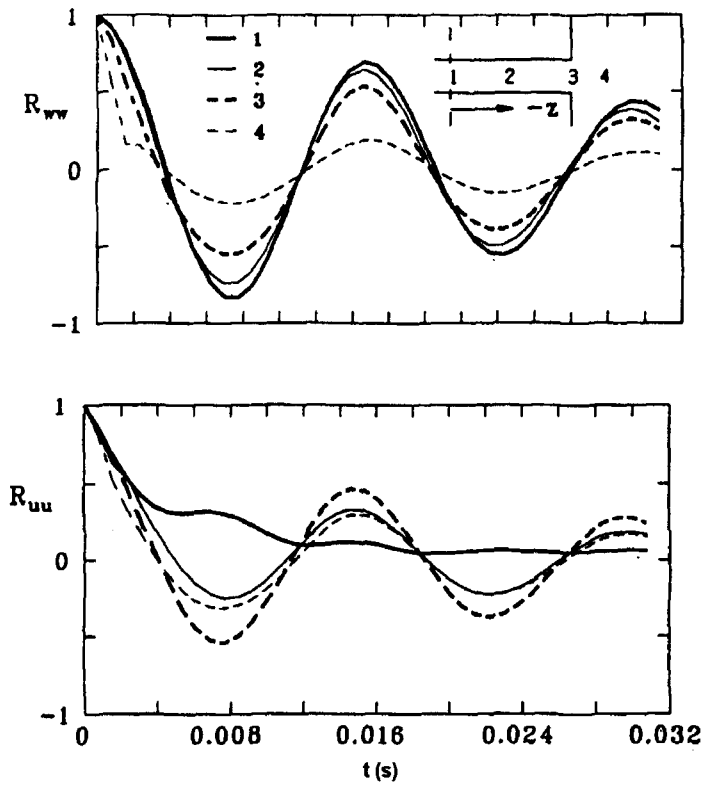

Figure 4.30: Autocorrelation functions measured at four positions on the symmetry line through the gap [34]

points (see also figure 4.1) can also be seen.

The same plots were created for cases C_1 and C_5 and they are presented in figures 4.31 and 4.32, respectively. First, for both the numerical and experimental results an oscillating pattern of the plots is observed. This clearly shows that the flow is not purely turbulent, but is superimposed by quasi-periodic oscillations. Second, as Meyer and Rehme [34] report, the autocorrelation function of u and w clearly show the dominant frequency of 68 Hz, taking the inverse of the time at which the correlation functions have their second maximum. The dominant frequencies in the

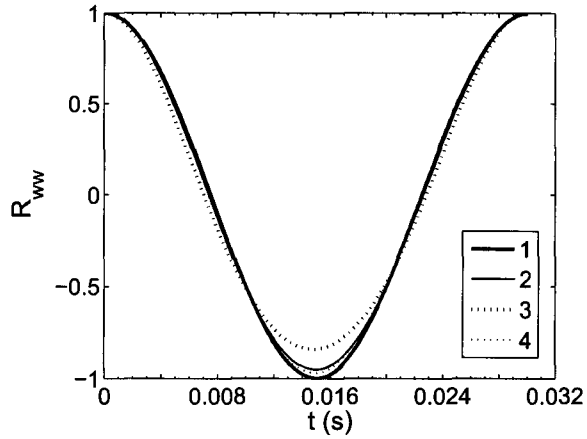

Figure 4.31: Span-wise, R_{ww} and stream-wise, R_{uu}, autocorrelation functions for case C_1

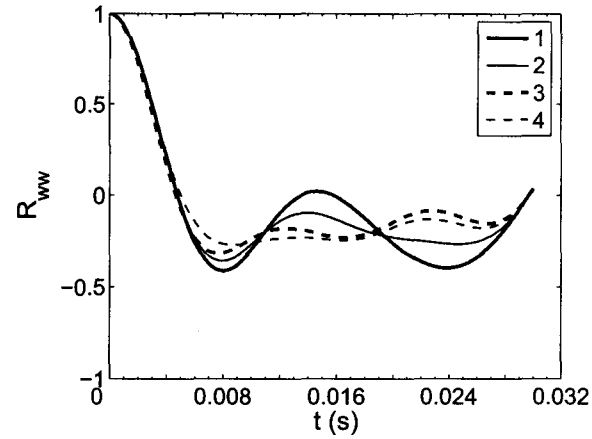

Figure 4.32: Span-wise, R_{ww} and stream-wise, R_{uu}, autocorrelation functions for case C_5

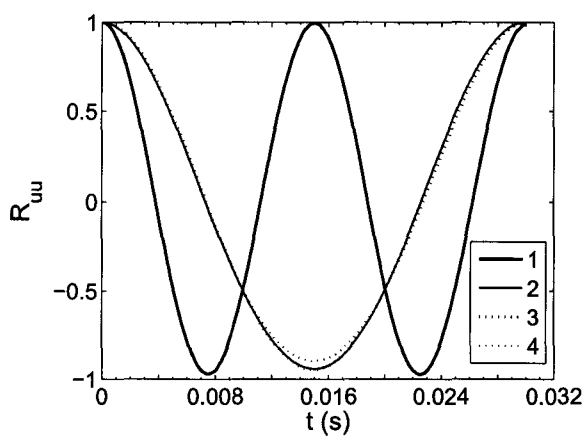

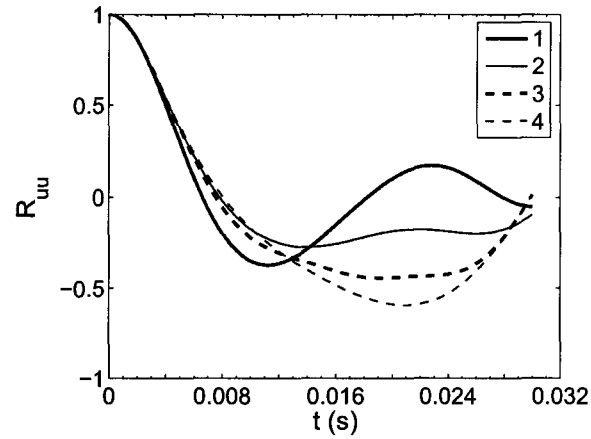

numerical results are somewhat different from the experiments and are discussed further in subsection 4.4.8.

The simulations show similar trends as observed in the experiments. In the case of the first order upwind results (case C_1) the period of the autocorrelation functions is more than two times higher than the respective experimental functions. The second order accurate results (case C_5) capture the experimental observations

better. For example, the autocorrelation functions for case C_5 and for the experiments damp out with time. However, this does not happen in case C_1, for which figure 4.31 shows that the plots seem to preserve their periods and peak values with time.

4.4.8 Power spectral density functions

As it was introduced in the previous subsection, the autocorrelation functions showed a periodic behaviour, which is an indication of the existence of large-scale periodic structures in the flow. The main frequencies of the flow structures can be identified by extracting the auto-power spectral density functions from the autocorrelation functions. The resulting auto-power spectral functions of the span-wise velocity component, w, for the four monitor points (see figure 4.1) for cases C_1 and C_5 can be seen in figures 4.33 and 4.34, respectively.

In figure 4.34 for case C_5, there is one clear peak frequency for all the four monitor points at a value of 58.6 Hz. As already mentioned, the respective peak frequency, reported by Meyer and Rehme [34], was at the value of 68 Hz. The code predicted the experimental peak frequency fairly well with an error of about 14%. Other than the main peak frequency in figure 4.34, there are some more local maximums in the power-spectral plots.

If the auto-power spectral density functions had only one clear peak frequency, figure 4.32 would be periodic. Although, this is not the case for the second order accurate cases, represented by case C_5, the first order upwind runs, represented by

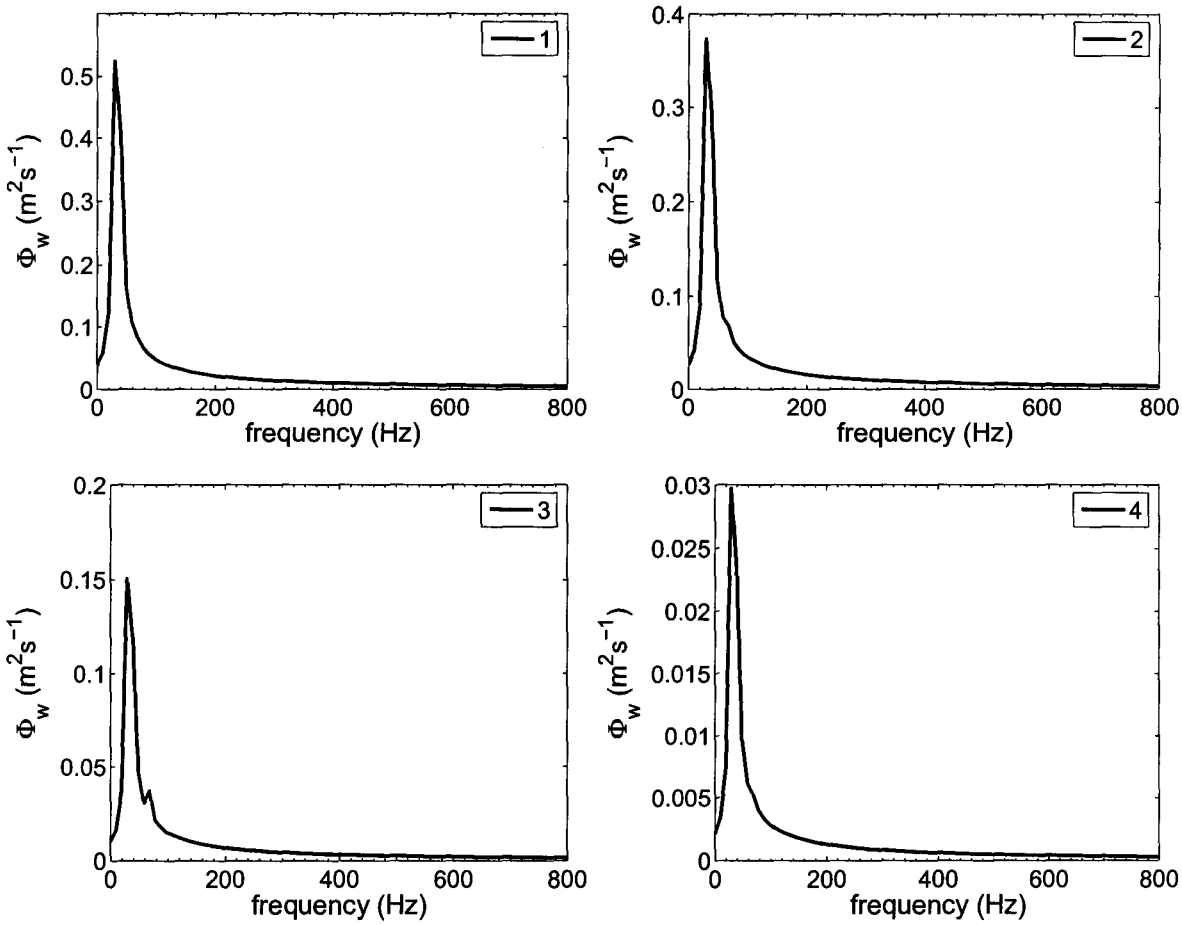

Figure 4.33: Span-wise auto-power spectral density functions at the four monitor points - Case C_1

case C_1, showed this clearly periodic pattern. This is also verified by the auto-power spectral density functions for case C_1, plotted in figure 4.33, where only one peak frequency is predicted at the value of 29.3 Hz. Of course, this value is less than half the experimental peak frequency.

In both cases, C_1 and C_5, the value of the power spectral density function at the main peak frequency is highest at the gap centre (point 1) and it decreases toward

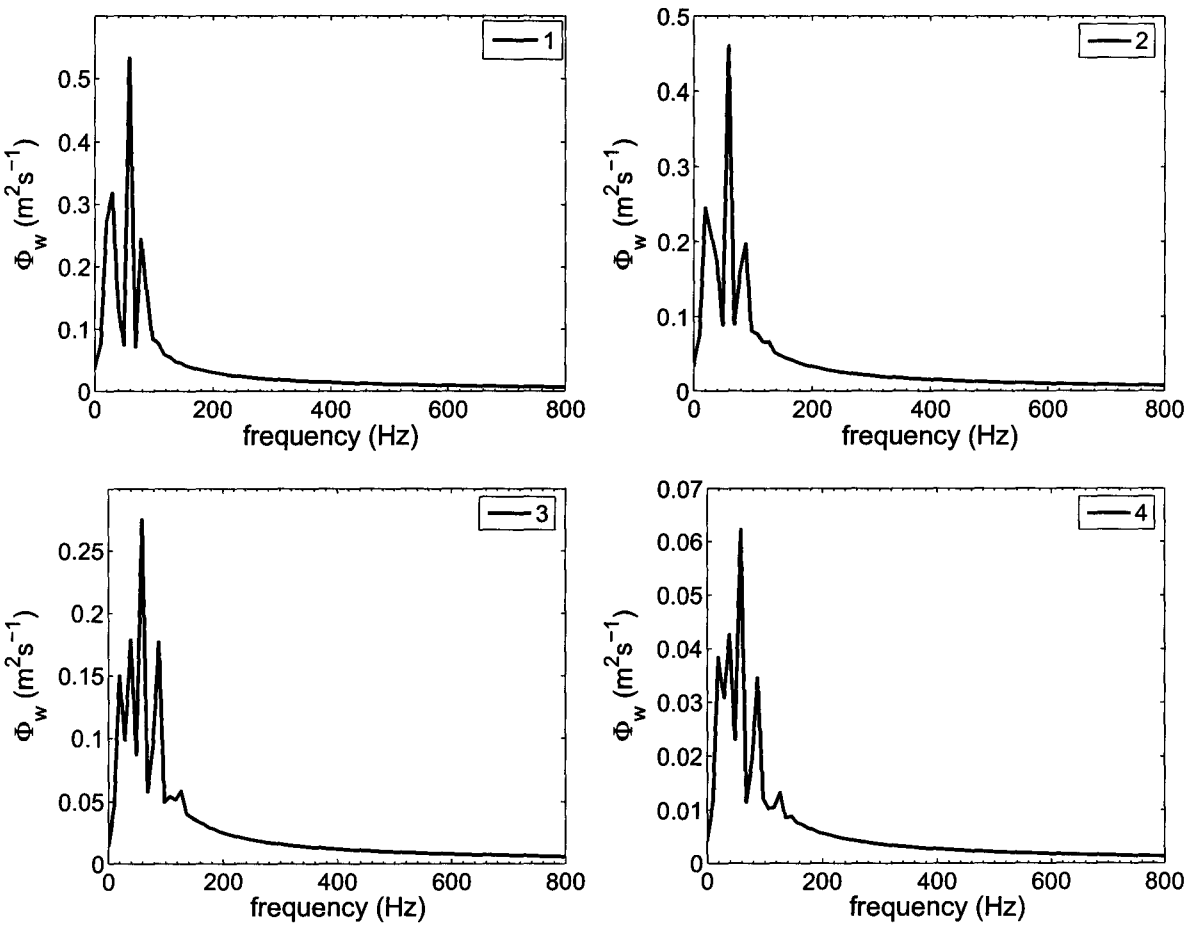

Figure 4.34: Span-wise auto-power spectral density functions at the four monitor points - Case C_5

the edge of the gap (point 3). This behaviour was also observed in the experiments.

4.4.9 Reynolds number dependence

Meyer and Rehme [34] also did experiments with different Reynolds numbers for some of the compound channel geometries used. The results of this study are summarized in figure 4.35. In figure 4.35 the vertical axis is the frequency at which a peak in the

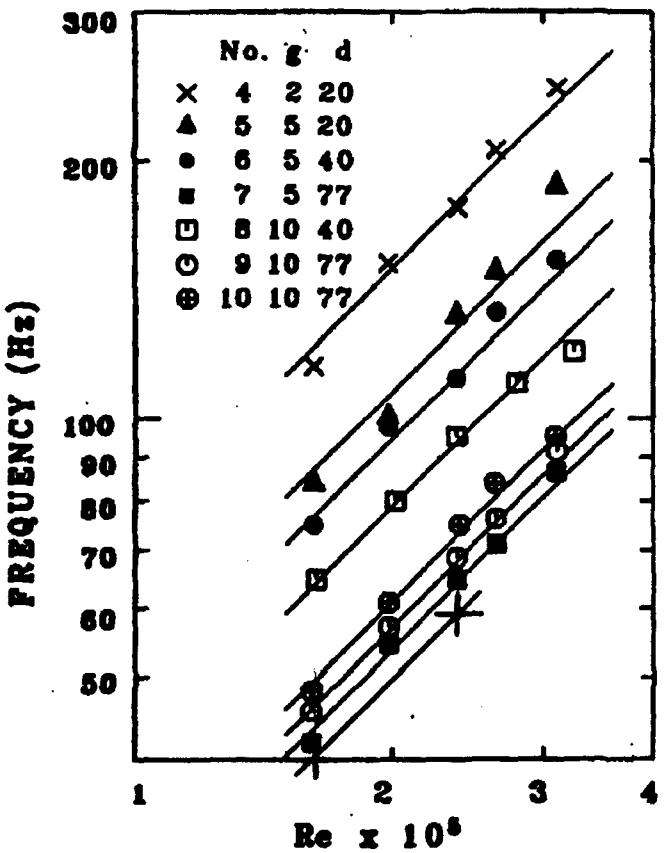

Figure 4.35: Frequency of the large-scale oscillations for different gap geometries versus the bulk Reynolds number. Adapted from Meyer and Rehme [34]

spectra was clearly detectable [34]. The horizontal axis is the bulk Reynolds number, based on the bulk average axial velocity, U_b, and the hydraulic diameter, D_h, of the channel neglecting the gap. As it can be seen from the figure's legend there are specifically seven geometries for which the results are provided. For all these seven geometries as the Reynolds number increases, the peak frequencies increase.

A simulation using the second order accurate in space scheme was carried out for a selected lower Reynolds number. Specifically, from figure 4.35 for case No.9, the

Reynolds number of $1.62*10^5$ was selected. From the results of this simulation, figures similar to figure 4.34 were created. From these plots, the resulting peak frequency at which peaks in the spectras were observed, was 39.1 Hz. The respective experimental frequency from figure 4.35 for case no.9 was 45.8 Hz. Again, the numerical peak frequency was close to its experimental value and the error on the prediction was exactly the same with the error in the case of the higher Reynolds number (case C_5). This is clearly shown in figure 4.35 where the resulting numerical points are added using the cross symbol and they are connected with a line. It can be observed that the lower Reynolds number numerical point is very near the horizontal axis, which corresponds to a frequency of 40 Hz. Moreover, the trend of the peak frequency versus Reynolds number variation was reproduced by the simulations.

4.4.10 Sensitivity to the length of the channel

In this subsection a study on the sensitivity to the length of the channel is carried out through the comparison of case C_5 in which the channel's length was $L = 730$ mm with the results of case C_7 in which a longer channel was used. Specifically, the simulation setup of case C_7 was the same as in case C_5, except for the length of the channel which was $L = 992.8$ mm and the mesh used. The mesh structure used in case C_7 was based on mesh M_5 (see table 4.2), resulting in a total number of nodes of 378,556. The comparison of cases C_5 and C_7 follows the flow of analysis in the previous subsections, which refer to the comparison of cases C_1 and C_5 with the

experimental measurements.

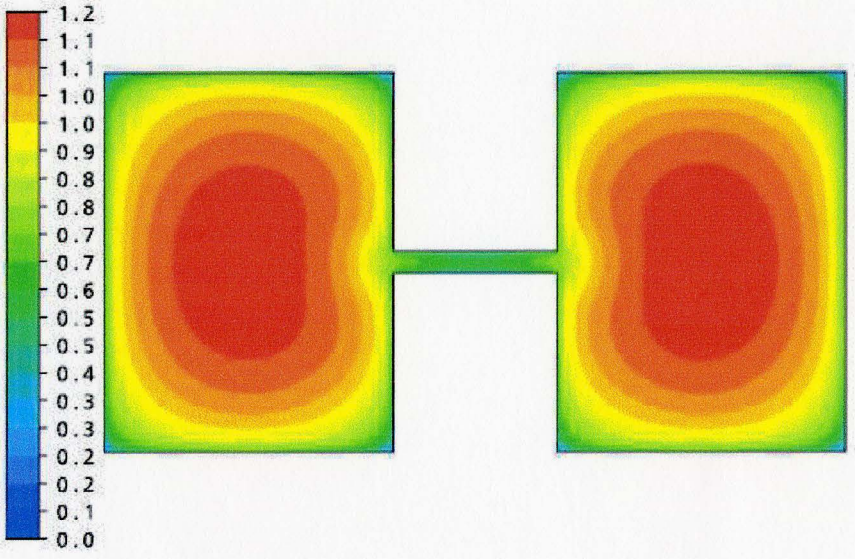

Figure 4.36: Normalized axial velocity contour plot for case C_7

The specific choice of the new length was based on two factors. First, the length of the channel could not be too high, since its numerical implementation would not be computationally affordable. Second, based on the wavelength of the structures reported by Meyer and Rehme [34], the new channel's length was decided to have this value in order to capture approximately five structures of one sequence and six structures of the other sequence in contrast to the initial length, which was chosen in order to capture four structures of alternate sequence. In addition, care had been taken in order that the length of the longer channel not to be an integral multiple of the lenth of the shorter channel.

In figure 4.36 the contour plot of the normalized axial velocity for case C_7 can

be observed. It is reminded that for the normalization of the axial velocity, the bulk velocity of the flow, $U_b = 21.5$ m/s, was used. Also, figures 4.37 and 4.38 show the contour plot of the instantaneous span-wise velocity and the instantaneous velocity vector plot, respectively, at the (x, z) symmetry plane through the gap (figure 4.10).

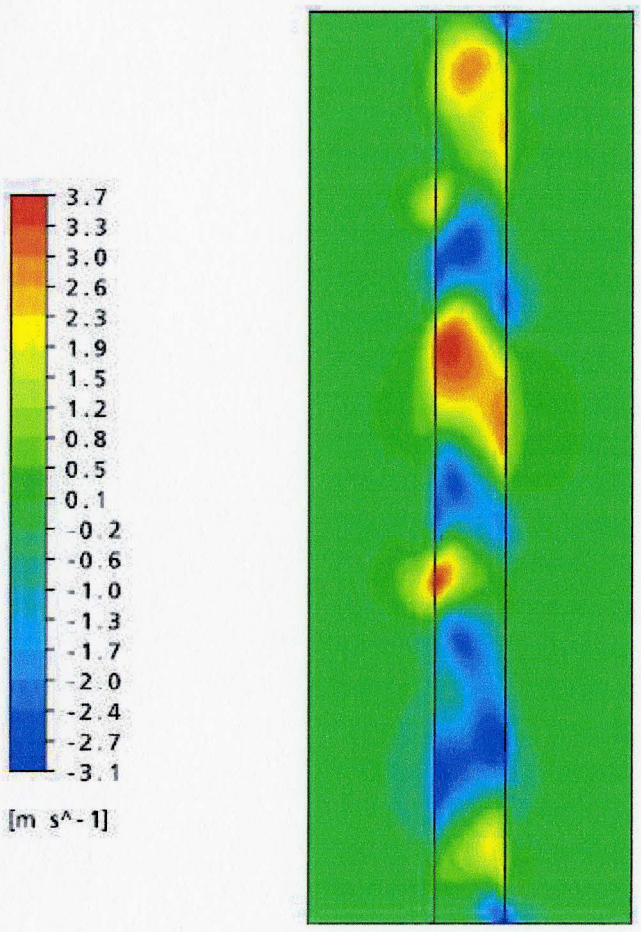

Figure 4.37: Instantaneous span-wise velocity contour plot for case C_7

Compared to figure 4.9 it can be seen that the axial velocity distribution in

both cases was similar. Moreover, comparing figures 4.37 and 4.12, it is observed that the distance between repeating values of the span-wise velocity in the axial direction is roughly close. The repeating patterns of the span-wise velocity values with time are discussed below through the calculated temporal autocorrelation functions and the respective auto-power spectral density functions.

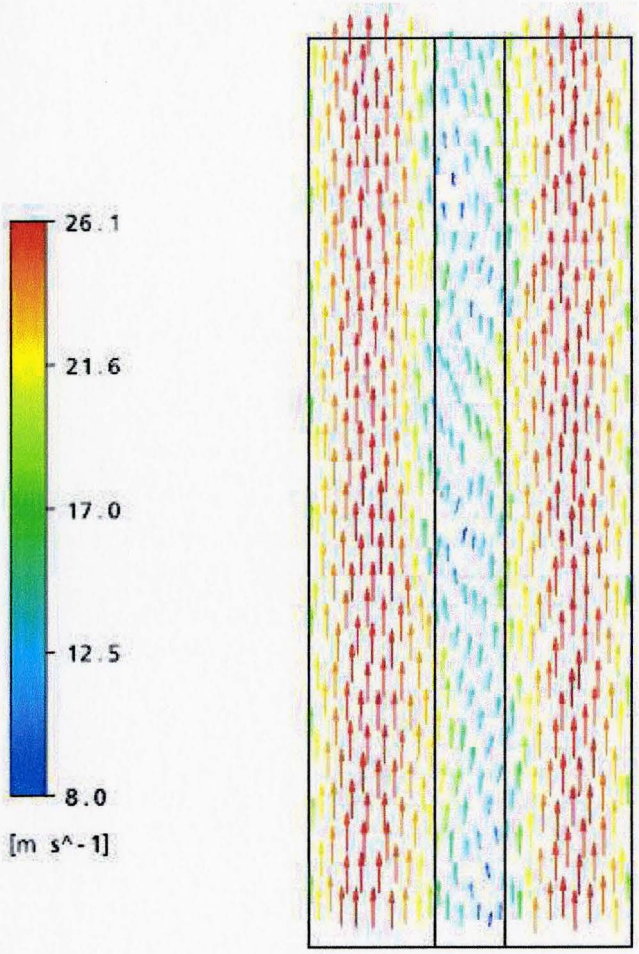

Figure 4.38: Instantaneous velocity vector plot for case C_7

Figure 4.39 shows the instantaneous span-wise velocity time traces at the gap centre (w_1) and at the gap edge (w_3), together with the instantaneous axial velocity time trace at the gap edge (u_3) for case C_7. In this figure the characteristics of the two components of the instantaneous velocity at the gap centre and at the gap edge were similar to the respective charecteristics as discussed for case C_5 in subsection 4.4.5 (figure 4.17).

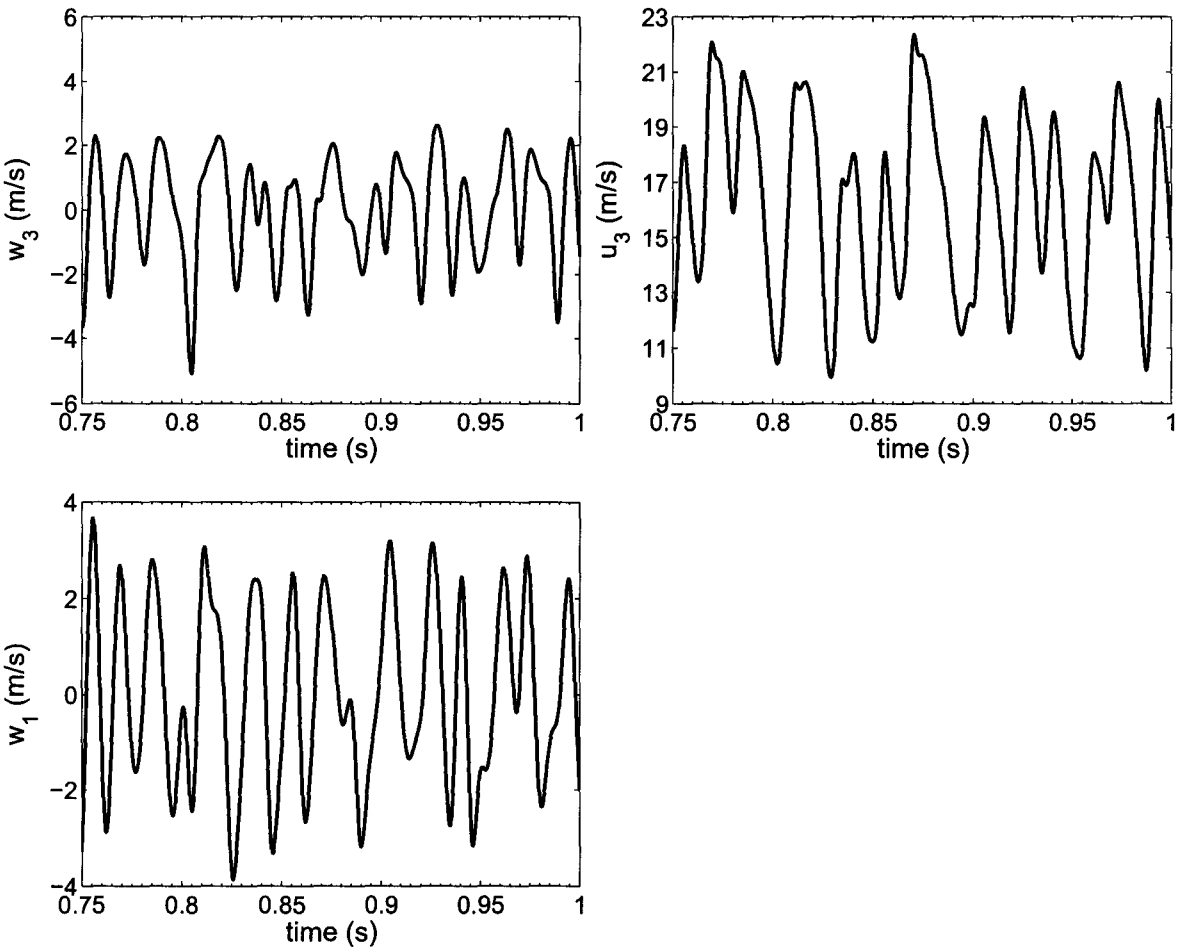

Figure 4.39: Time traces of the axial (u) and the span-wise (w) velocity for case C_7

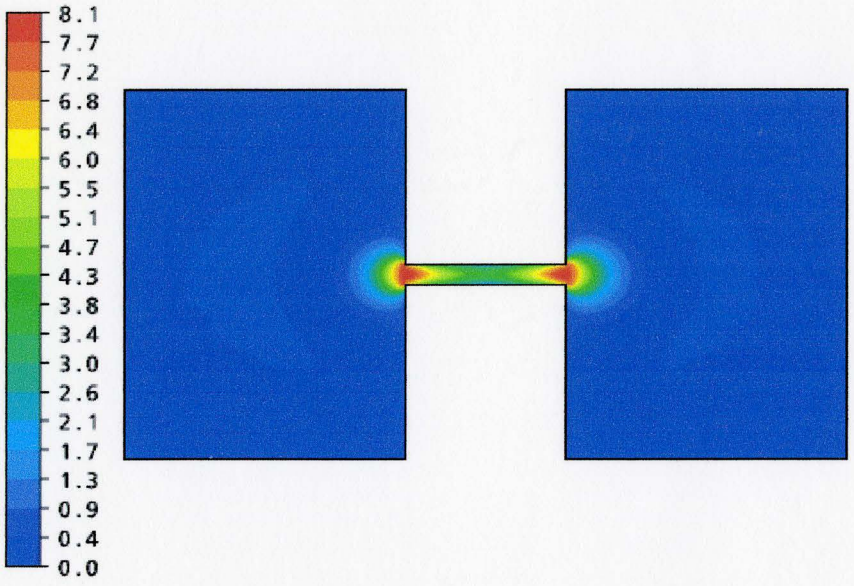

Figure 4.40: Contours of $\frac{\tilde{k}}{u_\tau^2}$ for case C_7

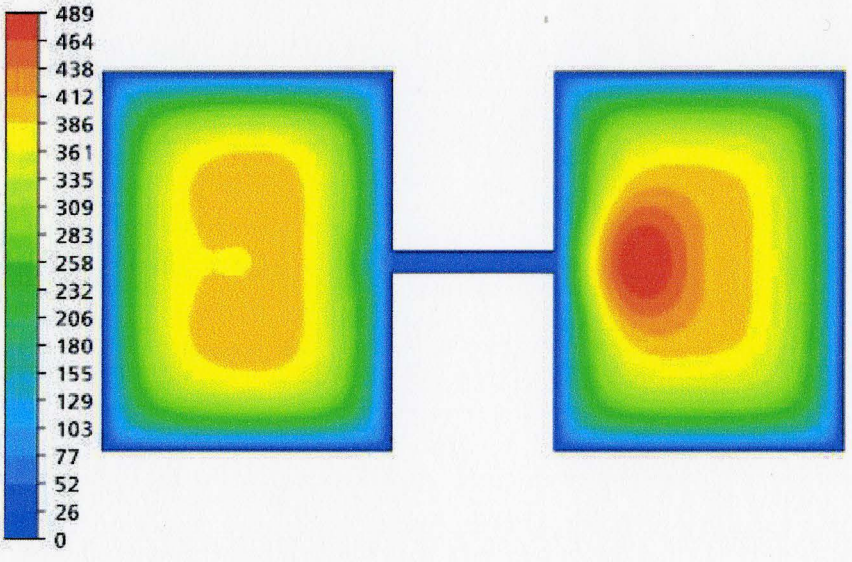

Figure 4.41: Normalized instantaneous eddy viscosity for case C_7

For the sake of completeness, the contour plots of the normalized kinetic energy $\tilde{k}$ (equation 4.5) and the normalized instantaneous eddy viscosity for case C_7 are given in figures 4.40 and 4.41. Comparing these two figures to figures 4.22 and 4.23 the same trends for $\frac{\tilde{k}}{u_\tau}$ and the normalized eddy viscosity can be observed. Figure 4.40 shows that at the gap edges the predicted values of $\frac{\tilde{k}}{u_\tau}$ were slightly higher than in case C_5 (figure 4.22) and that the higher values of the normalized $\tilde{k}$ cover more space in the vicinity of the gap edges. It is interesting to notice that the highest values of the eddy viscosity, as seen in figure 4.41, were at the right channel compared to case C_5 for which at a different time step the region with the highest values of the eddy viscosity was at the left channel (figure 4.23).

In figures 4.42 and 4.43 the span-wise and axial temporal autocorrelation functions and the span-wise auto-power spectral density functions at the four monitored points are given, similarly to figures 4.32 and 4.34. It is reminded that the four monitor points can be seen in figure 4.30. The temporal autocorrelation functions have an oscillating pattern, as expected, based on the analysis in subsection 4.4.7. The main difference with figure 4.32 is that the span-wise autocorrelations for case C_7 were closer to the respective experimental correlation functions (figure 4.30). Specifically, as shown in figure 4.42, the span-wise autocorrelation functions at all four monitor points have roughly the same period similarly to the respective span-wise autocorrelation functions from the experiments.

This is also justified from the span-wise auto-power spectral density functions,

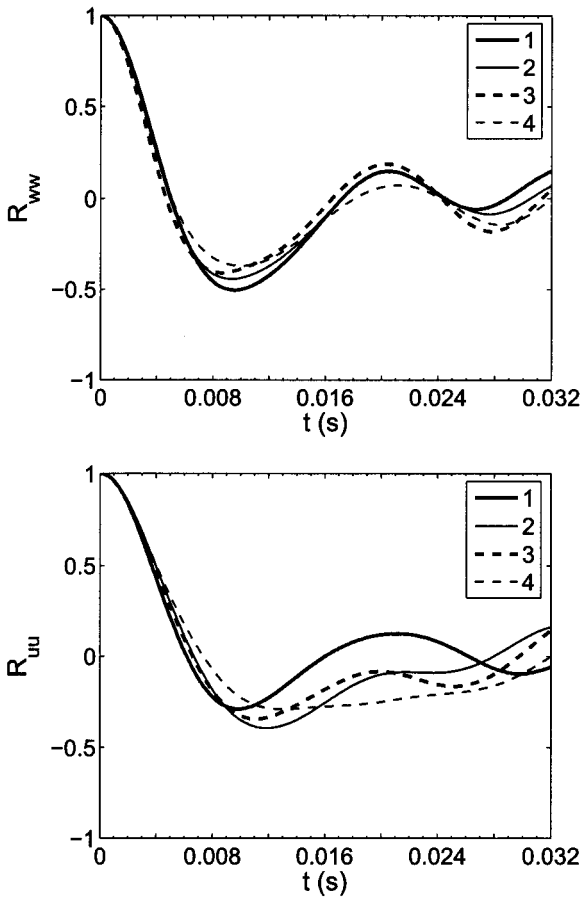

Figure 4.42: Span-wise, R_{ww} and stream-wise, R_{uu}, autocorrelation functions for case C_7

shown in figure 4.43. The clear oscillating pattern of approximately the same period at all four monitor points of the span-wise autocorrelation functions for case C_7 can be explained by their underlying peak frequencies at the four monitor points. As it is seen from figure 4.43, at each monitor point the main peak frequency was at the value of 58.6 Hz, as it was also observed for case C_5 (figure 4.34). The main difference of case C_7 compared to case C_5 is that in the neighbourhood of the main peak frequency there were not as many other peak frequencies as it was observed in case C_5.

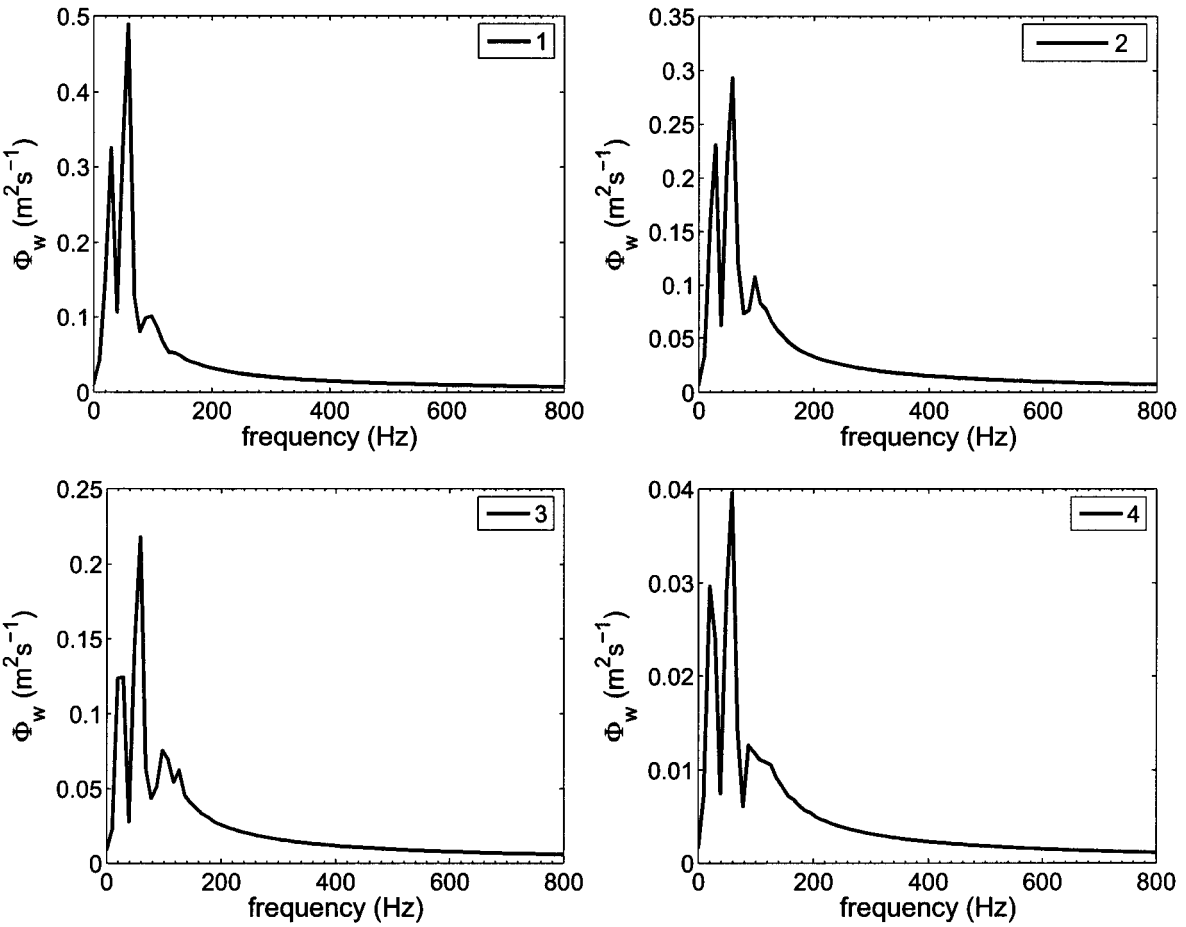

Figure 4.43: Span-wise auto-power spectral density functions at the four monitor points - Case C_7

Summarizing, it was observed that the increase of the channel's length did not significantly affect the predicted characteristics and dynamics of the flow by the SA model. In both cases C_5 and C_7 the predicted main peak frequency of the auto-power spectral density functions was 58.6 Hz, which was about 10 Hz lower than the respective experimental frequency.

4.4.11 Comparison with the results of $k-\varepsilon$ model

In this subsection the main results obtained using the $k-\varepsilon$ model (case C_8) are presented and discussed together with a comparison with the results using the SA model. The analysis of the results follows the same flow as in subsection 4.4.10. The mesh used with the $k-\varepsilon$ model was the reference mesh, M_1 (see table 4.2). Essentially, the simulation setup in case C_8 was the same with case C_5, except for the turbulence model used. Because of this, the results of case C_8 were compared with the results of the already discussed case C_5 (see table 4.4).

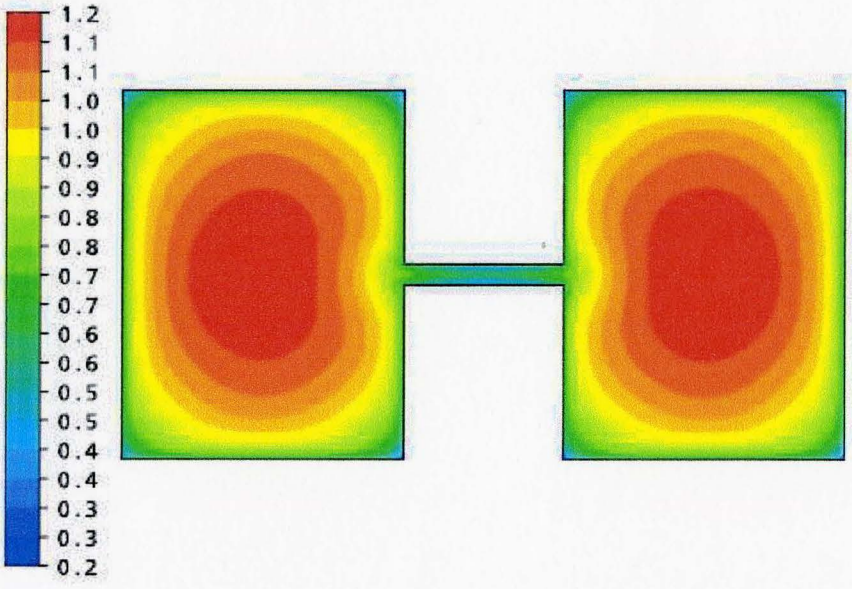

Figure 4.44: Normalized axial velocity contour plot for case C_8

Figure 4.44 shows the normalized axial velocity contour plot for case C_8. Comparing figure 4.44 to figure 4.9, it is observed that there are no significant differences

between them.

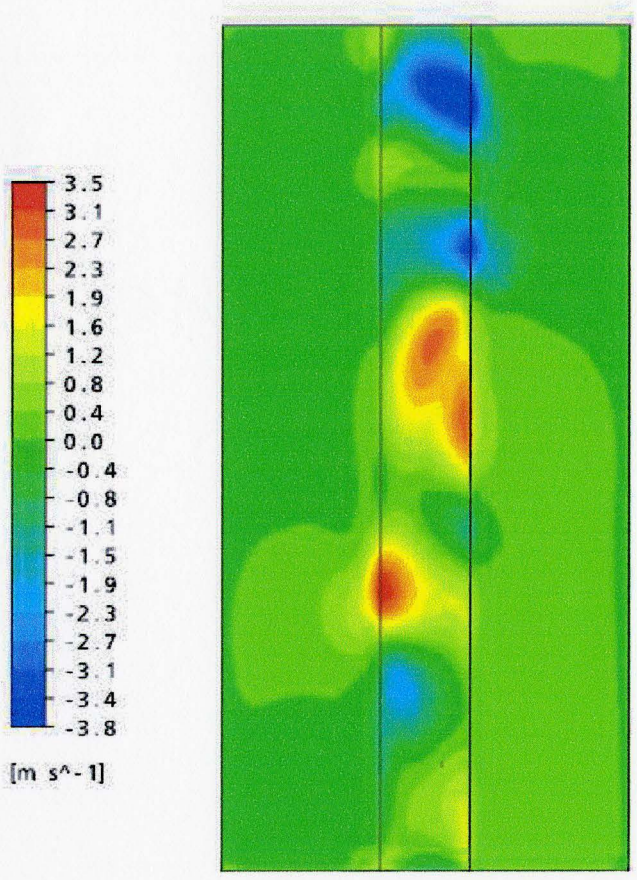

Figure 4.45: Instantaneous span-wise velocity contour plot for case C_8

Figures 4.45 and 4.46 present the instantaneous span-wise velocity contours and the instantaneous velocity vectors, respectively, at the (x, z) symmetry plane through the gap (figure 4.10) for case C_8. In these figures it is observed that the $k-\varepsilon$ model was able to predict flow structures and the corresponding wiggly pattern of the velocity field at the gap region. Comparing the velocity snapshots in figures

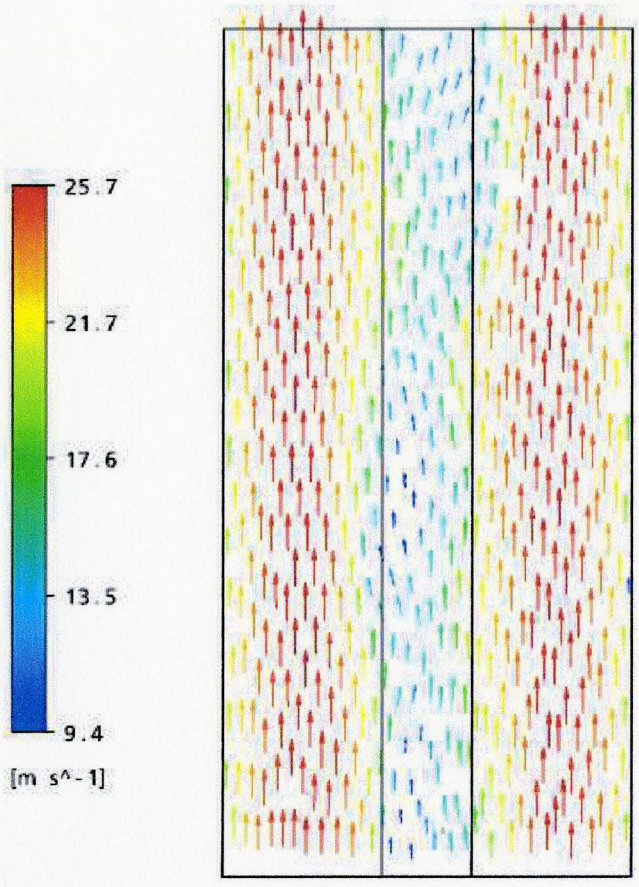

Figure 4.46: Instantaneous velocity vector plot for case C_8

4.45 and 4.46 with the respective velocity snapshots for case C_5 in figures 4.12 and 4.14 it is observed that they look similar. A more detailed analysis and comparison of the dynamics of the flow pulsations for cases C_5 and C_8 is carried out in the following discussion through the comparison of the temporal autocorrelation and the auto-power spectral density functions.

Similarly to figure 4.17, figure 4.47 shows the time traces of the span-wise

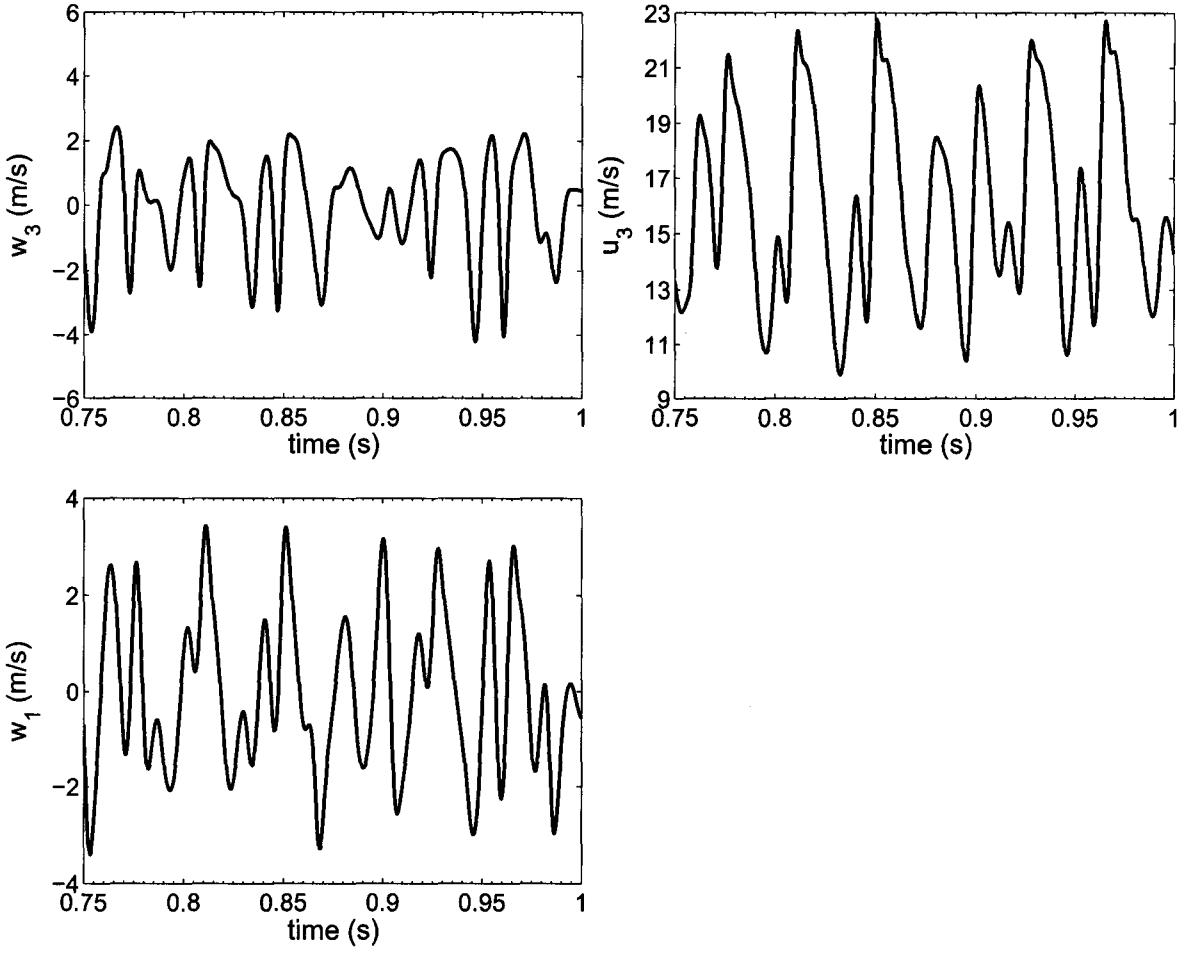

Figure 4.47: Time traces of the axial (u) and the span-wise (w) velocity for case C_8

velocity component at the gap centre, w_1, and the gap edge, w_3, and the stream-wise velocity component, u_3, at the gap edge for case C_8. Although the frequencies of the velocity time traces in case C_8 (figure 4.47) seem to be different from the respective time traces in case C_5 (figure 4.17), the ranges of magnitude of the velocity values were the same for both cases. Furthemore, similarly to case C_5, in case C_8 the strong negative skewness of the span-wise velocity at the gap edge was observed.

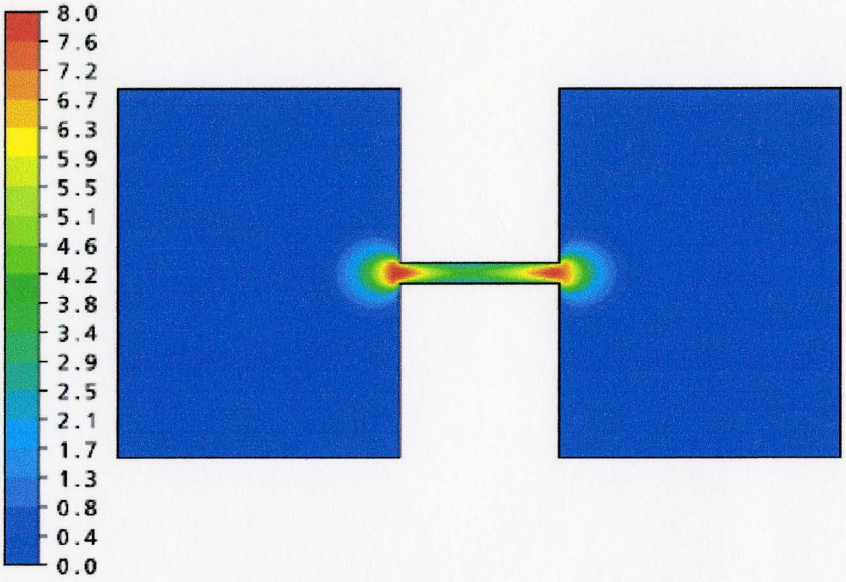

Figure 4.48: Contours of $\frac{\tilde{k}}{u_\tau^2}$ for case C_8

In figure 4.48 there is a contour plot of the normalized kinetic energy $\tilde{k}$, as it was calculated using equation 4.5. This contour plot roughly resembles the respective contours of the normalized $\tilde{k}$ for case C_5 as seen in figure 4.22. The range of the values was the same and both turbulence models predict two peaks of the same value at the corners of the gap. Similarly to figure 4.22, figure 4.48 shows that the value of $\tilde{k}$ at the bulk flow regions of the two channels was close to zero.

Since the $k - \varepsilon$ model solves a transport equation for the turbulence kinetic energy, it is of interest to create contours of the normalized instantaneous turbulence kinetic energy at a cross-section plane. As in figure 4.48, the instantaneous turbulence kinetic energy in figure 4.49 was normalized by the square of the average friction

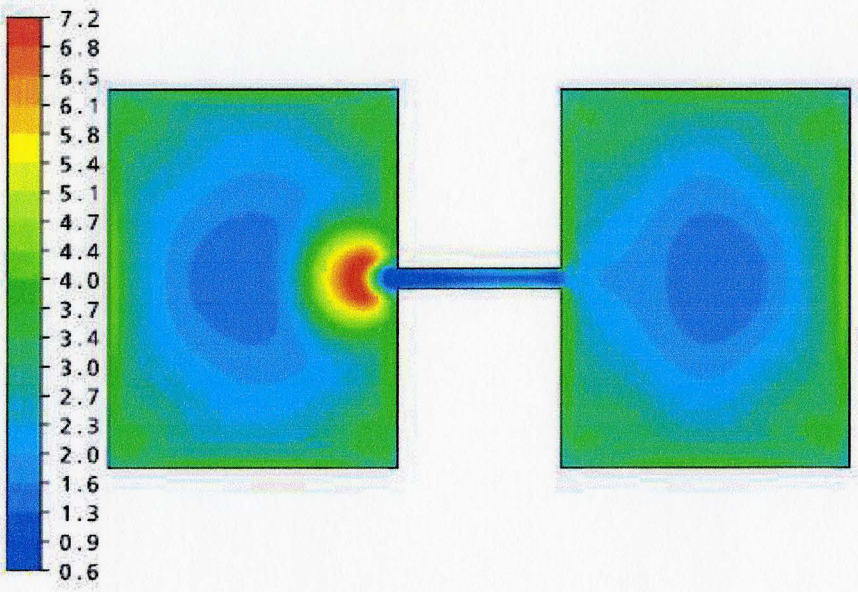

Figure 4.49: Contours of the instantaneous normalized turbulence kinetic energy for case C_8

velocity, $u_\tau = 0.924$ m/s. The fact that the kinetic energy $\tilde{k}$ should not be confused with the modelled turbulence kinetic energy is justified by the comparison of figures 4.48 and 4.49. As it was expected, figure 4.49 shows that turbulence kinetic energy is produced and reaches its local maximum values at the near wall regions (green regions near the walls). This was not observed in the respective contour plots of $\tilde{k}$ neither for case $C8$ (figure 4.48) or for case C_5 (figure 4.22) in which $\tilde{k}$ was zero at the mean flow of the two channels and at the near wall regions.

The span-wise and stream-wise autocorrelation functions at the four monitor points as they were obtained from the results of the $k - \varepsilon$ model are presented in figure 4.50. Although the autocorrelation functions for case C_8 have in general the

expected oscillating pattern, their period was different than in case C_5, as shown in figure 4.32. This difference was clearly revealed from the comparison of the span-wise auto-power spectral density functions at the four monitor points for cases C_5 and C_8.

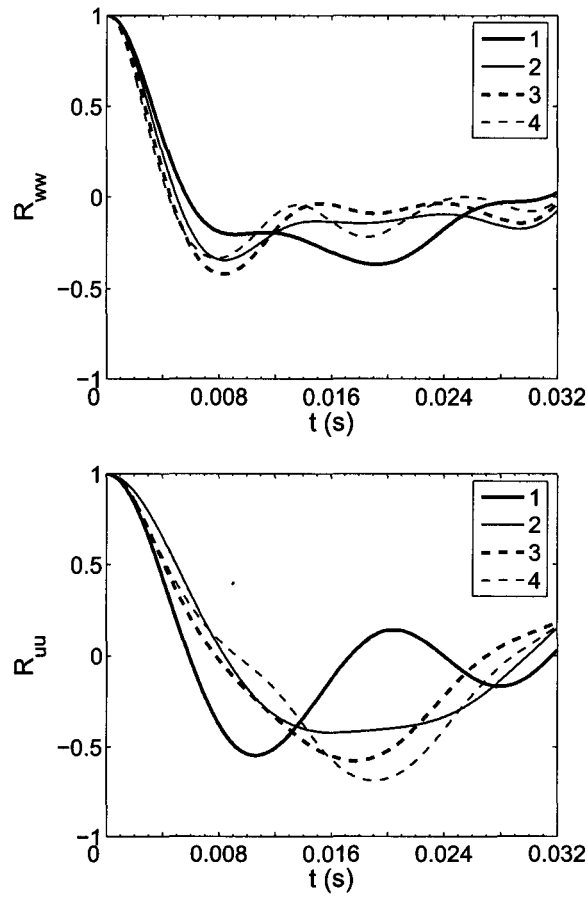

Figure 4.50: Span-wise, R_{ww} and stream-wise, R_{uu}, autocorrelation functions for case C_8

The span-wise auto-power spectral density functions at the four monitor points for case C_8 are presented in figure 4.51. First, in this figure it can be observed that the main peak frequency was not the same at all four monitor points. In contrast, the main peak frequency in case C_5 (figure 4.34), similarly to the experiment, was

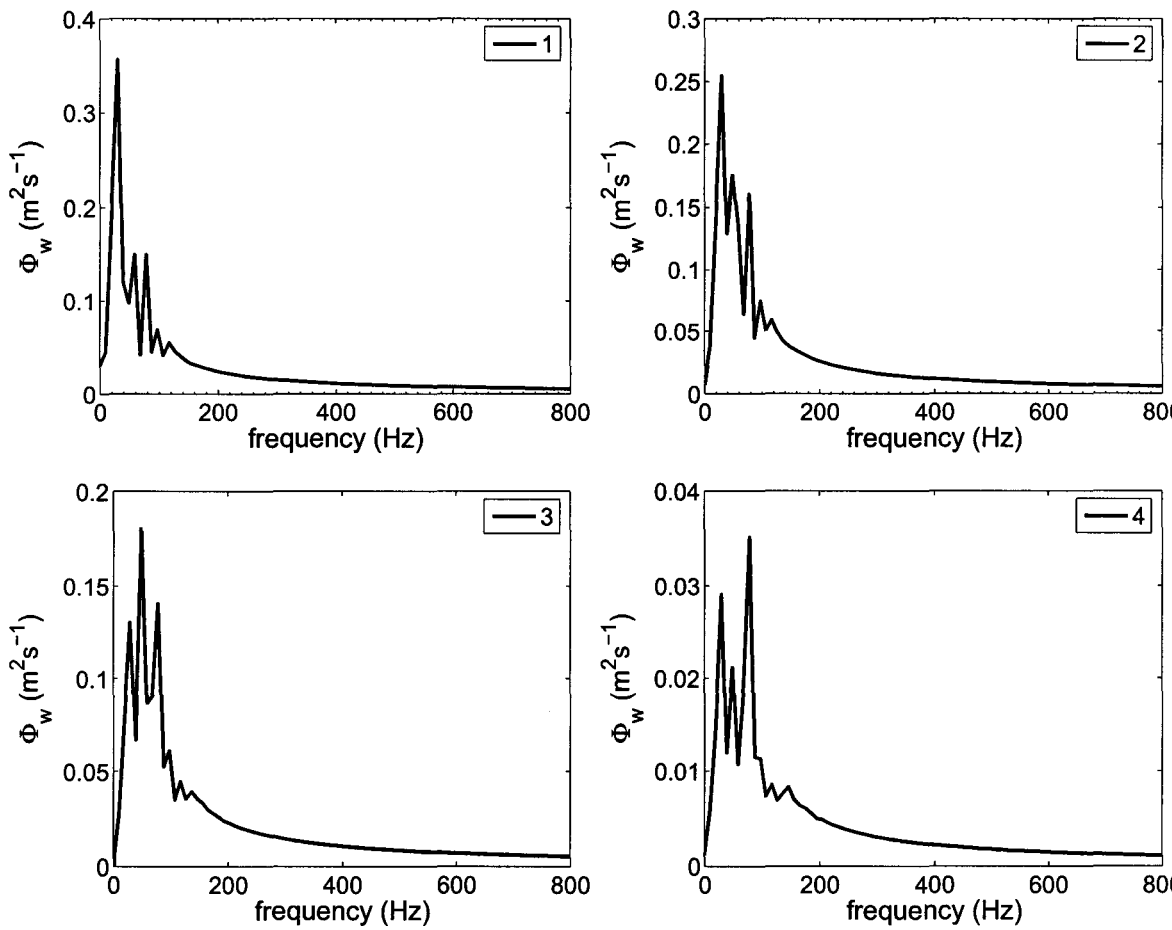

Figure 4.51: Span-wise auto-power spectral density functions at the four monitor points - Case C_8

the same at all four monitor points. Second, there was not any monitor point at which the main peak frequency had the value of 58.6 Hz, as it was observed at all four monitor points in case C_5 (figure 4.34). Specifically, the main peak frequency at monitor points 1 (gap centre) and 2 was 29.3 Hz, while at point 3 (gap edge) was 48.8 Hz and at point 4 was 78.1 Hz. This is an important advantage of the predictions of the SA model, compared to the predictions of the $k-\varepsilon$ model, because in contrast

to the $k-\varepsilon$ model, the SA model predicts one consistent main peak frequency at all four monitor points which is very close to its experimental value of 68 Hz.

Since the primary purpose of this research was to choose a RANS model that would capture and predict as faithfully as possible the dynamics of the flow pulsations at the gap region, the SA model seems to be a better choice than the $k-\varepsilon$ model. In order for a solid conclusion to be drawn from the comparison between these turbulence models for the studied case, a thorough study has to be done for the $k-\varepsilon$ model, similarly to the study that has been done for the SA model.

Chapter 5

Closure

5.1 Summary and Conclusions

Numerical studies of the flow pulsation phenomenon in a subchannel geometry was carried out, using the SA based turbulence model. The numerical results were validated against the experimental data of Meyer and Rehme [34]. Following are the findings of the SA model.

1. The axial velocity distributions, predicted by all the cases were in agreement with the experimental measurements.

2. The time traces of the span-wise velocity showed the expected behaviour at the gap, which connects the two rectangular subchannels. The model was successful in capturing large-scale flow oscillations at the gap region.

3. The instantaneous velocity components at the monitor points were within the

experimental range.

4. The turbulence characteristics of the flow field were estimated through the combination of the kinetic energy $\tilde{k}$ (equation 4.5) and the modelled eddy viscosity. The kinetic energy $\tilde{k}$ at the gap region followed the trend of the turbulence kinetic energy as reported in the experiments.

5. The frequency analysis, through the correlation functions and the power spectras showed the expected periodic nature of the fluid flow, justifying the argument that the most important contribution to the cross-flow mixing process is the presence of large-scale oscillations in the gap region. The computed peak frequency in the case of the second order accurate in space results was very close to its experimental value.

6. The study of the dependence of the frequency spectra to the Reynolds number was initiated and the initial results proved to follow the experimental trend. Specifically, the peak frequency of the power spectras increase with increasing Reynolds number.

7. A case study on the effect of the length of the channel had been carried out. This case study showed that the higher length of the channel didn't significantly affect the characteristics and the dynamics of the flow field as predicted from the SA model.

8. The commonly used $k - \varepsilon$ turbulence model was also used to predict the flow

in the twin rectangular subchannel. From an initial comparison, it seems that the SA model does better on predicting the dynamics of the flow structures at the gap region.

The two advection schemes used were the first order upwind and the second order accurate in space scheme. Referring to table 4.4, the two cases used in the study of the effect of the advection scheme were case C_1, for the former scheme and case C_5 for the latter. This study led to the following conclusions.

1. The axial velocity distributions in both cases were very well predicted, resulting in minor differences between the results.

2. The time traces of the span-wise velocity in the first order upwind cases had a distinctive periodic and symmetric pattern. This was not observed in the second order accurate cases. However, a less organized pattern was also observed.

3. The instantaneous velocity components at the monitor points in case C_1 had a symmetric and periodic pattern, while in case C_5 this behaviour was not observed. In case C_5, the instantaneous velocity plots resemble more the experimental plots. Nonetheless, in both cases the experimental velocity ranges were roughly captured, with case C_5 predicting slightly higher velocity values than case C_1.

4. The predictions of the turbulence quantities in the two cases have qualitatively the same behaviour, with the results in case C_5 being quantitavely closer to the

experimental data.

5. The correlation functions and the power spectral density functions explained the main differences between the two cases, such as the oscillating characteristics of the instantaneous velocity time traces. The second order accurate cases do much better in predicting the experimental peak frequencies, while the first order upwind cases underpredict the peak frequencies by roughly a factor of two.

5.2 Recommendations for Future Work

1. The effect of the Reynolds number on the frequency spectras can be further explored by running cases with different Reynolds numbers and validating the results with the experimental data.

2. Following the validation of the effect of the Reynolds number, a study on the threshold Reynolds number, below which the periodic flow pulsations do not exist can be carried out. In addition, simulations with higher Reynolds numbers beyond the maximum value used by Meyer and Rehme [34] can be performed.

3. The SA model can be directly used for simulations of turbulent flows in rod bundle geometriess.

Appendix A

Evaluation of the Auto-power Spectral Density Functions

Below is the script which was used in Matlab to evaluate the Fourier transform of the temporal autocorrelation functions, resulting to the auto-power spectral density function plots. In the third line of the script, $w1$ is the matrix, which refers to the span-wise velocity fluctuations at the gap centre (monitor point 1). It is calculated as: $w1 = W1 - \overline{W}1$, where $W1$ is the predicted span-wise velocity at each time step at monitor point 1 and $\overline{W}1$ is the time mean span-wise velocity at monitor point 1. Similarly, the same script was used for all the four monitor points.

```
clc;
clear all;
w1=[...]
N=length(w1);
for j=0:1023
        i=1;
        sum=0;
        while ((i+j) ≤ N)
                sum=sum+(w1(i)*w1(i+j));
                i=i+1;
        end
        R(j+1)=sum/(i-1);
end
M=length(R);
R'
X=fft(R);
Y=sqrt(X.*conj(X))/(M);
fs=10000;
k=-M/2:M/2-1;
plot(k*fs/M,fftshift(Y));
```

Bibliography

[1] A. M. M. Aly, A. C. Trupp, and A. D. Gerrard. Measurements and Prediction of Fully Developed Turbulent Flow in an Equilateral Triangular Duct. *Journal of Fluid Mechanics*, 85:57–83, 1978.

[2] B. S. Baldwin and T. J. Barth. A One-equation Turbulence Transport Model for High Reynolds Number Wall-bounded Flows. *NASA Technical Memorandum*, 1990.

[3] J. G. Bartzis and N. E. Todreas. Turbulence Modelling of Axial Flow in a Bare Rod Bundle. *J. Heat Transfer*, 10:628, 1979.

[4] M. Biemüller, L. Meyer, and K. Rehme. Large Eddy Simulation and Measurement of the Structure of Turbulence in Two Rectangular Channels Connected by a Gap. *Engineering Turbulence Modelling and Experiments*, 3:249–258, 1996.

[5] E. Brundrett and W. D. Baines. The Production and Diffusion of Vorticity in Duct Flow. *Journal of Fluid Mechanics*, 19:375–394, 1964.

[6] N. I. Buleev. Theoretical Model of the Mechanism of Turbulent Exchange in Fluid Flows. *Report AERE, Transaction*, 957, 1963.

[7] T. L. Campioli, J. Schetz, and R. Neel. Assessment of Incompressible Formulations for Numerical Solutions of Unsteady Turbulent Flows Over Bluff Bodies. In 43^{rd} *AIAA Aerospace Sciences Meeting and Exhibit*, 2005.

[8] P. Carajilescov and N. E. Todreas. Experimental and Analytical Study of Axial Turbulent Flows in an Interior Subchannel of a Bare Rod Bundle. *J. Heat Transfer*, 98(2), 1976.

[9] F. S. Castellana, W. T. Adams, and J. E. Casterline. Single–phase Subchannel Mixing in a Simulated Nuclear Fuel Assembly. *Nucl. Eng. Des*, 26(2), 1974.

[10] D. Chang and S. Tavoularis. Unsteady Numerical Simulations of Turbulence and Coherent Structures in Axial Flow Near a Narrow Gap. *Journal of Fluids Engineering*, 127:458, 2005.

[11] D. Chang and S. Tavoularis. Numerical Simulation of Turbulent Flow in a 37-Rod Bundle. *Nuclear Engineering and Design*, 237(6):575–590, 2007.

[12] S. K. Cheng and N. E. Todreas. Constitutive Correlations for Wire–wrapped Subchannel Analysis Under Forced and Mixed Convection Conditions. part 1. Technical report, DOE/ET/37240-108-TR-Pt. 1, Massachusetts Inst. of Tech., Cambridge (USA), 1984.

[13] S. K. Cheng and N. E. Todreas. Hydrodynamic Models and Correlations for Bare and Wire–wrapped Hexagonal Rod Bundles–Bundle Friction Factors, Subchannel Friction Factors and Mixing Parameters. *Nuclear Engineering and Design*, 92:227–251, 1986.

[14] X. Cheng and N. I. Tak. CFD Analysis of Thermal-hydraulic Behavior of Heavy Liquid Metals in Sub-channels. *Nuclear Engineering and Design*, 236(18):1874–1885, 2006.

[15] A. O. Demuren. Calculation of Turbulence–driven Secondary Motion in Ducts with Arbitrary Cross–section. 1990.

[16] A.O. Demuren and W. Rodi. Calculation of Turbulence-Driven Secondary Motion in Non-circular Ducts. *Journal of Fluid Mechanics*, 140:189–222, 1984.

[17] O. S. Eiff and M. F. Lightstone. On the Modelling of Single–phase Turbulent Energy Transport in Subchannels. *Proceedings of the Annual Conference – Canadian Nuclear Society*, pages 14–14, 1997.

[18] A. V. Garbaruk, M. K. Strelets, and M. L. Shur. Analysis of Three-Dimensional Turbulent Flow in an S–Shaped Rectangular Channel. *High Temperature*, 41(1):49–56, 2003.

[19] F. B. Gessner and A. F. Emery. A Reynolds Stress Model for Turbulent Corner Flows-Part I: Development of the Model. *Transactions of the ASME, Journal of Fluids Engineering*, 103:445–455, 1981.

[20] P. Godin and D. W. Zingg. High–lift Aerodynamic Computations with One and Two–equation Turbulence Models. *AIAA Journal*, 35(2):237–243, 1997.

[21] M. S. Guellouz and S. Tavoularis. The Structure of Turbulent Flow in a Rectangular Channel Containing a Cylindrical Rod–Part 1: Reynolds–Averaged Measurements. *Experimental Thermal and Fluid Science*, 23(1):59–73, 2000.

[22] M. S. Guellouz and S. Tavoularis. The Structure of Turbulent Flow in a Rectangular Channel Containing a Cylindrical Rod-Part 2: Phase-averaged Measurements. *Experimental Thermal and Fluid Science*, 23(1-2):75–91, 2000.

[23] K. Hanjalic and B. E. Launder. A Reynolds Stress Model of Turbulence and its Application to Thin Shear Flows. *Journal of Fluid Mechanics*, 52:609–638, 1972.

[24] J. Hinze. Turbulence. *McGraw-HIII: New York*, 1959.

[25] J. D. Hooper. Developed Single Phase Turbulent Flow through a Square–pitch Rod Cluster. *Nuclear Engineering and Design*, 60:365–379, 1980.

[26] J. D. Hooper and K. Rehme. Large-scale Structural Effects in Developed Turbulent Flow Through Closely Spaced Rod Arrays. *Journal of Fluid Mechanics*, 145:305–337, 1984.

[27] A. Hussain. Coherent Structures - Reality and Myth. *Physics of Fluids*, 26:2816, 1983.

[28] T. Ikeno and T. Kajishima. Analysis of Dynamical Flow Structure in a Square Arrayed Rod Bundle. In *The* 12^{th} *International Topical Meeting on Nuclear Reactor Thermal Hydraulics* $(NURETH-12)$, 2007.

[29] L. Ingesson and S. Hedberg. Heat Transfer Between Subchannels in a Rod Bundle. *pp FC7. 11.1-11 of Heat Transfer 1970. Vol. III./Grigull, Ulrich (ed.). Amsterdam*, 1970.

[30] T. Krauss and L. Meyer. Characteristics of Turbulent Velocity and Temperature in a Wall Channel of a Heated Rod Bundle. *Experimental Thermal and Fluid Science*, 12(1):75–86, 1996.

[31] B. E. Launder and W. M. Ying. Prediction of Flow and Heat Transfer in Ducts of Square Cross–section. *Proc. Inst. Mech. Engrs*, 187:455–461, 1973.

[32] G. L. Mellor and H. J. Herring. Two Methods of Calculating Turbulent Boundary Layer Behavior Based on Numerical Solutions of the Equations of Motion. I: Mean Velocity Field Method; II: Mean Turbulent Field Method. *Proceedings–Computation of Turbulent Boundary Layers*, 1, 1968.

[33] L. Meyer. Measurements of Turbulent Velocity and Temperature in Axial Flow Through a Heated Rod Bundle. *Nuclear Engineering and Design*, 146(1-3):71–82, 1994.

[34] L. Meyer and K. Rehme. Large–scale Turbulence Phenomena in Compound Rectangular Channels. *Experimental thermal and fluid science*, 8(4):286–304, 1994.

[35] S. V. Moller. Single–phase Turbulent Mixing in Rod Bundles. *Experimental Thermal and Fluid Science*, 5(1):26–33, 1992.

[36] S.V. Moller. On Phenomena of Turbulent Flow Through Rod Bundles. *Experimental Thermal and Fluid Science*, 4(1):25–35, 1991.

[37] D. Naot and W. Rodi. Numerical Simulation of Secondary Currents in a Channel Flow. *Journal of Hydraulics Division*, 108:948–968, 1982.

[38] J. Nikuradse. Gesetzmaigkeit der Turbulenten Stromung in Glatten Rohren. Forsch. Arb. Ing. *Wes. H*, 356, 1932.

[39] F. F. Ning and L. P. Xu. Application of One-Equation Spalart–Allmaras Turbulence Model in the Numerical Simulation of Internal Flows. *Journal of Engineering Thermophysics*, 22(3):304–306, 2001.

[40] P. Nithiarasu. An Efficient Artificial Compressibility (AC) Scheme Based on the Characteristic Based Split (CBS) Method for Incompressible flows. *International Journal for Numerical Methods in Engineering*, 56(13):1815–1845, 2003.

[41] S. B. Pope. *Turbulent Flows.* Cambridge University Press, 2000.

[42] K. Rehme. Simple Method of Predicting Friction Factors of Turbulent Flow in Non–circular Channels. *Int. J. Heat Mass Transfer*, 16(5), 1973.

[43] K. Rehme. The Structure of Turbulent Flow Through a Wall Subchannel of a Rod Bundle. *Nucl. Eng. Des*, 45:311–323, 1978.

[44] K. Rehme. Turbulent Momentum Transport in Rod Bundles. *Nuclear Engineering and Design*, 62(1-3):137–146, 1980.

[45] K. Rehme. The Structure of Turbulent Flow Through Rod Bundles. *Nuclear Engineering and Design*, 99:141–154, 1987.

[46] K. Rehme. Experimental Observations of Turbulent Flow through Subchannels of Rod Bundles. *Experimental Thermal and Fluid Science*, 2:341–349, 1989.

[47] K. Rehme. The Structure of Turbulence in Rod Bundles and the Implications on Natural Mixing Between the Subchannels. *International Journal of Heat and mass Transfer*, 35(2):567–581, 1992.

[48] H. Reichardt. Vollstandige Darstellung der Turbulenten Geschwindigkeitsverteilung in Glatten Leitungen. *Z. Angew. Math. Mech*, 31(7):208–219, 1951.

[49] M. Renksizbulut and G.I. Hadaller. An Experimental Study of Turbulent Flow Through a Square–array Rod Bundle. *Nuclear Engineering and Design*, 91(1):41–55, 1986.

[50] R.C.K Rock and M.F. Lightstone. A Numerical Investigation of Turbulent Interchange Mixing of Axial Coolant Flow in Rod Bundle Geometries. *Numerical Heat Transfer. Part A, Applications*, 40(3):221–237, 2001.

[51] J. T. Rogers and R. G. Rosehart. Mixing by Turbulent Interchange in Fuel Bundles. *Correlations and Inferences, ASME Paper*, 1972.

[52] J. T. Rogers and A. E. Tahir. Turbulent Interchange Mixing in Rod Bundles and the Role of Secondary Flows. *ASME Paper*, 1975.

[53] J. T. Rogers and N. E. Todreas. Coolant interchannel mixing in reactor fuel rod bundles: Single-phase coolants. *pp 1-56 of Heat Transfer in Rod Bundles. New York, American Society of Mechanical Engineers, 1968.*

[54] D. S. Rowe and C. W. Angle. Crossflow Mixing Between Parallel Flow Channels During Boiling. Part II. Measurement of Flow and Enthalpy in two Parallel Channels. Technical report, BNWL–371 (Pt. 2), Battelle-Northwest, Richland, Wash. Pacific Northwest Lab., 1967.

[55] D. S. Rowe, B. M. Johnson, and J. G. Knudsen. Implications Concerning Rod Bundle Crossflow Mixing Based on Measurements of Turbulent Flow Structure. *Int. J. Heat Mass Transfer*, 17(3), 1974.

[56] G. Roy, D. Vo-Ngoc, and V. Bravine. A Numerical Analysis of Turbulent Compressible Radial Channel Flow With Particular Reference to Pneumatic Controllers. *Journal of Thermal Science*, 13(1):24–29, 2004.

[57] R. H. Sabersky, A. J. Acosta, and E. G. Hauptmann. *Fluid Flow: A First Course in Fluid Mechanics.* New York: Macmillan, 1989.

[58] W. Seale. Turbulent Diffusion of Heat Between Connected Flow Passage. Part 2: Prediction Using k-1 Turbulence Model. *Nuclear Engineering and Design*, 54:197–209, 1979.

[59] W. Seale. Turbulent Diffusion of Heat Between Connected Flow Passages. Part 1: Outline of Problem and Experimental Investigation. *Nuclear Engineering and Design*, 54:183–195, 1979.

[60] W. J. Seale. The Effect of Subchannel Shape on Heat Transfer in Rod Bundles With Axial Flow. *Int. J. Heat Mass Transfer*, 24:768–770, 1981.

[61] W. J. Seale. Measurements and Predictions of Fully Developed Turbulent Flow in a Simulated Rod Bundle. *Journal of Fluid Mechanics*, 123:399–423, 1982.

[62] P. R. Spalart and S. R. Allmaras. A One-equation Turbulence Model for Aerodynamic Flows. In 30^{th} *Aerospace Sciences Meeting and Exhibit*, page 69, 1992.

[63] C. G. Speziale. Analytical Methods for the Development of Reynolds–Stress Closures in Turbulence. *Annual Reviews in Fluid Mechanics*, 23(1):107–157, 1991.

[64] C. Tong and Z. Warhaft. Passive Scalar Dispersion and Mixing in a Turbulent Jet. *Journal of Fluid Mechanics Digital Archive*, 292:1–38, 2006.

[65] S. Tóth and A. Aszódi. CFD Analysis of Flow Field in a Triangular Rod Bundle. In *The* 12^{th} *International Topical Meeting on Nuclear Reactor Thermal Hydraulics* $(NURETH-12)$, 2007.

[66] A. C. Trupp and R. S. Azad. The Structure of Turbulent Flow in Triangular Array Rod Bundles. *Nucl. Eng. Des*, 32(1), 1975.

[67] V. Vonka. Measurement of Secondary Flow Vortices in a Rod Bundle. *Nucl. Eng. and Des*, 106:191–207, 1988.

[68] X. Wu. On the Transport Mechanims in Simulated Heterogeneous Rod Bundle Subchannels. *Nuclear Engineering and Design*, 158(1):125–134, 1995.

[69] X. Wu and A. C. Trupp. Experimental Study on the Unusual Turbulence Intensity Distributions in Rod-to-wall Gap Regions. *Experimental Thermal and Fluid Science*, 6(4):360–370, 1993.